

VILNIUS UNIVERSITY
CENTER FOR PHYSICAL SCIENCES AND TECHNOLOGY

ALEKSEJ ŽARKOV

NOVEL SYNTHETIC APPROACHES FOR YSZ AND GDC
CERAMICS AND ANALYTICAL CHARACTERIZATION

Doctoral dissertation

Physical Sciences, Chemistry (03 P)

Vilnius, 2016

The dissertation was carried out from 2012 to 2016 at Vilnius University.

Scientific supervisor: Prof. Dr. Stasys Tautkus (Vilnius University, Physical Sciences, Chemistry - 03 P).

Scientific consultant: Prof. Habil. Dr. Aivaras Kareiva (Vilnius University, Physical Sciences, Chemistry - 03 P).

Contents

LIST OF ABBREVIATIONS.....	5
INTRODUCTION	6
1. LITERATURE SURVEY.....	8
1.1. Solid electrolytes.....	8
1.1.1. Yttria-stabilized zirconia.....	12
1.1.2. Gadolinium doped ceria.....	15
1.2. Synthesis methods.....	17
1.2.1. Preparation of bulk ceramics	18
1.2.2. Formation of thin/thick films.....	21
1.3. Elemental analysis of YSZ and GDC ceramics	24
1.3.1. Analysis of bulk ceramics.....	25
1.3.2. Analysis of thin/thick films.....	27
1.4. Application of YSZ and GDC ceramics.....	28
1.4.1. Solid oxide fuel cells.....	28
1.4.2. Gas sensors.....	31
1.4.3. Other.....	33
2. EXPERIMENTAL.....	34
2.1. Reagents and solutions.....	34
2.2. Synthesis of YSZ powders and films.....	35
2.3. Synthesis of GDC powders and films	37
2.4. Elemental analysis of YSZ powders and films	39
2.5. Elemental analysis of GDC powders and films	40
2.6. Instrumentation and characterization techniques.....	41
3. RESULTS AND DISCUSSION.....	44
3.1. Synthesis and characterization of yttria-stabilized zirconia.....	44
3.1.1. Three different synthesis techniques to the bulk ceramics	44
3.1.2. Deposition of thin films	53
3.1.3. Development of analytical techniques	55
3.2. Synthesis and characterization of gadolinium doped ceria.....	59
3.2.1. Two different synthesis techniques to the bulk ceramics	59
3.2.2. Deposition of thin films	79

3.2.3. Development of analytical techniques	90
4. CONCLUSIONS	96
LIST OF PUBLICATIONS	98
ACKNOWLEDGEMENTS	101
REFERENCES	102

LIST OF ABBREVIATIONS

AFM	– Atomic Force Microscopy
BET	– BET surface area measurement (BET from Brunauer, Emmett, Teller)
CA	– Citric Acid
CP	– Co-precipitation
CVD	– Chemical Vapor Deposition
DSC	– Differential Scanning Calorimetry
DTG	– Differential Thermogravimetry
EDTA	– Ethylenediaminetetraacetic Acid Disodium Salt
EDX	– Energy-Dispersive X-ray Spectroscopy
EG	– Ethylene Glycol
FTIR	– Fourier Transform Infrared Spectroscopy
GDC	– Gadolinium Doped Ceria
GL	– Glycerol
ICP-OES	– Inductively Coupled Plasma Optical Emission Spectrometry
PLD	– Pulsed Laser Deposition
PVD	– Physical Vapour Deposition
RMS	– Root Mean Square
RSD	– Relative Standard Deviation
SD	– Spray Deposition
SDZ	– Scandium Doped Zirconia
SEM	– Scanning Electron Microscopy
SGC	– Sol-gel Combustion
SG	– Sol-gel
SOFC	– Solid Oxide Fuel Cell
TA	– Tartaric Acid
TG	– Thermogravimetry
WDS	– Wavelength Dispersive X-ray Spectroscopy
XPS	– X-ray Photoelectron Spectroscopy
XRD	– X-ray Diffraction
YSZ	– Yttria-stabilized Zirconia

INTRODUCTION

Solid state ionics provide a fascinating interdisciplinary field of study since their discovery by Michael Faraday almost 200 years ago. Yttria-stabilized zirconia (YSZ) and gadolinium doped ceria (GDC) are the most technologically important compounds from this class of materials due to an excellent ionic conductivity [1]. Therefore, these materials could be successfully used as oxygen-ion conducting membranes (solid electrolytes) in electrochemical devices [2]. During the last decades the research has been driven by the requirements for efficient energy sources, sensors and batteries with high energy density. Exceptional importance among electrochemical devices is assigned to solid oxide fuel cells (SOFCs). This technology moves towards the generation of energy in more efficient and environmentally friendly way. Nowadays, global energy consumption constantly grows and according to U.S. Energy Information Administration it will grow by 56% between 2010 and 2040 [3]. Besides SOFCs application, ionic conductivity of YSZ and GDC is used in gas sensors and oxygen pumps [4, 5]. Moreover, YSZ due to its perfect thermal and mechanical properties is widely used as thermal barrier coatings for gas turbines [6] or dental implants [7]. In addition to electrochemical devices ceria is used in the processes of catalysis [8], chemical-mechanical polishing [9], UV-Vis absorption [10] and in optoelectronics and photovoltaics [11].

Application of thin films can be utilized in many different areas. In the case of YSZ and GDC it is of particular interest in terms of miniaturizing of electrochemical devices. Moreover, reducing thickness of electrolyte in SOFCs leads to the minimization of ohmic losses. Micro-SOFCs systems based on thin films show the highest specific energy and energy density and have a potential use for portable devices with a perspective to replace lithium-ion batteries [12].

It is well known that physical properties of crystalline materials are strongly dependent on the phase purity, grain size and grain size distribution. Therefore, it is very important to develop simple, reliable and cost-effective synthesis method for the preparation of products with controllable phase purity

and surface morphology. It is important to develop reliable analytical methods for the control of chemical composition of materials since the physical properties highly depend on the chemical composition.

The main aim of this study was to develop synthesis methods for the preparation of YSZ and GDC bulk ceramics and thin films investigating the effect of synthetic approach on the characteristics of the end products. The additional aim was to develop an analytical methods for the determination of stoichiometry of ceramics and films. The following tasks were set in order to achieve these objectives:

- Synthesis and comparative study of YSZ bulk ceramics by sol-gel, sol-gel combustion and co-precipitation and GDC bulk ceramics by sol-gel and sol-gel combustion methods.
- Application of sol-gel synthetic approaches for the fabrication of YSZ and GDC thin films using spin-coating technique.
- Development of analytical techniques for the determination of chemical composition of YSZ and GDC bulk ceramics and films.

1. LITERATURE SURVEY

1.1. Solid electrolytes

Concept of solid electrolytes (also superionic conductors, fast ion conductors) covers a wide range of materials, which are combined by one exclusive property – the defining role of ions in charge transfer. Possibility of ionic conductivity depends on the structural characteristics of the material. Most of the solid electrolytes are solid solutions based on ionic crystals. The nodes of the crystal lattice of ionic crystals are ions, forming two sublattices – cationic and anionic. Exceptionally high values of ionic conductivity are reached due to the fast diffusion of usually only one ionic species through a sublattice formed by immobile counterions. Conductivities of solid electrolytes can reach values of the order of $1 \text{ S}\cdot\text{cm}^{-1}$, which are comparable to those observed in the molten state [13].

History of solid electrolytes takes its beginning in the first half of the 19th century and associated with investigations of English scientist Michael Faraday. He introduced the basic terminology of electrochemistry, e.g. terms ion, cation, anion, electrode, anode, cathode, electrolyte and electrolysis [2]. In 1834 Faraday has classified substances into first and second types of conductors – metallic and electrolytic. The first type now recognized as electronic and the second type as ionic conductors [14]. Faraday discovered the motion of mobile ions not only in liquid, but also in solid electrolytes. He noticed that electric conductivity of silver sulfide (Ag_2S) at elevated temperatures was comparable to those observed in metals, however, contrary to metals, conductivity was lost upon cooling. The same behavior was also observed for lead fluoride (PbF_2). This appears to be the first observations of the transition from the poorly conducting to the conducting states in solid ionically conducting materials, and Ag_2S and PbF_2 in their turn are the first ever discovered solid electrolytes [15]. Towards the end of the 19th century the term “solid electrolyte” was in use, however, understanding of the nature of ionic conductivity was very poor. Significant progress was achieved after the development of X-ray techniques for

structural analysis of crystalline materials, measurements of transport number by C. Tubandt [16] and establishment of the theory of crystal lattice disorder by Y. Frenkel, W. H. Schottky, C. Wagner and W. Jost [2].

There are two main types of intrinsic lattice defects which preserve the stoichiometry of a compound – Schottky defects and Frenkel defects. Schottky defects can be represented as balanced populations of vacancies on both the cation and anion sites in a crystal lattice. In other words, if the compound has a formula MX , then the number of vacancies in cationic sublattice must be equal to the number of vacancies in anionic sublattice in order to maintain electrical neutrality, although these vacancies do not have to be geometrically close together. In a binary ionic crystal of type MX_2 , the number of anion vacancies should be twice the cation vacancies.

A population of vacancies created by displacing some atoms into normally unoccupied interstitial sites constitute a second arrangement of paired point defects, known as Frenkel defects. For this type of defects the charge balance disruption does not take place due to the simple redistribution of ions of one species in crystal lattice. A Frenkel defect in a compound with formula MX consists of one interstitial cation plus one cation vacancy, or one interstitial anion plus one anion vacancy. Equally, a Frenkel defect in a crystal of formula MX_2 can consist of one interstitial cation plus one cation vacancy, or one interstitial anion plus one anion vacancy [17, 18]. Schematic illustration of Schottky and Frenkel defects is depicted in Fig. 1.

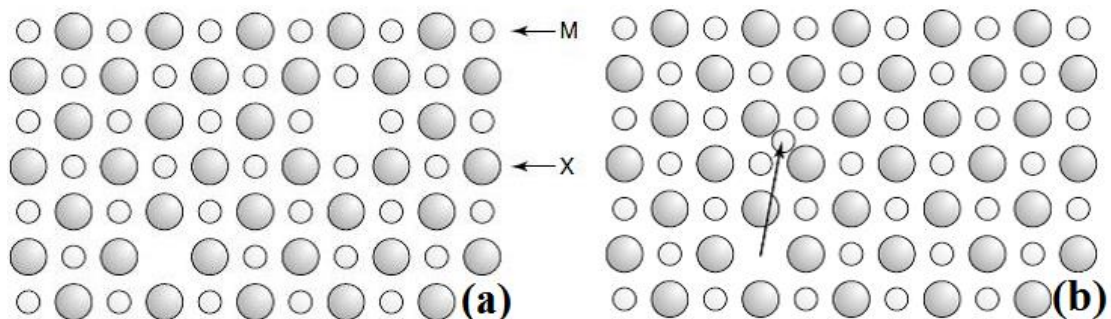


Fig. 1. Representation of point defects in an ionic crystal of formula MX :

Schottky defects (a) and Frenkel defects on cation sites (b) [17].

To move through a crystal an ion must hop from an occupied site to a vacant site. Thus ionic conductivity can only occur if defects are present. Solid electrolytes are intermediate in nature between crystalline solids which possess a regular structure with immobile ions and liquid electrolytes with fully mobile ions and without regular structure. Unlike metals, where conductivity is observed due to the motion of free electrons, and liquid electrolytes, where conductivity is determined by both anions and cations, in the most solid electrolytes conductivity is provided by the migration of ions of one type. Impurities presented in a crystal lattice give rise to extrinsic point defects. Depending on the difference of valence of host and guest ions, these impurities can lead to the formation of non-stoichiometric crystals. In some cases the certain amount of impurities are deliberately introduced in order to prepare compounds with known concentration of defects. This is a common strategy used for the synthesis of materials with properties based on the defects.

The magnitude of the ionic conduction in solids is usually much lower in comparison with electronic conductivity (especially in metals), nevertheless the same equation is used to describe the ionic conductivity:

$$\sigma = n \cdot q \cdot \mu, \quad (\text{Eq. 1})$$

where n is the charge carrier concentration, q is the electric charge and μ is the charge mobility. It is known from Nernst-Einstein relation that charge mobility depends on diffusion coefficient as follows:

$$\mu = \frac{q \cdot D}{k \cdot T}, \quad (\text{Eq. 2})$$

where k is Boltzmann constant and T is absolute temperature. Diffusion coefficient D in its turn depends on temperature in the following way:

$$D = D_0 \cdot \exp\left(-\frac{\Delta E_D}{k \cdot T}\right), \quad (\text{Eq. 3})$$

where D_0 is temperature-independent pre-exponential and ΔE_D is the diffusion activation energy. Combining of equations 1–3 provides the following expression, also called Arrhenius equation:

$$\sigma \cdot T = \sigma_0 \cdot \exp\left(\frac{-\Delta E_a}{k \cdot T}\right) \quad (\text{Eq. 4})$$

Here σ_0 is pre-exponential term and ΔE_a is activation energy for conduction. A linear relationship between $\log \sigma T$ and $1/T$ can be predicted by this equation. Mobility of ions is usually low at room temperature, however, increases exponentially with increasing the temperature.

Considering crystalline oxygen ion conductors some general aspects have to be highlighted. In such electrolytes charge transfer occurs by the movement of oxygen ions (O^{2-}) through the crystal lattice. This movement is a result of thermally-activated hopping of oxygen ions, moving in the direction of electric field. The ionic conductivity is consequently strongly temperature dependent and can approach values close to $1 \text{ S}\cdot\text{cm}^{-1}$. The crystal must contain unoccupied sites equivalent to those occupied by the lattice oxygen ions. The energy involved in the process of migration from one site to another must be small, certainly less than about 1 eV [19]. Usually, oxygen ion conductivity is observed in crystalline compounds with fluorite, perovskite or perovskite-related types crystal structures. At some conditions oxygen vacancies can provide protonic conductivity of material. This is a common phenomenon for perovskite-type solid solutions (e.g. BaCeO_3 , BaZrO_3), exposed to the humid atmosphere at elevated temperatures. Water dissolves in ceramics and oxygen vacancies are filled by hydroxide ions. Further diffusion of protons takes place according to Grotthuss mechanism [20]. In fluorite-type solid electrolytes protonic conductivity can be observed as well.

Solid electrolytes can exhibit both cationic and anionic conductivities. Mainly small ions such as H^+ , Li^+ , Na^+ , F^- and O^{2-} perform charge transfer. The ionic conductivity can be observed not only in crystalline solids but also in amorphous solids, glasses, gels and polymers. All these classes of materials can be utilized for different electrochemical applications, however, ceramic solid electrolytes are the most suitable for high-temperature devices such as fuel cells and gas sensors.

1.1.1. Ytria-stabilized zirconia

Zirconium oxide (ZrO_2) exists in three different crystalline structures, but the only stable phase at room temperature is monoclinic. The monoclinic structure transforms to tetragonal at 1170 °C, and the tetragonal transforms to cubic fluorite-type structure with $Fm\bar{3}m$ space group at 2370 °C. The cubic phase is stable up to the melting point (2680 °C). All these phase transitions are reversible on cooling. Moreover, transformation from tetragonal form to monoclinic is accompanied by 3–5% volume change [21]. High-temperature zirconia phases can be stabilized at room temperature by doping with aliovalent ions. The most commonly used stabilizing oxides are CaO, MgO, Sc_2O_3 , Y_2O_3 , and La_2O_3 . Analogically, as in the case of temperature, the monoclinic zirconia transforms to the tetragonal and then to the cubic with increasing concentration of dopant. If dopant content is not sufficient to stabilize fully cubic phase then a mixture of two or three phases can be observed. Phase diagram of yttria-stabilized zirconia (YSZ) is illustrated in Fig. 2.

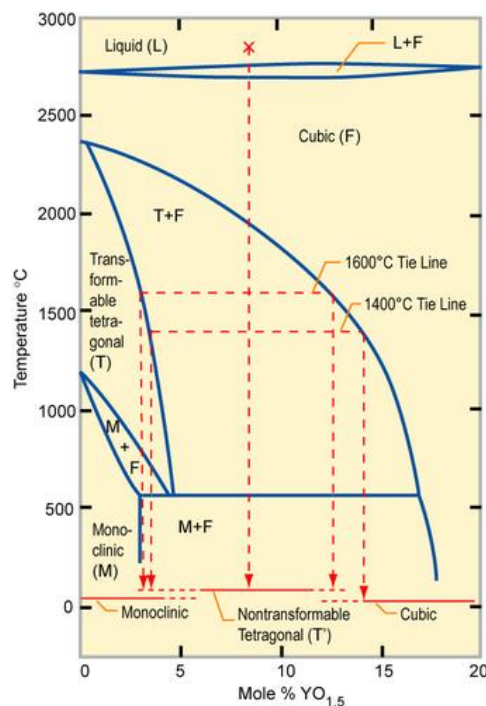
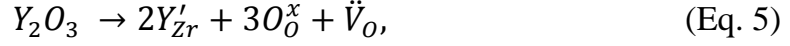


Fig. 2. Phase diagram of yttria-stabilized zirconia [22].

It can be seen that cubic structure is fully stabilized with about 14 mol% of $YO_{1.5}$. Furthermore, the addition of lower valence cations induces the generation of oxygen vacancies to maintain overall charge neutrality. The dissolution of yttria into zirconia can be written by the following quasi-chemical reaction:



where Y'_{Zr} means Y in the Zr site with a negative charge, and \dot{V}_O is the vacancy in the oxygen sublattice with double positive charge. O^x_O is the lattice oxygen, i.e., oxygen in the oxygen site with net charge of zero. The Kröger-Vink notations are used in Eq. 5.

The existence of oxygen vacancies gives rise to the ionic conductivity of zirconia. Oxygen ions are transported by hopping through the vacancies sites. The concentration of oxygen vacancies is determined by the concentration of dopant. The ionic conductivity in cubic zirconia is strongly dependent on the nature and concentration of doping ions. The dependence of the ionic conductivity on chemical composition in the system of $(ZrO_2)_{1-x}(Ln_2O_3)_x$ is shown in Fig. 3a.

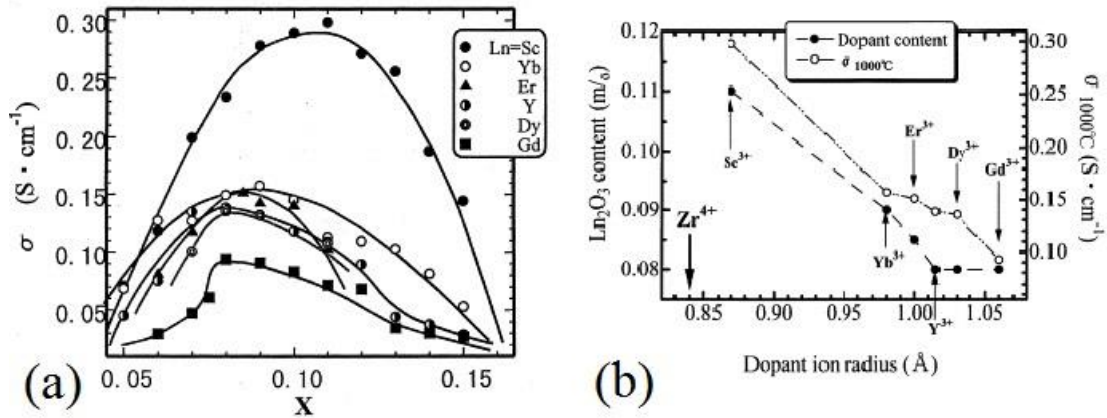


Fig. 3. Composition dependence of the electrical conductivity for $(ZrO_2)_{1-x}(Ln_2O_3)_x$ systems at 1000 °C (a) and dopant content showing the highest conductivity at 1000 °C versus dopant ion radius curves (b) [23].

Scandium doped zirconia (SDZ) exhibits the highest conductivity and the highest dopant content at maximum conductivity in comparison with other

dopants. This is related to the difference of ionic radii of host and guest ions (see Fig. 3b). The Sc(III) ionic radius is the closest to that of Zr(IV), consequently it causes the smallest crystal lattice distortion [24]. It is argued that lattice distortion (lattice stress and deviation from cubic symmetry) determines the ionic conductivity to a very large extent, and that lattice distortion is of much greater importance than many other proposed parameters [25]. In spite of the high ionic conductivity, SDZ has some disadvantages such as high cost and aging. Under long-term exposure at high temperatures, the $\text{Sc}_2\text{O}_3\text{-ZrO}_2$ system shows significant deterioration of conductivity [21, 26].

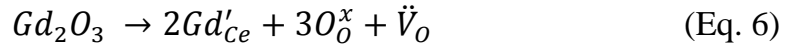
For YSZ it is clear that maximum conductivity is achieved at doping level about 8 mol% Y_2O_3 (Fig. 3a), which is slightly higher than necessary for full stabilization of cubic structure. The maximum conductivity is comparable to that of zirconia doped with Yb, Er and Dy, whereas Y is more available and cheaper. Moreover, such a strong aging effect as was determined for SDZ system was not observed for YSZ. Therefore, yttrium is the most favorable dopant for ZrO_2 . The ionic conductivity of YSZ initially increases with increasing Y content due to the increase of concentration of oxygen vacancies. It could be suggested that the higher the doping level, the higher the concentration of oxygen vacancies being created and therefore the higher the ionic conductivity. However, the maximum conductivity is achieved at a much lower concentration than it can be expected. The conductivity does not increase monotonically. It starts to decrease after reaching the maximum at ~8 mol% of Y_2O_3 . The decrease in ionic conductivity at higher levels of dopant is attributed to the interactions of the substitutional cation with the introduced charge-compensating oxygen vacancy [27]. The ionic conductivity in YSZ is temperature dependent and can be described by Eq. 4, in the same time the electronic conductivity in YSZ is negligible. In addition to the oxygen ion conductivity, a proton conductivity in porous YSZ is also possible [28]. This conductivity is attributed to proton conduction along physisorbed water (Grotthuss mechanism) at the inner surfaces. Although many other oxides exhibit higher oxygen conductivity than YSZ, this material has a number of significant advantages, including abundance,

chemical stability, mechanical strength, non-toxicity and low cost, which make it attractive for the use in electrochemical devices.

1.1.2. Gadolinium doped ceria

Cerium(IV) oxide has a cubic fluorite-type crystal structure with $Fm\bar{3}m$ space group over the temperature range from room temperature to the melting point. The fluorite structure consists of a face-centered cubic unit cell of cations with anions occupying the tetrahedral interstitial sites. In this structure each cerium cation is coordinated by eight oxygen anions, while each oxygen anion is coordinated by four cerium cations [29].

Considering the ionic conductivity in doped ceria, similar regularities and trends as in doped zirconia are observed. Mobile oxygen vacancies are introduced by substituting Ce(IV) ions by lower valence elements. In the case of gadolinium doped ceria the dissolution of Gd_2O_3 into CeO_2 can be written by the following quasi-chemical reaction:



The ionic conductivity of doped ceria depends on the temperature, nature of dopant and its concentration. Fig. 4a shows the dependence of ionic conductivity on some rare earth dopants in terms of the ionic radius. Despite the fact that ionic radii of Yb(III), Y(III) and Dy(III) (98.5, 102 and 103 pm, respectively) better matches with Ce(IV) (97 pm), Gd- and Sm-doped ceria exhibit the highest ionic conductivity. It was found that the ionic conductivity increased with increasing ionic radius of dopant from Yb to Sm, but decreased at $r > 109$ pm [30]. This trend has been attributed to the binding energy between dopant and host cations [31]. However, some disagreement between the ionic conductivity values reported by different authors are reported. According to Steele the highest ionic conductivity of differently doped ceria is exhibited by GDC in contradiction with the above findings [32].

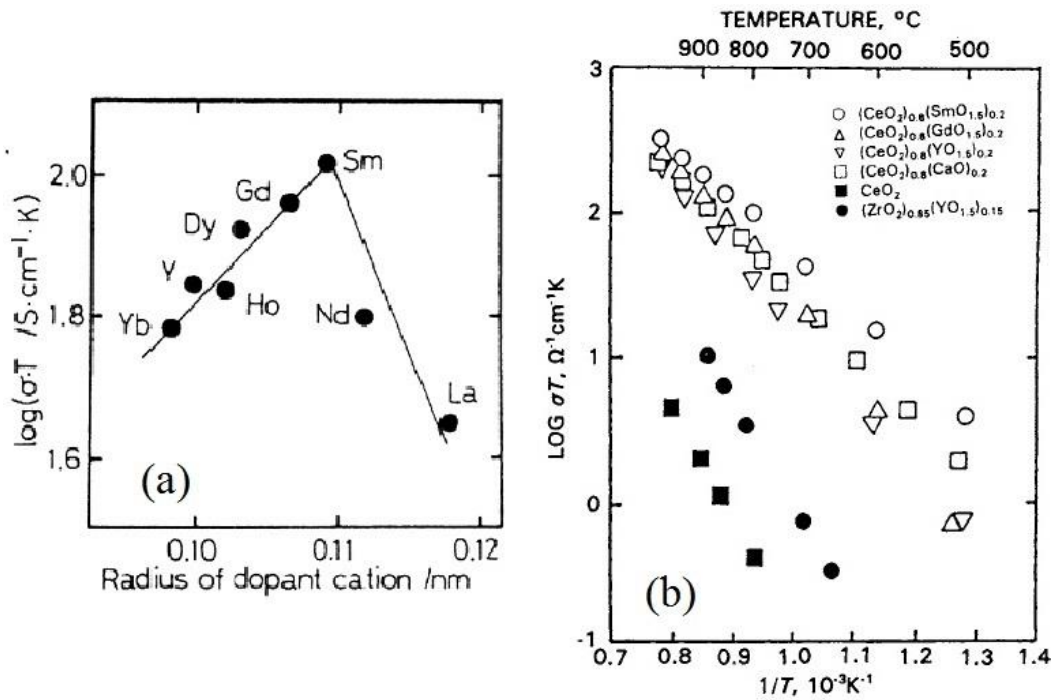
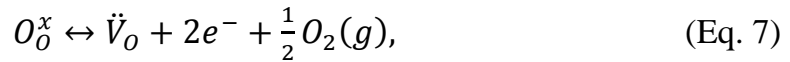


Fig. 4. Dependence of the ionic conductivity for $(\text{CeO}_2)_{0.8}(\text{LnO}_{1.5})_{0.2}$ at 800 °C on ionic radius of Ln(III) (a) [30] and Arrhenius plots of ionic conductivity of differently doped ceria (b) [31].

Actually, a clear comparison of ionic conductivity of different oxides is a quite complicated task. One of the reasons is that the activation energy varies with a type and concentration of dopant [25]. Another factor is a grain boundary resistivity which depends on method of fabrication of the samples. Nevertheless, Gd is the most common dopant for cerium oxide. The electrical conductivity of differently doped ceria as a function of temperature typically follows Arrhenius-type behavior. Fig. 4b shows several Arrhenius conductivity plots for differently doped ceria as well as for YSZ. Compared to YSZ, doped ceria shows a higher conductivity and lower activation energy, therefore, it is considered for the use as SOFC electrolyte, especially at reduced temperatures. The ionic conductivity increases as the level of substitution increases, however, it remains in force only for small concentrations of dopant. A maximum is observed at relatively low additions of dopant due to the interactions of the substitutional cation with oxygen vacancies. The most frequently used dopant concentration in ceria is in

the range of 10–20 mol% [33-35]. The ionic conductivity of GDC ceramic samples with such chemical composition is comparable.

The main disadvantage of GDC as a solid electrolyte is a chemical stability. Ceria at low oxygen pressure and at elevated temperatures (e.g. $< \sim 10^{-15}$ atm O_2 at 800 °C) releases a significant level of oxygen. Depending on the temperature and oxygen partial pressure ceria exhibits an oxygen nonstoichiometry (deficiency) with the formula of $CeO_{2-\delta}$ (δ as large as 0.3) [31]. Under such conditions Ce(IV) transforms to Ce(III) to compensate the oxygen vacancies with formation of Ce(III)/Ce(IV) redox couple. As a result an electronic conduction appears and ceria becomes mixed ionic-electronic conductor. This process can be described by the following quasi-chemical reaction:



where O_O^x , \dot{V}_O and $2e^-$ are oxide ions in the lattice, doubly charged oxygen vacancies and electrons in the conduction band made up of Ce 4f energy states, respectively [36, 37]. Further reduction of Ce(IV) results in lattice expansion limiting its utilization as an electrolyte at high temperatures and reducing atmosphere. Therefore, GDC confines to low-temperature applications (below 600 °C) where the electronic conductivity can be considerably suppressed to an acceptable level [26, 38]. The proton conductivity like in the case of YSZ was also observed in microcrystalline and nanocrystalline GDC at low temperatures and under wet conditions [39].

1.2. Synthesis methods

Many different synthesis methods used for the fabrication of YSZ, GDC and related systems are described in the literature. This chapter will give a brief review of the main synthesis techniques applied for the preparation of YSZ and GDC bulk ceramics and thin films by different researchers and research groups during the last decade.

1.2.1. Preparation of bulk ceramics

Solid-state reaction method is one of the most frequently used synthetic approach for the preparation of polycrystalline ceramic compounds because of its low manufacturing cost and simplicity. This method allows the use of wide range of starting materials such as oxides, carbonates, oxalates, etc. and does not require any solvents and sophisticated equipment. Starting components are mixed thoroughly (in some cases ball milling is applied) and calcined at high temperatures (approximately 1000–1500 °C or even higher). The synthesis of YSZ [40, 41] and GDC [42, 43] powders by solid-state reaction method were reported. However, this method has a number of disadvantages such as high calcination temperature, poor compositional homogeneity of products, uncontrollable particle size distribution and evaporation of a reactant due to high temperature [44]. In order to overcome these disadvantages a number of wet-chemical methods have been suggested. These methods attract a huge attention of scientists due to the mixing of raw materials on atomic level, which ensures an excellent chemical homogeneity of the final products and lower synthesis temperatures. Moreover, it is possible to prepare products with controlled particle size, morphology and surface area. Among the wet-chemical routes, sol-gel, sol-gel combustion, co-precipitation and solvothermal (hydrothermal) methods have found particular interest because of their simplicity, versatility, and easy scale-up capability [45].

Sol-gel process is an attractive route that starts from molecular precursors and forms an oxide network via inorganic polymerization reactions. The precursors used in the sol-gel processing are metal-organic compounds, mostly metal alkoxides *e. g.*, zirconium(IV) propoxide and cerium(IV) isopropoxide. However, alkoxides are very sensitive to moisture and must be handled under a dry or inert atmosphere to avoid precipitation. During hydrolysis and condensation of metal alkoxides a sol-gels are forming. Complexing agents such as β -diketones, carboxylic acids and other are added to decrease the hydrolysis rate and prevent the precipitation of metal hydroxides. After gelation process,

the gels are dried and calcined at high temperatures. The characteristics of obtained powders are highly influenced by experimental parameters such as the temperature, pH, chemical composition, reactant concentrations and nature of the solvent and complexing agents. This process has a number of advantages such as high phase purity, good homogeneity of the product, low synthesis temperatures, inexpensive equipment [45]. Viazzi *et al.* synthesized YSZ powders from zirconium(IV) propoxide and yttrium(III) nitrate in 1-propanol medium [46]. Number of parameters such as hydrolysis rate, concentration of precursors in the sol and the role of organic additives have been investigated. Final heat treatment of synthesized xerogels was performed at 950 °C for 2 h. Wang *et al.* reported on the aqueous sol-gel synthesis of GDC powders [47]. Ce and Gd nitrates were used as starting materials and sucrose was used as organic chelating agent. Crystalline powders were obtained above 500 °C.

Solution combustion synthesis is a time- and energy-saving method which involves the exothermic reaction of an oxidizer (most frequently metal nitrates or ammonium nitrate are used) with an organic fuel (typically glycine, urea, sucrose). Solution combustion route can be combined with sol-gel process when fuel acts as chelating agent. Once the mixture of reagents is ignited, the high self-generated energy can convert precursors into the corresponding oxide materials without an additional external energy input [48]. The resultant oxide ash obtained after combustion process is typically composed of fine particles linked together in a networked structure. The morphology, particle size and specific surface area of products are highly influenced by the fuel type and fuel/oxidizer ratio. Mohebbi *et al.* investigated the influence of pH of the precursor solution on the characteristics of Ni-YSZ composite in microwave-assisted nitrate-glycine combustion process [49]. Crystalline products after combustion process were obtained for all selected pH values with smallest crystallites at pH = 9. Mesoporous pure and rare earth doped ceria powders were prepared by nitrate-citrate auto-combustion process [50].

Co-precipitation method is based on the simultaneous precipitation from solution of different ions in the form of insoluble compound which is converted

to final crystalline particles by thermal treatment. Precipitants such as ammonia, ammonium carbonate, oxalic acid, etc. can be employed to produce YSZ and GDC powders. Difficulties in the synthesis of ternary metal oxides can occur due to the different precipitation rates of elements. It can lead to the variation of target stoichiometry of products. Padney *et al.* synthesized YSZ powders by drop wise adding ammonia to the starting metal nitrates solution. pH of the solution was raised up to 9–10 for complete precipitation. Precipitates were filtered, dried and calcined at 1000 °C [51]. The reports on similar synthesis were published elsewhere [52, 53]. GDC powders were prepared by reverse-strike precipitation (by adding salt solution to the precipitant one) using aqueous solutions of NH_4HCO_3 [54] and $(\text{NH}_4)_2\text{CO}_3$ [55] as precipitants. Filtered and dried precipitates were calcined at 700–950 °C.

The solvothermal process is defined as a chemical reaction taking place in a sealed vessel at temperatures above the solvent boiling point and at elevated pressures. The medium used in a solvothermal synthesis can vary from water (hydrothermal) to ammonia (ammonothermal), an alcohol (alcothermal) or other organic solvent [56]. This technique does not require final calcination process such as in sol-gel and co-precipitation synthesis routes. Therefore, it is possible to produce agglomerate-free powders. Sato *et al.* successfully employed hydrothermal method for the synthesis of YSZ [57] and GDC [58]. YSZ nanocrystals with controlled yttria content (3–12 mol%) and size less than 10 nm were synthesized at 150 °C for 1–24 h. Synthesis of GDC powders was carried out at 125–150 °C temperature for 6–24 h and resulted in nanocrystals with a size of approximately 4 nm.

To conclude, there is a variety of synthesis methods acceptable for the preparation of YSZ and GDC powders. Each of them, however, has some advantages and disadvantages and can be chosen depending on the required properties of the final product and accessibility. The microstructure, mechanical, chemical and electrical properties of ceramics can be designed using different chemical approaches.

1.2.2. Formation of thin/thick films

For a large number of technological devices YSZ and GDC must exist in the form of films or coatings. The choice of an appropriate film deposition technique is obviously influenced by the desired film quality, morphological features and the cost of fabrication. There are two most commonly used techniques for the preparation of thick ceramic films: tape-casting and screen-printing. Tape casting is a technique which utilizes a fluid suspension of ceramic or metallic particles in an organic solvent or water as the starting point for processing. Organic and/or inorganic additives such as plasticizers, binders, dispersants, pore formers, etc. are added to the powders to form the slurry. The actual tape is formed when the slurry is cast onto a flat moving surface with a removal of excess substance from a coated surface by the blade. Further sintering at elevated temperatures is applied in order to remove all additives and solvents. Tape casting is a low cost process particularly well-suited for the fabrication of 10–500 μm thick flat uniform ceramic sheets, it is straightforward, scalable and may be used with a variety of materials. This method allows producing a wide variety of controlled morphologies, from highly porous to fully dense microstructures [59-61]. Both dense and porous YSZ films with a thickness of about 30 μm were fabricated [62]. The results on the preparation of porous GDC films with a thickness ranging from 360 to 450 μm were also published [63]. Xiong *et al.* [64] reported on the preparation of porous approximately 500 μm thick NiO/GDC layer and fully dense GDC film with a thickness of 13 μm . The screen-printing technique is also based on utilizing ceramic particles dispersed in a solvent with a number of additives. The ink slurry is forced through the screen, which then snaps away leaving a film on the substrate [61]. As-deposited films are dried and sintered at certain temperature depending on the desired morphology of the final product. Seok *et al.* reported on the fabrication of screen-printed layered YSZ/GDC structure with a thicknesses of 2.5 μm and 9 μm for YSZ and GDC, respectively. The deposited layers were confirmed to be dense and only a small amount of isolated pores was

observed [65]. Porous 9 μm thick GDC layer was screen-printed on YSZ pellet [66] and porous NiO-YSZ composite and dense YSZ film were prepared [67] using this technique.

There is a variety of methods suitable for the formation of thin ($\leq 1 \mu\text{m}$) YSZ and GDC films. Generally these techniques can be divided into two basic groups: vacuum deposition techniques and liquid-precursor-based deposition techniques. Crystallinity and microstructure of the thin films are highly influenced by the deposition method. Vacuum methods usually lead to crystalline films forming already during the deposition process, non-vacuum methods usually result in amorphous films which can be transformed into crystalline films via annealing procedure. Columnar microstructure is usually observed for vacuum-deposited films and bricklayer-type containing of a large number of randomly oriented crystalline grains for non-vacuum [12]. Vacuum deposition techniques in their turn can be divided into physical vapor deposition (PVD) and chemical vapor deposition (CVD).

One of the most popular PVD method is sputtering. During this process material is removed from the solid cathode target as a result of collision with positively charged ions of noble gas (usually argon). Gas-phase atoms are transported from the source to the substrate, upon which the film will nucleate and grow. However, it may be difficult to maintain desired stoichiometry of a multicomponent films due to the different sputtering rates of the constituents. In [68], dense YSZ films were deposited by magnetron sputtering on porous NiO/YSZ cermet substrate from metallic targets. Tanveer *et al.* deposited 140 nm thick GDC film on YSZ substrate by radio frequency sputtering using GDC powders as a target [69]. Epitaxial 75 nm thick YSZ and GDC films on MgO and Al₂O₃ substrates were produced by simultaneously sputtering from single-element targets [70]. Another PVD technique successfully employed for the deposition of YSZ and GDC films is pulsed laser deposition (PLD). This method based on the interaction of high-power pulsed laser beam (usually of wavelength in the UV range) with a solid target. Material is ablated from the target surface and subsequently deposited onto the preheated substrate.

This method allows to achieve epitaxial film growth and relatively high deposition rates (> 10 nm/s) [71]. Epitaxial GDC films up to 1 μm in thickness were deposited on a single crystal YSZ substrate [72, 73] and thinner coatings (52–403 nm) were obtained on sapphire [74].

Basic difference between PVD and chemical vapor deposition (CVD) is the way how materials are transferred from the vapor phase to the solid phase. In the case of CVD, gas phase reactions or gaseous decomposition as the source of materials are used. During CVD process the reactive gas transports one or few premixed volatile precursors, which react and/or decompose on the surface of preheated substrate leading to the formation of film [75]. Schlupp *et al.* reported on the fabrication of GDC and YSZ films using CVD technique. The layered structure of GDC films with thickness of ~ 150 nm and granular (270 nm) or columnar (130 nm) YSZ films were obtained [76].

As was mentioned earlier, wet-chemical processes (spraying, dipping and spinning) are used extensively to produce YSZ and GDC thin films [77]. The spray deposition (SD) techniques are based on the generation of a fine aerosol of a liquid precursor solution, which is nebulized towards a heated substrate surface, where the droplets evaporate and organic compounds decompose, leading to the formation of desired thin film. Different modifications of SD which are mainly distinguished by the method of atomization such as electrostatic, flame and ultrasonic SD are known [77-79]. Porous 200–700 nm thick YSZ and GDC films were synthesized using SD technique by Scherrer *et al.* [80]. Dense, continuous and crack-free GDC films with a thickness of about 85 nm were fabricated on YSZ pellets [81].

During dip-coating process the substrate is partly or fully immersed into precursor solution following by withdrawing and annealing. This method allows to coat the objects with complex shapes, and planar substrates can be coated on the both sides at once. Thickness of the prepared films depends on the viscosity of precursor solution and substrate immersing and withdrawing rate. Mesoporous and macroporous YSZ thin films were prepared on Si substrates using sol-gel synthesis method [82]. Both dense and mesoporous 100–700 nm

in thickness GDC coatings were deposited on different substrates by Hierso *et al.* [83].

Spin-coating technique is a rapid, useful and cost-effective processing route for the synthesis of thin and uniform coatings on planar substrates. In this technique, the precursor solution is dispensed onto a substrate with further spinning of the substrate at high speed (few thousand rpm). Thin film on the surface is forming due to the spreading of the solution on the substrate by centripetal acceleration. Final film thickness and other properties depend on a number of factors such as viscosity, concentration, surface tension of precursor solution, drying rate, sintering temperature and rate, spinning speed etc. Of course, the thickness of the films can be controlled by applying a certain number of deposition cycles. A huge variety of precursors can be used for spin-coating, such as metal carboxylates, alkoxides, halogenides, nitrates, acetates and suspensions [84, 85]. Thin YSZ and GDC films with a thickness of about 1 μm were also fabricated by spin-coating technique on porous substrates [86].

Morphology, mechanical and electrical properties of YSZ and GDC films can vary depending on the used deposition technique. Development of cost-effective methods to produce these materials on a large scale with a good quality is necessary for industrial applications.

1.3. Elemental analysis of YSZ and GDC ceramics

Since physical properties of YSZ and GDC are strongly dependent on the chemical composition, it is necessary to have an analytical method for the accurate and precise determination of element content in this kind of ceramics. This is of particular importance considering synthesis methods, where due to the procedure peculiarities element ratio in final product can be different from element ratio in the precursors. For the analytical purposes, X-ray spectroscopic techniques such as energy-dispersive X-ray spectroscopy (EDX), wavelength-dispersive X-ray spectroscopy (WDS) and X-ray photoelectron spectroscopy (XPS) are most frequently used. These methods are fast, non-destructive (or

quasi non-destructive) and are suitable for both powders and films. EDX and WDS allow to perform elemental mapping, which is very useful investigating elemental distribution and migration via diffusion. XPS technique allows to determine an oxidation state of the elements, which is very important considering the existence of cerium in dual oxidation states of +3 and +4. Among the disadvantages of such techniques is high cost, quite poor accuracy and precision. Actually, these methods are surface analysis techniques. For the analysis of bulk ceramics destructive wet chemical methods such as inductively coupled plasma optical emission spectroscopy (ICP-OES) can be applied. This technique exhibit good accuracy and precision, low detection limits and comparatively fast analysis, however, cannot provide an information on the oxidation state of analytes.

1.3.1. Analysis of bulk ceramics

High performance liquid chromatography (HPLC) and X-ray Fluorescence (XRF) analyses were employed for the determination of yttrium content in differently doped YSZ bulk ceramics synthesized by co-precipitation method [87]. For HPLC analysis, the samples were dissolved in HF and H₂SO₄ mixture, whereas for XRF measurements, the samples were prepared as pellets with boric acid as binder. The results obtained by XRF were in a good agreement with a nominal yttrium content. However, the HPLC revealed slightly lower yttrium content. The authors explain it by the losses occurred during dilution process used to prepare the samples.

Hao *et al.* utilized EDX method for the analysis of ordered YSZ nanoarrays synthesized by template assisted sol-gel method [88]. Metal precursors were mixed with Zr to Y ratio 92:16. The obtained EDX results were in a good agreement with expected composition. Yttrium content in sol-gel derived (Y₂O₃)_x(ZrO₂)_{1-x} (0.02 ≤ x ≤ 0.1) microspheres was determined by means of ICP-OES and EDX [89]. Interestingly, the mean values obtained by both techniques varied up to 31%, however, the authors do not comment on this

difference. It was noticed that for the particles with higher yttrium content the EDX values were higher than expected, but ICP-OES analysis of these samples was not performed. Uncertainty for ICPS-OES was ± 0.4 mol%, whereas for EDX it was ± 1 mol%. Elemental analysis of YSZ aerogels with Zr/Y ratios corresponding to 3–25 mol% Y_2O_3 substitution was also performed by ICP-OES [90]. Yttrium content agreed well for the samples prepared with lower yttrium amount, whereas the determined yttrium content for the sample prepared with 25 mol% substitution was lower than expected.

XPS analysis was used in order to evaluate surface atomic composition in sol-gel derived GDC samples [91]. Ce to Gd ratio in $Gd_{0.1}Ce_{0.9}O_{1.95}$ powders was found to be 5.67 instead of nominal 9.0. Such a significant mismatch authors explain by inhomogeneous distribution of dopant in the sample. Qualitative EDX analysis was performed for the NiO-10GDC composites [92]. Homogeneous distribution of Ni, O, Ce and Gd in calcined powders was confirmed by elemental mapping. WDS analysis of $Ni_{1-x}Co_x-Ce_{0.8}Gd_{0.2}O_{1.9}$ cermets synthesized by combustion method was performed by Cho *et al.* [93]. It was confirmed that prepared powders have an expected compositions, where the Ce to Gd atomic ratio was in the range from 79.6:20.4 to 82.1:17.9.

Lee *et al.* [94] performed elemental analysis by ICP-OES in order to compare cation composition changes between as-mixed precursors and as-prepared GDC powders synthesized by radio frequency thermal plasma treatment. It was found that Gd content in the as-prepared powders was slightly reduced (< 3 at.%) for $Gd_{0.2}Ce_{0.8}O_{1.9}$ in comparison to that of the starting materials and the change in Gd content appears less for $Gd_{0.1}Ce_{0.9}O_{1.95}$. Wang *et al.* [47] performed elemental analysis of sol-gel derived $Gd_{0.2}Ce_{0.8}O_{1.9}$ powders heated at different temperatures by means of ICP-OES and EDX. Ce to Gd ratio determined by ICP-OES was 81:19 and 83:17. The EDX analysis revealed results of 80:20 and 81:19, which are closer to the nominal stoichiometry.

1.3.2. Analysis of thin/thick films

For the analysis of films predominantly the same techniques are used as for bulk ceramics with only exception that wet chemical methods are not usually applied. The chemical composition of YSZ thin films deposited by MOCVD technique was determined by XPS [95]. It was found that yttrium content in the films was always lower, than in the precursor mixture. For example, approximately 25 mol% Y_2O_3 in the precursor mixture was needed to deposit YSZ films of 10 mol% Y_2O_3 . Heiroth *et al.* studied chemical composition of thin YSZ films prepared by PLD technique using Rutherford backscattering spectrometry combined with particle-induced X-ray emission [96]. The obtained results were in a good agreement with theoretical values. Furthermore, about 1% of Hf was detected as impurity.

Jiang *et al.* analyzed elemental composition of GDC thin films deposited by magnetron sputtering using XPS [70]. It was shown that deposition rate of Gd_2O_3 was much lower than that of CeO_2 , which results in the lower dopant concentration. The relationship between the actual atomic ratio and the expected atomic ratio was found equal 1.5. Hong *et al.* studied compositional changes during e-beam evaporation between GDC film and evaporating GDC powders by means of EDX [97]. Analysis results showed that chemical composition of GDC film was slightly different compared with GDC powders. The thin film appeared to have higher Gd content and lower Ce content than evaporating GDC powders, indicating the different evaporation behavior of the components. Thus, Gd content in evaporating powders should be controlled to obtain a desired composition of GDC thin film.

To summarize, there is a number of analytical techniques which allow to determine the chemical composition of YSZ and GDC bulk ceramics and films. However, most of the modern techniques are quite expensive and not widely available. Therefore, there is still a need in the development of accurate and cost-effective analysis techniques.

1.4. Application of YSZ and GDC ceramics

YSZ and GDC materials could be applied in a variety of areas due to their excellent electrical, mechanical, catalytic and optical properties. This chapter will give a brief review on the main applications of YSZ and GDC.

1.4.1. Solid oxide fuel cells

Solid oxide fuel cell is a high-temperature electrochemical device that directly converts chemical energy into electricity with high efficiency and low emission. A single cell SOFC consists of 3 key components: porous anode (fuel electrode), porous cathode (oxygen electrode) and dense electrolyte between them. The heart of SOFC is an oxygen ion or proton conducting ceramic membrane. Fully solid construction of device allows to eliminate the electrolyte management problems associated with the liquid electrolyte fuel cells. Schematic diagram of the processes taking place during the operation in a SOFC is illustrated in Fig. 5.

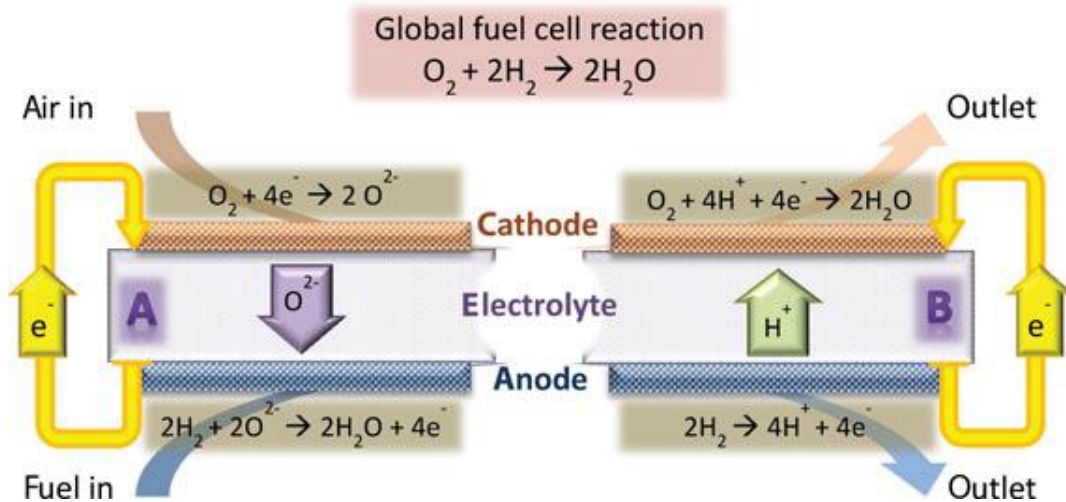


Fig. 5. Schematic view of SOFCs based on oxygen ion conductors (a) or protonic conductors (b). In both cases the fuel is hydrogen while air is the supplier of oxygen for the global fuel cell reaction [98].

Electrochemical reduction of oxygen molecules to oxide ions takes place on the cathode side at the three-phase boundary (cathode, electrolyte and gas phase) and can be described by the following equation:



The oxygen ions cross the electrolyte, where react with hydrogen at three-phase boundary on the anode side yielding water vapors and 2 electrons, which migrate to the cathode through an external circuit:



Overall reaction can be written as follows:



In SOFC with proton conducting electrolyte hydrogen ions migrate through the electrolyte from anode to cathode side.

Electrolytes used in SOFC have to meet a number of criteria: dense and gas tight; chemically stable in reducing and oxidizing environments, sufficient ionic conductivity at operating temperatures, non-electron conductor; thin to reduce ionic resistance, thermally stable. YSZ is the most commonly used electrolyte in SOFC, however, to achieve a proper ionic conductivity in YSZ ceramics, the system must operate at about 1000 °C. In order to reduce operating temperature, alternative electrolyte materials with higher ionic conductivity are considered. GDC is one of the most attractive materials to use as an electrolyte in SOFC in the temperature range from 500 to 700 °C. However, the main weakness of GDC electrolyte is a lack of stability at high temperatures and under low oxygen pressure, reduction of Ce(IV) to Ce(III) leads to the electronic conductivity.

The anode layer has to meet following main requirements: electronic conductivity, porous microstructure for gas-phase diffusion to the electrolyte interface, chemical and thermal stability at reducing environment and at high temperature, compatibility with electrolyte and interconnect materials, catalysis of anode reaction (see Eq. 9). Anodes are usually made from metal-ceramic composites (cermets) and the choice of proper anode material depends on the

electrolyte. For YSZ electrolytes Ni-YSZ anodes are preferred and Ni-GDC are usually chosen for GDC electrolyte. This strategy leads to a better anode-electrolyte interface – YSZ (GDC) in anode bonds to YSZ (GDC) in the electrolyte [24, 27, 99, 100].

Most frequently cathodes are made from electronically conducting oxides or mixed electronically and ionically conducting ceramics. Currently, perovskite structure compounds such as lanthanum strontium manganite ($\text{La}_x\text{Sr}_{1-x}\text{MnO}_{3-\delta}$, LSM) [101] or lanthanum strontium cobalt ferrite ($\text{La}_x\text{Sr}_{1-x}\text{Co}_y\text{Fe}_{1-y}\text{O}_{3-\delta}$, LSCF) [102] are the most common cathode materials. In addition to the application as an electrolyte and anode material GDC can be used in SOFC as an interlayer between YSZ electrolyte and cathode [103]. At high temperatures LSCF and YSZ chemically react, inducing the formation of 2 insulating phases ($\text{La}_2\text{Zr}_2\text{O}_7$ and SrZrO_3) and thin GDC interlayer is introduced in order to prevent this reaction [81].

Considering the geometry design, SOFCs can be divided into planar, where the electrolyte is sandwiched in between the electrodes, and tubular, where air and fuel are passed through inside and outside of the tube. Both these types are manufactured by different companies and have their own advantages and disadvantages [104].

Comparing to other types of fuel cells, the SOFCs have a number of advantages, which include high efficiency, long-term stability, fuel flexibility (hydrogen, hydrocarbons, ammonia, alcohols, carbon monoxide, etc. can be used), low emissions and relatively low cost. The main disadvantage is a high operating temperature which results in longer start-up times and mechanical and chemical compatibility issues. Primarily SOFCs used for stationary power generation and major application is at 1–5 kW level to supply combined heat and power to residential buildings utilizing natural gas as a fuel. However, large SOFC system with power up to 220 kW were successfully fabricated and tested [26]. Micro-SOFCs designed using thin film techniques can be utilized in portable electronic devices and partially replace Li batteries [12]. Typically thin and dense electrolyte membranes are fabricated on Si wafers. Electrodes (usually

porous Pt) are deposited on the electrolyte after removing Si by lithography and etching. Despite of all advantages of SOFCs the main drawback to the large-scale commercialization of such power systems remains their high cost compared to conventional power generation technologies.

1.4.2. Gas sensors

The solid electrolytes are widely used as high-temperature electrochemical gas sensors. The most common type of such devices is oxygen or so-called lambda sensors. Nowadays, such oxygen sensors are installed in quantities of millions in automotive exhaust gas systems to regulate air-to-fuel ratio (λ) [105]. According to the configuration and sensing principle, they can be divided into potentiometric, amperometric and resistive sensors. Among different ceramic materials YSZ has been also used for solid state oxygen sensors due to its ionic nature, good stability in harsh environment and cost. Principal scheme of thimble-shaped potentiometric oxygen sensor is showed in Fig. 6a.

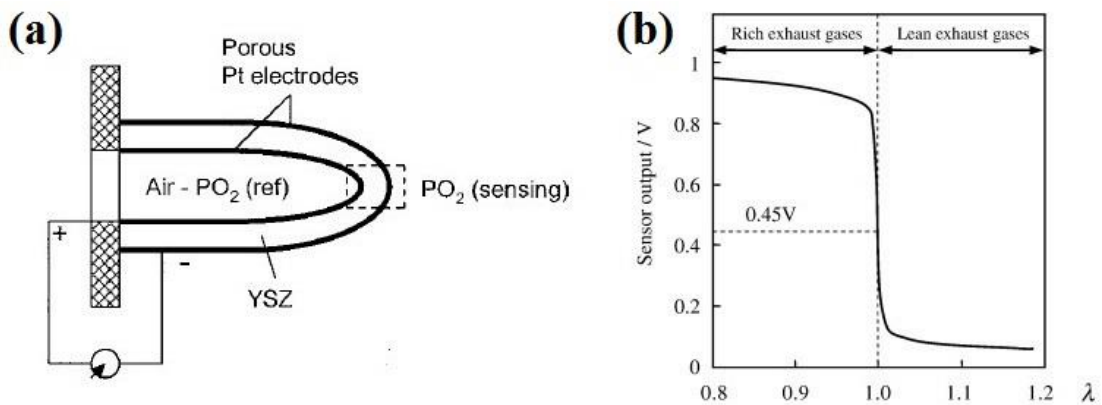


Fig. 6. Principal scheme of potentiometric oxygen sensor (a) [106] and typical response of oxygen sensor to changes in air-to-fuel ratio (b) [4].

It consists of solid electrolyte and two porous (usually Pt) electrodes. When solid electrolyte is placed between different oxygen partial pressure, the following electrode reaction occurs at the three-phase boundary:



The electromotive force (emf) between electrodes is expressed by the Nernst equation when the transport number of oxygen ions is unity in the electrolyte.

$$emf = \frac{RT}{4F} \ln \frac{p'_{O_2}}{p''_{O_2}}, \quad (\text{Eq. 12})$$

where R is the gas constant, T is an absolute temperature, and F is the Faraday constant. If oxygen partial pressure on the one side is known, the oxygen partial pressure on the other side can be calculated by Eq. 12. This is the basic principle of a potentiometric oxygen sensor. A reference air or a metal-metal oxide mixture can provide a constant oxygen activity. The sensitivity of potentiometric sensors expressed by $RT/4F$ depends only on temperature [4]. The characteristic output signal of lambda sensor is illustrated in Fig 6b. The exhaust emission products depend on the λ point at which the engine functions. In the fuel rich region CO and hydrocarbons are major emission components and in the fuel lean region NO_x emission dominates. Oxygen sensor output is fed back to the engine control system so that the engine operates between the rich and lean fuel conditions centered on the stoichiometric ratio.

In amperometric sensors oxygen is pumped from one side of the electrolyte to another by an applied external voltage. The resulting ionic current flowing through the electrolyte is a function of the oxygen concentration [107]. TiO₂, CeO₂, Ga₂O₃ and SrTiO₃ are the most frequently used materials for such sensors [108]. With appropriate electrode material and design, the solid electrolyte-based sensors are suitable not only for oxygen detection, but for other gaseous species, such as NO_x, CO, CO₂, SO₂, NH₃ and hydrocarbons as well [109-112]. Ceria-based gas sensors are not as widespread as zirconia-based, however, there is a majority of scientific articles on the development of such devices [113-115]. Oxygen sensors are able to measure oxygen concentration not only in the gaseous phase but also in liquids and molten metals.

1.4.3. Other

In addition to SOFCs and gas sensors, the YSZ and GDC ceramics could be applied in other different industrial areas. For instance, YSZ films are used as mechanical, chemical and thermal protective coatings. Low thermal conductivity provides thermal protection, hardness defends against scratching and erosion, chemical inertness protects against corrosion, high thermal expansion coefficient helps to alleviate the stresses arising from thermal expansion mismatch with covered metal [116]. YSZ and ceria-YSZ are popular materials for thermal barrier coatings on combustors, stationary and rotating components of gas turbines or diesel engines [6], [117]. YSZ ceramics also find biomedical application in manufacturing of dental implants [7] and femoral heads for total hip replacements [118]. Nanostructured YSZ films were used for optical humidity sensing [119]. YSZ monocrystals due to its optical properties and hardness are used in jewelry. YSZ- and GDC-based oxygen pumps are used for oxygen separation and high grade purification of gases. Moreover, YSZ is used in catalysis [120] and photonics [89]. As refractory material YSZ can be used to make crucibles for melting metals, liners for jet and rocket motor tubes, resistance furnaces, etc. The GDC and pure ceria can be used in humidity sensors [121], catalysis [8] and other [122].

2. EXPERIMENTAL

2.1. Reagents and solutions

The following starting materials were used for the synthesis and analysis: $Zr(CH_3COO)_x \cdot (OH)_y$ (Sigma-Aldrich, 99.9%), $Y(CH_3COO)_3 \cdot 4H_2O$ (Alfa Aesar, 99.5%), $ZrO(NO_3)_2 \cdot xH_2O$ (Sigma-Aldrich, 99%), $Y(NO_3)_3 \cdot 6H_2O$ (Alfa Aesar, 99.9%), $Zr^{x+} \cdot xCH_3COOH$ (Sigma-Aldrich, $Zr^{x+} \approx 15-16\%$), $Ce(NO_3)_3 \cdot 6H_2O$ (Alfa Aesar, 99.99%), $Gd(NO_3)_3 \cdot xH_2O$ (Alfa Aesar, 99.9%), $Ce(CH_3COO)_3 \cdot xH_2O$ (Sigma-Aldrich, 99.9%), $Gd(CH_3COO)_3 \cdot xH_2O$ (Alfa Aesar, 99.9%), $C_{15}H_{21}CeO_6 \cdot xH_2O$ (cerium(III) acetylacetonate hydrate, Sigma-Aldrich), $C_{15}H_{21}GdO_6 \cdot xH_2O$ (gadolinium(III) acetylacetonate hydrate, Alfa Aesar, 99.9%), $C_2H_2O_4 \cdot 2H_2O$ (oxalic acid dihydrate, Sigma-Aldrich, $\geq 99\%$), NH_4OH (Chempur, 25 wt.%), $C_6H_8O_7$ (citric acid, Penta, 99.5%), C_3H_8O (2-propanol, Lab-scan, 99.8%), $C_5H_8O_2$ (acetylacetone, Penta, 99.5%), $C_2H_6O_2$ (ethylene glycol, Sigma-Aldrich, $\geq 99.5\%$), $C_3H_8O_3$ (glycerol, Sigma-Aldrich, $\geq 99.5\%$), $C_4H_6O_6$ (tartaric acid, Penta, $\geq 99.5\%$), CH_3OH (methanol, Roth, $\geq 99\%$), H_2SO_4 (Roth, 98 wt.%), HNO_3 (Roth, 65 wt.%), HCl (Roth, 37 wt.%), CH_3COOH (Sigma-Aldrich, $\geq 99\%$), H_2O_2 (Reachem, 35 wt.%), $AgNO_3$ (Sigma-Aldrich, ≥ 99.0), EDTA (ethylenediaminetetraacetic acid disodium salt dihydrate, $\geq 99\%$, Sigma-Aldrich), $(NH_4)_2S_2O_8$ (Alfa Aesar, 98%), arsenazo III (2,7-Bis(2-arsenophenylazo)chromotropic acid, Reachem).

Single element ICP standard solutions of Y, Zr, Gd and Ce (1000 $\mu g/ml$, Roth) were used for spectrophotometric measurements and ICP-OES. Working solutions were prepared daily by appropriate dilution. Standard solutions of arsenazo III (0.05 and 0.2% (w/v)) were prepared by dissolving an appropriate amount of arsenazo III in deionized water. A stock solution of EDTA (0.1 mol/L) was prepared by dissolving an appropriate amount of EDTA in deionized water. A working standard solution (0.01 mol/L) was prepared by diluting with deionized water. A standard working solution of nickel (0.01 mol/L) was prepared by dissolving an appropriate amount of Ni_2O_3 in a 3:1 mixture of HCl and HNO_3 .

2.2. Synthesis of YSZ powders and films

YSZ powders with 5, 8 and 10 mol% of Y_2O_3 (5YSZ, 8YSZ and 10YSZ, respectively) have been synthesized utilizing 3 different methods (co-precipitation, sol-gel combustion and sol-gel).

Co-precipitation synthesis route (CP)

For the preparation of YSZ powders by CP method the stoichiometric amounts of $Zr(CH_3COO)_x(OH)_y$ and $Y(CH_3COO)_3 \cdot 4H_2O$ were dissolved in diluted acetic acid. The obtained solution of Y and Zr salts was slowly poured into aqueous solution of oxalic acid under active stirring at 50 °C for 30 min. As a result, white opaque colloidal solution has formed. Concentrated ammonia solution was then added drop wise to the reaction mixture up to pH = 9–10 to promote sedimentation. The precipitate was filtered, washed with distilled water and then dried for 24 h at 100 °C in air. Finally, dry powders were ground in an agate mortar and then annealed in a furnace at different temperatures for 5 h (5 °C/min) in air.

Sol-gel combustion synthesis route (SGC)

The appropriate amounts of $Y(NO_3)_3 \cdot 6H_2O$ and $ZrO(NO_3)_2 \cdot xH_2O$ were dissolved separately in distilled water and then mixed together. Complexing agent (citric acid, CA) was then added to the above solution in 1:2 (Y + Zr):CA molar ratio. The resulted solution was mixed for 1 h at 60 °C and then concentrated by evaporation of solvent at 100 °C until it turned into a viscous gel. Then temperature was raised to ~250 °C to initiate self-propagating gel combustion process, which was accompanied with evolution of gases. The resulted grey powders were ground in an agate mortar and annealed for 5 h at 800 °C (5 °C/min) in air.

Sol-gel synthesis route (SG)

The YSZ precursor solution was synthesized as follows. An appropriate amount of 2-propanol and acetylacetone were mixed under stirring at room temperature. Secondly, an appropriate volume of zirconium acetate solution in dilute acetic acid was drop wise added to the mixture. After addition of

zirconium precursor the colorless and transparent solution became yellowish due to the formation of zirconium(IV) acetylacetonate. $Y(NO_3)_3 \cdot 6H_2O$ was then added to the above solution according to the desired stoichiometry of the final product. After complete dissolution of yttrium nitrate the precursor solution was concentrated by slow evaporation at 100 °C under constant stirring. During the last stage of gelation the temperature was increased up to 150 °C and highly viscous orange gel gradually turned into brown-glassy gel. The resulted gels were ground in an agate mortar and sintered for 5 h at 800 °C (5 °C/min) in air.

Deposition of thin films

The same precursor solution obtained by SG method was applied for the deposition of YSZ films. Multilayered YSZ films were prepared on Si(100)/SiO₂ (native layer) substrates by spin-coating technique. In order to reduce the amount of organic compounds, a series of acetylacetonate to total metal ion molar ratio solutions were prepared. The stability of the YSZ precursors with different Acac/M ($M = Y^{3+} + Zr^{4+}$) ratios is illustrated in Table 1.

Table 1. Stability of YSZ precursor solution with different Acac/M ($M = Y^{3+} + Zr^{4+}$) ratio.

Acac/M	0.5	1.0	1.5	2.0	2.5	3.0
Time	<1 h	<1 h	<24 h	<24 h	~24 h	≥week

It was determined that for the preparation of a stable solution, the Acac/M molar ratio should be ~3 and optimal concentration ~3% (w/v). Higher YSZ concentration solutions showed lower stability over the time. Prior deposition the substrates were cleaned with a mixture of concentrated sulfuric acid and hydrogen peroxide. Several drops of YSZ precursor solution were placed onto substrates and spin-coated for 30 s @ 3000 rpm (1000 rpm/s). The as deposited wet film was treated on a hot plate for 5 min at 400 °C. The complete cycle is repeated 1–10 times prior to a final annealing in a muffle furnace at 800 °C for 2 h in air (ramp 2 h).

Thermogravimetric analysis of all zirconium precursors ($Zr(CH_3COO)_x(OH)_y$, $ZrO(NO_3)_2 \cdot xH_2O$ and $Zr^{x+} \cdot xCH_3COOH$) was performed prior the synthesis in order to estimate zirconium content.

2.3. Synthesis of GDC powders and films

GDC powders with gadolinium content 10 mol% (10GDC) were prepared by sol-gel combustion and aqueous sol-gel methods using ethylene glycol (EG), glycerol (GL) and tartaric acid (TA) as complexing agents and fuels.

Sol-gel combustion (SGC) synthesis route

For the synthesis of $Gd_{0.1}Ce_{0.9}O_{1.95}$ powders the appropriate amounts of $Ce(NO_3)_3 \cdot 6H_2O$ and $Gd(NO_3)_3 \cdot xH_2O$ were dissolved in deionized water in a tall beaker followed by the addition of EG, GL or TA as an complexing agents and fuels for self-burning reaction. The amount of fuel was estimated according to the principle of propellant chemistry [123]. Calculations of the oxidizing valences of oxidants and the reducing valences of EG, GL and TA are presented in Table 2.

Table 2. The oxidizing valences of oxidants and the reducing valences of EG, GL and TA.

Compound	Derivation	Valence oxidizing (-) reducing (+)
Oxidizers: $M(NO_3)_3$, M = Ce, Gd	$3 + 3 \times (0 + 3 \times (-2))$	-15
Fuels:		
Ethylene glycol ($C_2H_6O_2$)	$2 \times 4 + 6 \times 1 + 2 \times (-2)$	10
Glycerol ($C_3H_8O_3$)	$3 \times 4 + 8 \times 1 + 3 \times (-2)$	14
Tartaric acid ($C_4H_6O_6$)	$4 \times 4 + 6 \times 1 + 6 \times (-2)$	10

The stoichiometric fuel to oxidant ratio was chosen and calculated EG, GL and TA to metal nitrates ratios were 1.5:1, 1.07:1 and 1.5:1, respectively. The resulted solution was evaporated while continuously stirring at 100 °C. After the sol transformed into transparent gel the temperature of the hot plate

was increased to 250 °C and spontaneous ignition process took place yielding voluminous powders with uniform pale-yellow color (for EG and GL). Using TA as a fuel no intensive combustion has occurred, only slow decomposition of organic parts with emission of reddish-brown gases was observed. Finally, the ashes were collected and annealed in a furnace at different temperatures up to 800 °C in air atmosphere with heating rate of 5 °C/min.

Sol-gel (SG) synthesis route

For the preparation of GDC powders by SG technique the stoichiometric amounts of $\text{Ce}(\text{CH}_3\text{COO})_3 \cdot x\text{H}_2\text{O}$ and $\text{Gd}(\text{CH}_3\text{COO})_3 \cdot x\text{H}_2\text{O}$ were dissolved in deionized water. EG, GL or TA as complexing agents were then added to the above solution in the same ratio as in the sol-gel combustion synthesis route. In the case of TA some precipitates were formed instantly after addition of complexing agent. Therefore, ammonium hydroxide was added up to pH~8 in order to obtain clear solution. The resulted clear solutions were mixed for 1 h at 60 °C and then concentrated by evaporation of solvent at 100 °C until it turned into a viscous turbid (using EG and GL) or reddish transparent (using TA) gel. The resulted gel was dried in the oven overnight, ground in an agate mortar and finally annealed in a furnace under the same conditions as for the sol-gel combustion synthesis.

Deposition of thin films

GDC precursor solution was synthesized by the following procedure. An appropriate amount of $\text{C}_{15}\text{H}_{21}\text{CeO}_6 \cdot x\text{H}_2\text{O}$ and $\text{C}_{15}\text{H}_{21}\text{GdO}_6 \cdot x\text{H}_2\text{O}$ were separately dissolved in a certain amount of methanol at room temperature. Small amount of acetic acid was added drop wise to the above solutions in order to increase a solubility of precursors. The concentrations of cerium and gadolinium in obtained solutions were 0.1 M and 0.05 M, respectively. Starting Ce and Gd solutions were mixed in an appropriate ratio according to the desired stoichiometry of final compound ($\text{Gd}_x\text{Ce}_{1-x}\text{O}_{2-x/2}$, $x = 0, 0.1, 0.15$ and 0.2). Multilayered ceria films were prepared on Si and Si/YSZ substrates by spin-coating technique. Prior deposition Si substrates were cleaned with a mixture of concentrated sulfuric acid and hydrogen peroxide (30%) followed by washing

with deionized water and isopropanol. Several drops of GDC precursor solution were placed onto substrates and spin-coated for 30 s @ 3000 rpm (1000 rpm/s). The as deposited wet film was treated on a hot plate for about 5 min at 400 °C. The complete cycle is repeated 1–18 times prior to a final annealing in a furnace at different temperatures for 2 h (1°C/min).

Thermogravimetric analysis of Ce and Gd precursors ($\text{Gd}(\text{NO}_3)_3 \cdot x\text{H}_2\text{O}$, $\text{Ce}(\text{CH}_3\text{COO})_3 \cdot x\text{H}_2\text{O}$, $\text{Gd}(\text{CH}_3\text{COO})_3 \cdot x\text{H}_2\text{O}$, $\text{C}_{15}\text{H}_{21}\text{CeO}_6 \cdot x\text{H}_2\text{O}$ and $\text{C}_{15}\text{H}_{21}\text{GdO}_6 \cdot x\text{H}_2\text{O}$) was performed prior the synthesis in order to estimate the exact content of crystallization water.

2.4. Elemental analysis of YSZ powders and films

For the spectrophotometric determination of zirconium in YSZ powders the following procedure was established. First, approximately 20 mg of YSZ sample was dissolved in 5 mL of concentrated H_2SO_4 (in the case of films, samples were not weighed). This solution was transferred into a 100 mL volumetric flask and diluted with deionized water. An aliquot of sample solution containing 4–20 μg of Zr was transferred into 50 mL volumetric flask, 1 mL of 2% arsenazo III standard solution was added and diluted with 1:1 solution of HCl. The absorbance was measured at 665 nm against arsenazo III solution.

For the determination of yttrium, an aliquot of YSZ sample solution containing 5–30 μg of Y was transferred into 50 mL volumetric flask, mixed with 1 mL of 2% arsenazo III standard solution, 0.25 mL of working standard solution of nickel and 0.2 mL of working standard solution of EDTA. The pH value was adjusted at ~3 by addition of diluted NH_3 and HCl and solution was diluted up to 50 mL with deionized water. The absorbance of final solution is measured at 655 nm against the reagent blank solution prepared in the same way. Concentrations of Y and Zr in YSZ samples were calculated from the appropriate calibration curve equation.

For the determination of Y and Zr by ICP-OES the same sample preparation procedure was employed with only difference that lower dilution factor was used.

2.5. Elemental analysis of GDC powders and films

The following procedure was employed for the determination of chemical composition of GDC samples. Approximately 20 mg of GDC sample (in the case of films, samples were not weighed) were dissolved in a mixture of 5 mL concentrated HNO_3 and 4 mL H_2O_2 . Resulting transparent colorless solution was transferred into 50 mL volumetric flask and diluted with deionized water. The further spectrophotometric determination of Ce and Gd was carried out in two steps. First, determination of Ce content was performed, which is based on the absorbance of radiation by yellow Ce(IV) solution. For this purpose an aliquot of dissolved sample containing 50–1500 μg of Ce was transferred into 50 mL beaker and 5 mL of 10% $(\text{NH}_4)_2\text{S}_2\text{O}_8$ solution were added followed by few drops of 1% AgNO_3 solution. This mixture was boiled on a hot plate in order to oxidize Ce(III) ions to Ce(IV). The colorless solution transformed into bright yellow. The excess of $(\text{NH}_4)_2\text{S}_2\text{O}_8$ was decomposed by boiling. The solution was evaporated to minimal volume, transferred into 50 mL volumetric flask and diluted with 1 M H_2SO_4 . In such acidic environment Ce(IV) ions are stable in time and do not transform back to reduced form. The absorbance of the final colored solution was measured at 340 nm against 1 M H_2SO_4 reagent blank and concentration of Ce was calculated from the calibration curve equation. The calibration solutions were prepared in the same way. Calculated Ce content value was used for the further determination of Gd.

Determination of Gd is based on the absorbance of Gd(III) and arsenazo III complex. An aliquot of dissolved GDC sample was transferred into 50 mL volumetric flask and 2 mL of 0.05% arsenazo III standard solution were added. The pH value was adjusted at ~ 3 by addition of diluted NH_3 and H_2SO_4 and solution was diluted up to 50 mL with deionized water. The absorbance of the final colored solution was measured at 665 nm against deionized water. Whereas Ce(III) ions also form complex with arsenazo III, which absorbs in the same spectrum region, the sum absorbance of Gd(III) and Ce(III) complexes with arsenazo III was measured. At the same time a solution containing certain

amount of Ce (determined by mentioned above procedure) and arsenazo III also was prepared. The absorbance of gadolinium complex is calculated by subtracting absorbance value of Ce complex from the sum absorbance. The concentration of Gd was calculated from the calibration curve equation.

For the determination of Ce and Gd content by ICP-OES, GDC samples were dissolved by the above mentioned procedure, diluted by appropriate dilution factor with 2% HNO₃ and analyzed.

2.6. Instrumentation and characterization techniques

TG-DSC analysis. The thermal decomposition of the precursor gels, co-precipitated species and starting materials were analyzed through thermogravimetric analysis and differential scanning calorimetry (TG-DSC) using Perkin Elmer STA 6000 Simultaneous Thermal Analyzer. Dried samples of about 5–10 mg were heated from 25 to 950 °C at a heating rate of 10 °C/min in a dry flowing air (20 mL/min).

Powder X-ray Diffraction. Powder X-ray diffraction data were collected using Ni-filtered Cu K_α radiation on Rigaku MiniFlex II diffractometer working in Bragg-Brentano ($\theta/2\theta$) geometry. The step width and integration time was 0.02° and 1 s, respectively. The size of crystallites was calculated by Scherrer equation:

$$\tau = \frac{0.9\lambda}{B\cos\theta} \quad (\text{Eq.13})$$

where τ is the mean crystallite size, λ is the X-ray wavelength, B is the line broadening at half maximum intensity (FWHM) and θ is the Bragg angle.

FTIR Analysis. IR spectra were taken with PerkinElmer Frontier ATR-FTIR spectrometer equipped with a liquid nitrogen cooled MCT detector.

SEM analysis. The morphology of the samples was characterized by scanning electron microscopy performed with a Hitachi SU-70 field-emission scanning electron microscope (FE-SEM).

XPS analysis. XPS measurements of synthesized GDC powders and films were carried out to obtain information about the chemical state of cerium

employing the upgraded Vacuum Generator (VG) ESCALAB MKII spectrometer fitted with a new XR4 twin anode. The non-monochromatized MgK α X-ray source was operated at $h\nu = 1253.6$ eV with 300 W power (20mA/15kV) and the pressure in the analysis chamber was lower than $5 \cdot 10^{-7}$ Pa during spectral acquisition. The spectra were acquired with an electron analyzer pass energy of 20 eV for narrow scans and resolution of 0.05 eV. All spectra were recorded at a 90° take-off angle and calibrated from the hydrocarbon contamination using the C 1s peak at 284.6 eV. The spectra calibration, processing and fitting routines were done using Avantage software (5.918) provided by Thermo VG Scientific. Core level peaks of Ce 3d and C 1s were analyzed using a nonlinear Shirley-type background.

Impedance spectroscopy. In order to study electrical conductivity of the synthesized materials, the specimens have been prepared by uniaxial pressing powders under 200 MPa. Subsequently, the pellets were sintered at 1500 °C and 1300 °C (2 h) for YSZ and GDC, respectively, with the heating and cooling rate of 3 °C/min. The cylindrical-shape samples (thickness 1.5 mm, \varnothing 2 mm) were prepared and Pt paste electrodes were applied for the impedance spectroscopy investigations. The impedance spectra have been obtained by using two custom spectrometers. The first allowed to measure impedance by two-electrode method in the frequency range of 10 Hz to 10 GHz and 300–800 K temperature range. The method used for these measurements has been presented in [124]. Due to the big influence of platinum electrodes on impedance spectra, the second impedance spectrometer, which operates by 4-electrode method, was used and impedance spectra were obtained in the frequency range from 10 Hz to 2 MHz as described in [125].

Spectrophotometric measurements. Elemental analysis of synthesized samples was performed using a Perkin-Elmer Lambda 35 UV-Vis and Analytik Jena Specord 200 plus spectrometers and KFK-3 photometer.

ICP-OES analysis. For the determination of element ratio in the synthesized samples inductively coupled plasma optical emission spectrometry was employed using Perkin-Elmer Optima 7000 DV spectrometer.

AFM analysis. For the surface characterization of deposited films, an atomic force microscope (AFM) BioScope Catalyst from Bruker was used. The contact mode was employed and sharpened silicon nitride (DNP-S type) AFM probes were applied.

UV-Vis measurements. Diffuse reflectance spectra were recorded at room temperature on a Perkin-Elmer Lambda 35 UV-Vis spectrophotometer equipped with an integrating sphere accessory and Edinburgh Instruments FLS980 fluorescence spectrometer equipped with an integration sphere coated with Teflon. Teflon was also used as a white standard.

Raman spectroscopy. Raman spectroscopy measurements were performed at room temperature using combined Raman and scanning near-field optical microscope (SNOM) WiTec Alpha 300 R equipped with 532 nm excitation laser source.

BET analysis. Specific surface area of powders was measured using a surface area analyzer Micrometrics TriStar II 3020 based on Brunauer-Emmett-Teller (BET) principle and nitrogen adsorption.

3. RESULTS AND DISCUSSION

3.1. Synthesis and characterization of yttria-stabilized zirconia

3.1.1. Three different synthesis techniques to the bulk ceramics

Thermal analysis

The thermal decomposition behavior of Y-Zr-O gels and precipitated Y-Zr-oxalate, corresponding to the final composition of $(Y_2O_3)_{0.08}(ZrO_2)_{0.92}$, were investigated by simultaneous TG-DSC measurements. The TG-DSC curves of precipitated Y-Zr oxalate are shown in Fig. 7.

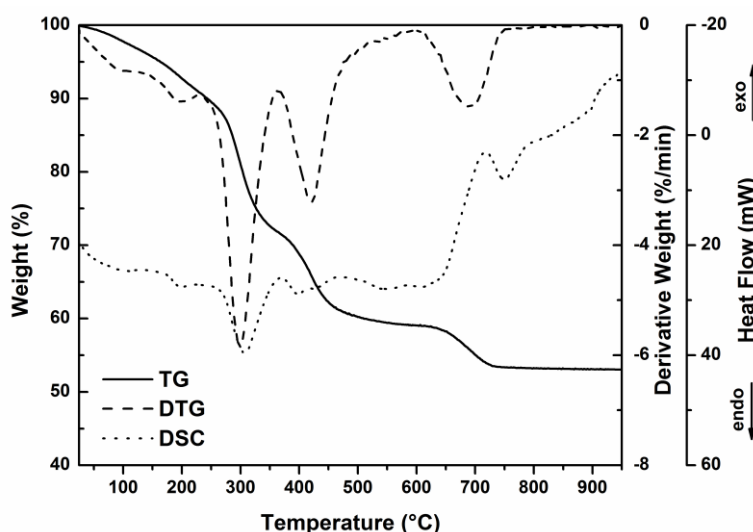


Fig. 7. TG-DSC curves of Y-Zr oxalate precipitate.

The thermal decomposition of the Y-Zr oxalate precipitate passes through five stages. Two endothermic peaks in DSC curve in temperature range 25–230 °C is due to the removal of adsorbed and hydrated water. The weight loss of ~19% in temperature interval 230–362 °C is attributed to decomposition of zirconyl oxalate ($ZrOC_2O_4$) to form intermediate carbonate species ($ZrOCO_3$). This is in a good agreement with results published by Drozd-Ciesla *et al.* [126]. The fourth weight change in the temperature range 360–490 °C is attributed to the simultaneous decomposition of residual $ZrOCO_3$ and $Y_2(C_2O_4)_3$. As a result, amorphous zirconium oxide (ZrO_2) and various carbonate-oxalates, and oxy-carbonates are formed [127, 128]. The weak exothermic signal in DSC curve

peaked at 470 °C can be ascribed to the amorphous zirconia crystallization stage [129]. The final weight loss of ~6% in the temperature range 600–760 °C indicates a decomposition of thermally stable $Y_2O_2CO_3$. The exothermic peak above 600 °C in DSC curve is attributed to amorphous-crystalline phase transition in Y_2O_3 . Such exothermic peaks were observed in nearly all rare earth metal oxalates studied by Wendlandt *et al.*[130]. In conclusion, the TG analysis of precipitated Y-Zr oxalate revealed that two separate phases are formed in different temperature ranges. The TG-DSC curves of Y-Zr-O gel synthesized by SGC method are plotted in Fig. 8.

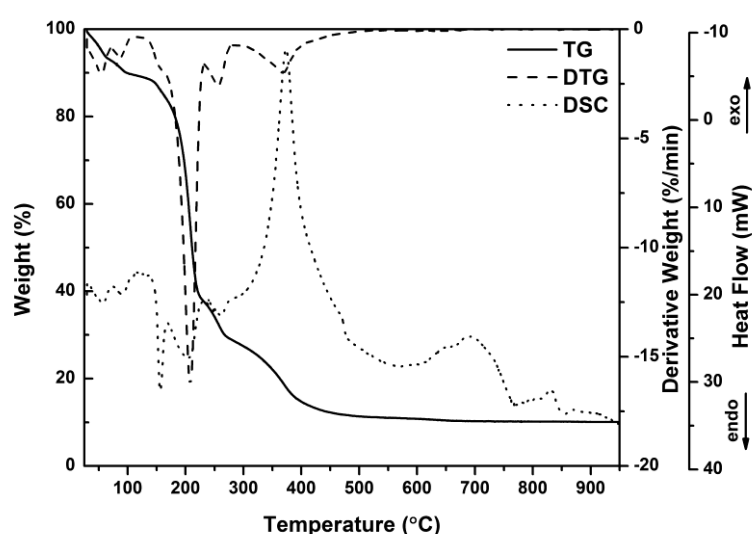


Fig. 8. TG-DSC curves of Y-Zr-O precursor gel obtained by SGC route.

The decomposition process of citrate-nitrate gel can be divided into four major steps. The first weight loss (~10%) in the TG curve from room temperature to ~130 °C is due to the loss of residual water in the gel. The second and most prominent weight loss (~50%) peaked at 207 °C in the DTG curve can be ascribed to the decomposition of citrate matrix. The endothermic peak at 156 °C in the DSC curve indicates that citric acid undergoes melting before decomposition occurs [131]. The third weight loss (~10%) can be associated with decomposition of intermediate products [132]. The residual organic compounds are oxidized at higher temperature yielding a strong exothermic signal peaked at 372 °C in the DSC curve [133]. The final negligible weight

change (~1%) is ascribed to the removal of elemental carbon. No more weight changes are observed above 700 °C, indicating that all organic residues are decomposed at this point. The thermal behavior of the Y-Zr-O precursor gel synthesized by SG process is illustrated on Fig. 9.

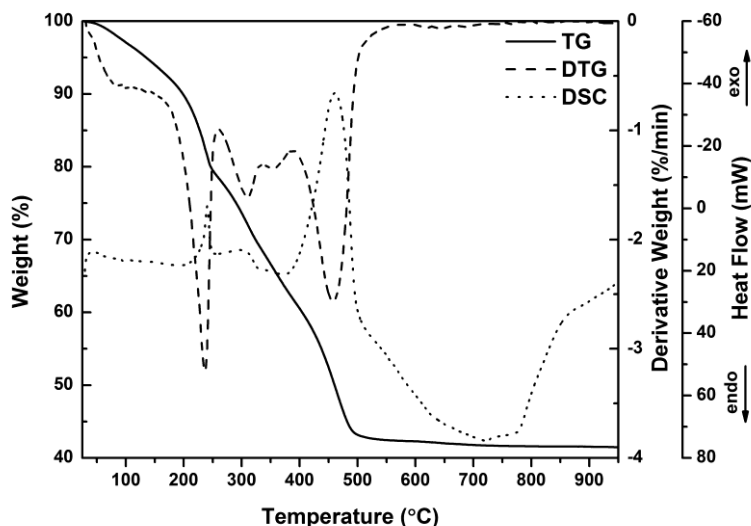


Fig. 9. TG-DSC curves of Y-Zr-O precursor gel obtained by SG route.

The obtained results demonstrate that thermal decomposition occurs in five steps. In the temperature range of 25–100 °C the absorbed water and volatile compounds are removed from the gel (~8% of the initial weight). The second weight loss peaked at 238 °C in the DTG curve can be ascribed to the complete degradation of acetylacetonate ligands and formation of intermediate species of $\text{ZrO}(\text{CH}_3\text{COO})_2$ [134]. During the third step in temperature range of 260–390 °C acetate groups are decomposed leading to the formation of ZrOCO_3 . The fourth weight loss in the TG curve (~25%) is accompanied by the strongest exothermic signal in DSC curve peaked at 463 °C. It is associated with oxidation of residual acetates by nitrate ions and simultaneous decomposition of ZrOCO_3 . The last and barely visible weight loss (~1.5%) from 500 up to 800 °C is due to the removal of elemental carbon from final compound. The complete elimination of carbon occurs at 800 °C that is 100 °C higher if compared to SGC route.

Powder X-ray diffraction analysis

The phase crystallinity and purity of all samples were characterized by means of XRD analysis. The representative XRD patterns of YSZ specimens obtained by CP method and annealed at 800 °C for 5 h are shown in Fig. 10a.

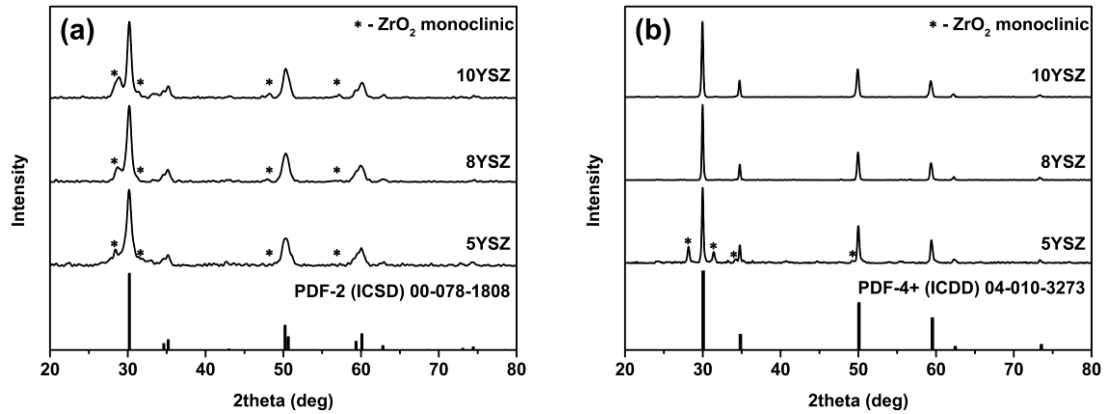


Fig. 10. Powder XRD patterns of YSZ samples prepared by CP synthesis route and annealed at 800 °C (a) and 1500 °C (b).

The formation of two phases attributed to tetragonal zirconia (ICSD#00-078-1808) and monoclinic zirconia (ICSD#00-086-1451) was observed in all samples despite of the chemical composition. The powder XRD analysis revealed that single phase cubic zirconia with fluorite-type crystal structure was not obtained at 800 °C. Therefore, the samples were annealed at elevated temperatures. It was found that the temperature of 1500 °C is necessary to obtain single phase cubic zirconia of 8YSZ and 10YSZ (Fig. 10b). However, in the case of 5YSZ sample the mixture of cubic and monoclinic zirconia was observed after the same thermal treatment. The narrow reflection peaks of samples annealed at 1500 °C suggest about higher degree of crystallinity in comparison to those which were annealed at 800 °C. The XRD patterns of the final YSZ powders with different content of Y_2O_3 obtained by SGC technique and annealed at 800 °C are depicted in Fig. 11a.

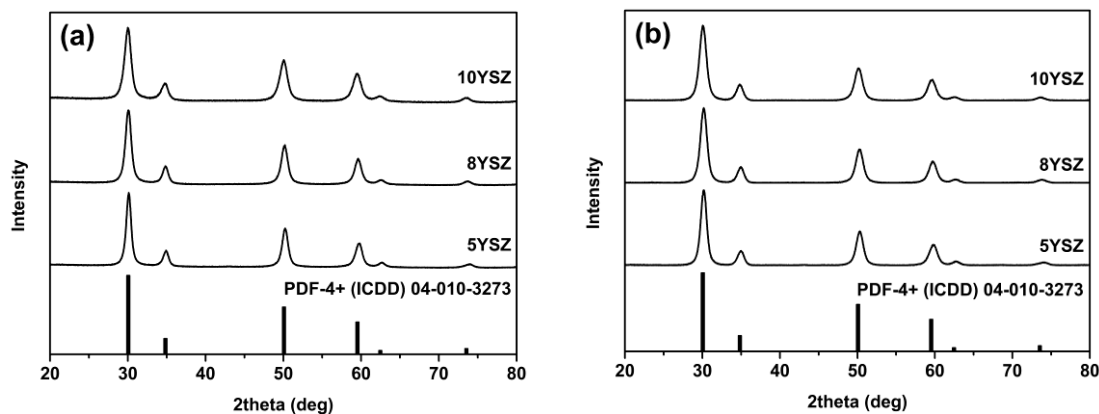


Fig. 11. Powder XRD patterns of YSZ samples prepared by SGC (a) and SG (b) synthesis routes and annealed at 800 °C.

All the diffraction peaks are indexed to the cubic zirconia with fluorite-type crystal structure and match very well the standard XRD data of ICDD#04-010-3273. However, the characteristic reflections for tetragonal and cubic phases are located at nearly overlapping angles, the diffraction pattern of 5YSZ sample could be attributed to the cubic and/or tetragonal phases [135]. According to the literature, the introduction of higher yttrium content into zirconia lattice leads to the formation of cubic phase [24]. The powder XRD patterns of different stoichiometry YSZ samples obtained by SG process are given in Fig. 11b. The XRD patterns are nearly identical to those obtained by SGC method (Fig. 11a). All the peaks can be assigned to the cubic zirconia and are in a good agreement with standard powder XRD data of ICDD#04-010-3273. No X-ray reflections arising from by-products such as yttrium oxide (Y_2O_3) or monoclinic zirconia (ZrO_2) are observed after annealing the powders at 800 °C indicating the high phase purity of synthesis products.

Based on the obtained XRD results we can conclude that the phase formation mechanism in co-precipitated specimens is similar to the traditional solid state reaction synthesis route, where much higher temperatures are necessary to obtain single phase compound.

SEM analysis

The morphology of synthesized YSZ powder samples were examined by scanning electron microscopy. The SEM micrographs of 8YSZ sample synthesized by CP method and annealed at 1500 °C are shown in Fig. 12a.

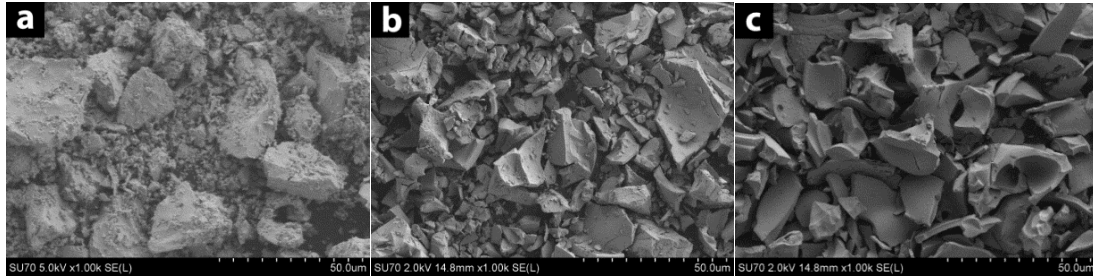


Fig. 12. SEM micrographs of 8YSZ powders synthesized by CP (a), SGC (b), SG (c) methods and annealed at 1500, 800 and 800 °C, respectively.

The SEM images clearly demonstrate that the powders consist of irregular shape agglomerates (10–30 μm) covered by smaller particles. However, the 8YSZ powders prepared by SGC method exhibit different morphological features (Fig. 12b). After calcination at 800 °C blocky angular shape particles were obtained. Moreover, the abundance of small particles decreased in comparison to CP method. Fig. 12c shows that powders synthesized by SG procedure and annealed at 800 °C consist of plate like monoliths with a flat surface. The variation in stoichiometry of the final compounds did not result in any significant morphological changes for each synthesis techniques. Fig. 13 represents the SEM images of 8YSZ pellets sintered at 1500 °C for 2 h.

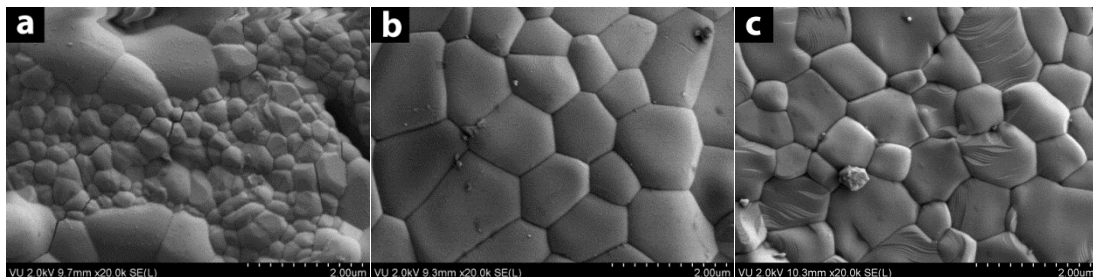


Fig. 13. SEM micrographs of 8YSZ pellets pressed from powders synthesized by CP (a), SGC (b), SG (c) methods and sintered at 1500 °C.

It is obvious that the pellet pressed from the powders prepared by CP method (Fig. 13a) is composed of smaller (0.2–0.5 μm) and significantly larger (1–2 μm) grains. The last ones tend to aggregate with each other to form island-like structure. Numerous interspaces and cracks are observed on the surface suggesting about the poor quality of ceramic sample. The pellets obtained by SGC and SG techniques (Fig. 13b, c) possess similar morphology. The dense ceramics with low porosity were obtained in both cases. However, the average grain size for SGC route is slightly larger (1–2 μm) and more uniform corresponding to a smaller grain boundary volume.

Electrical properties of YSZ ceramics

Two relaxation processes were observed in the impedance spectra of YSZ ceramics sintered from SG and SGC powders. The dispersion in the lower frequency range was attributed to the oxygen ion transport in the grain boundaries of the ceramics, while the dispersion in the higher frequencies – to the oxygen ion transport in the ceramics bulk. Each of the above mentioned processes is observed as a semicircle in the complex resistivity ($\tilde{\rho} = \tilde{Z} \frac{S}{l}$, where \tilde{Z} is impedance, S is electrode surface area and l – length of the sample) plot (Fig. 14), besides, the diameters of the semicircles are equal to bulk (ρ_b) and grain boundary (ρ_{gb}) resistivities, respectively. It should be noted, that the processes at the electrode-YSZ interface do not influence impedance spectra because of the four-electrode method used at low frequencies. The bulk resistivity values of SG and SGC ceramics are almost identical, while the lowest grain boundary resistivity values for ceramics sintered from SGC powders were found. Only one huge and deformed semicircle can be observed in $\rho''(\rho')$ plot for ceramics sintered from CP powders. Numerous cracks and big distribution of ceramic grain sizes contribute to the grain boundary resistivity arc. In this case the poorly conducting ceramics grain boundaries govern all the spectrum and the bulk conductivities could not be extracted from the impedance data.

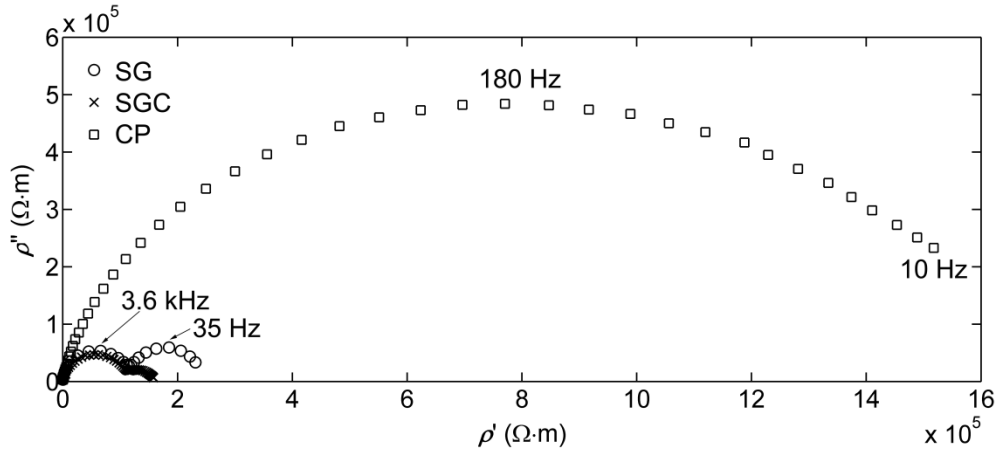


Fig. 14. Complex resistivity plot at 500 K of 8YSZ obtained by different methods (CP, SGC and SG).

Temperature dependences of the bulk ($\sigma_b = \frac{1}{\rho_b}$) and grain boundary ($\sigma_{gb} = \frac{1}{\rho_{gb}}$) conductivities are shown in Fig. 15. All the conductivities obey Arrhenius law: $\sigma_{b,gb} = \sigma_0 \exp \frac{-\Delta E_{b,gb}}{kT}$, where σ_0 is preexponential factor, k – Boltzmann constant, T – temperature and $\Delta E_{b,gb}$ – activation energies of bulk and grain boundary conductivities, respectively. The obtained conductivities correlate well with the microstructure of the obtained ceramics – the highest grain boundary conductivities have been found for ceramics prepared by SGC route, where the ceramic grains are larger.

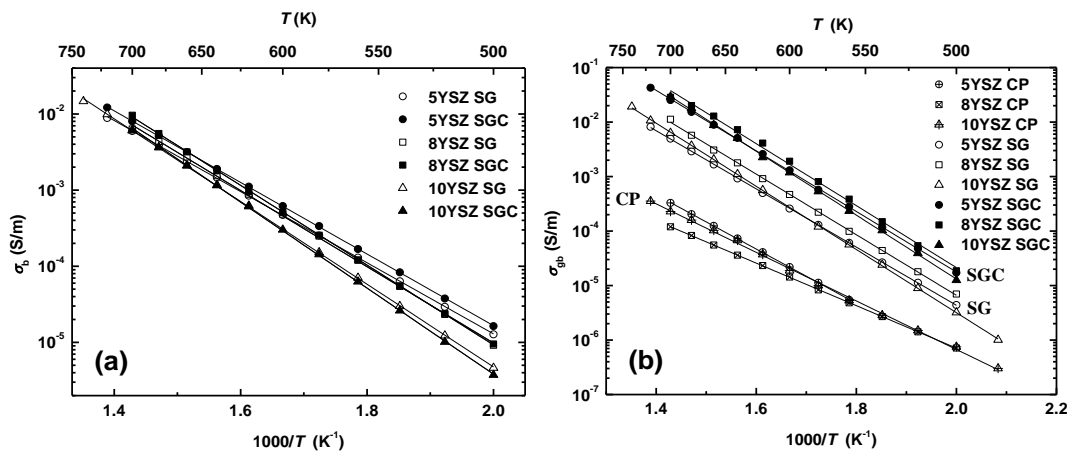


Fig. 15. Temperature dependences of bulk (a) and grain boundary (b) conductivities of YSZ ceramics. Solid lines are the fits in accordance with Arrhenius law.

The bulk conductivity of the ceramics and its activation energy (see the summary in Table 3) almost do not depend on the powder preparation method. The highest bulk conductivity was found for 5YSZ, but the conductivity of 8YSZ is also comparable. The activation energy of the bulk conductivity increases with increase of Y_2O_3 amount. Our results are in a good agreement with the literature data [136, 137].

Table 3. Summary of activation energies of bulk and grain boundary conductivities of YSZ ceramics.

Preparation method Sample	SG		SGC		CP	
	ΔE_b , eV	ΔE_{gb} , eV	ΔE_b , eV	ΔE_{gb} , eV	ΔE_b , eV	ΔE_{gb} , eV
5YSZ	0.93	1.07	0.90	1.11		1.00
8YSZ	1.00	1.11	1.05	1.14		0.78
10YSZ	1.09	1.16	1.13	1.17		0.89

The values of the grain boundary conductivities usually show the quality of the obtained ceramics. A clear dependence of σ_{gb} on the method used for the synthesis of the powder was found. The highest grain boundary conductivities were found for ceramics prepared from SGC synthesized powders, while the lowest σ_{gb} values are for ceramics sintered from CP powders. The low grain boundary conductivity can be caused by low obtained ceramics density. Not only the quality of the ceramics is indicated by σ_{gb} but also the amount of phase stabilizing Y_2O_3 affects the grain boundary conductivity of the ceramics. The highest σ_{gb} for Y_2O_3 content of 8 mol% within the synthesis method was found.

3.1.2. Deposition of thin films

The precursor solution obtained by SG method was successfully applied for the deposition of YSZ thin films on Si substrates by spin-coating technique. As seen from Fig. 16, all diffraction lines of 8YSZ film correspond to monophasic cubic zirconia. No tetragonal or monoclinic YSZ phases were detected after calcination at 800 °C.

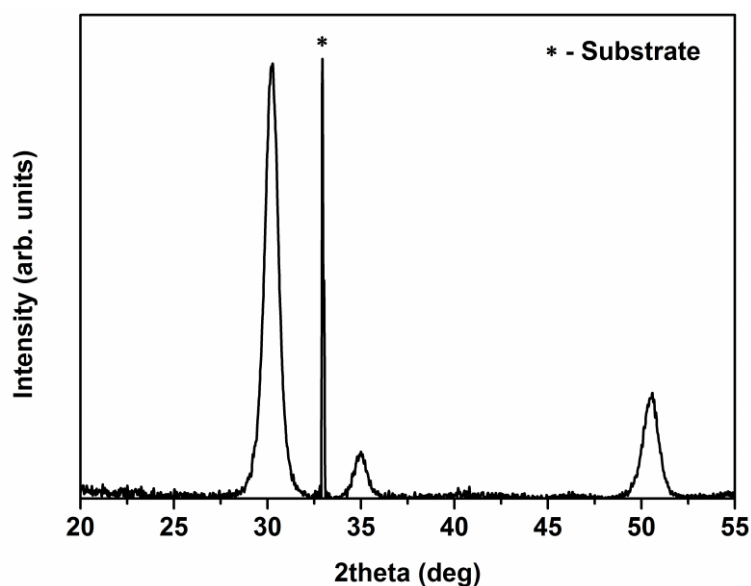


Fig. 16. XRD pattern of a 10-layered 8YSZ film deposited on Si substrate annealed at 800 °C.

Plane view SEM images of the deposited 8YSZ film with different magnifications are shown in Fig. 17(a, b). As can be seen, smooth, uniform and homogeneous YSZ films have been formed. However, some individual cracks are observed on the surface. These cracks are formed due to the release of gases during decomposition of organic matters that remained after hot plate treatment at 400 °C. The TG curve presented in Fig. 3 confirms the presence of organic residues at this temperature. The crack formation could be avoided by performing a heat treatment of each layer at elevated temperature. Cross-section SEM image of a 10-layered 8YSZ film is presented in Fig. 17c.

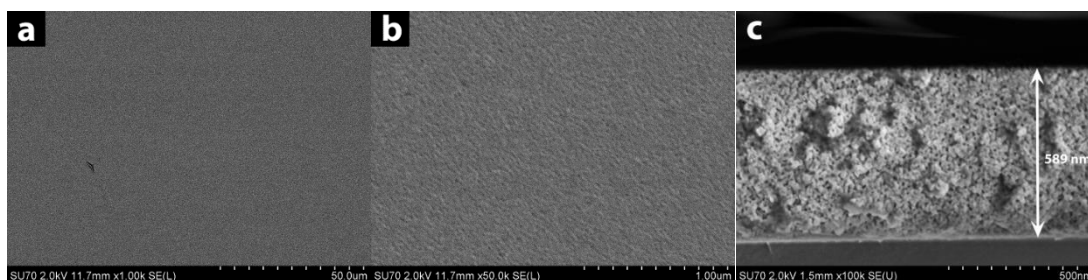


Fig. 17. Plane view (a, b) and cross-section (c) SEM images of a 10-layered 8YSZ film annealed at 800 °C.

The SEM micrograph clearly shows the formation of a porous film, however, for the practical application as an electrolyte in SOFC the YSZ layer has to be dense and gas-tight. The porosity can be reduced by increasing sintering temperature [138] or laser treatment [139]. Such porous nanocrystalline films can be used for low-temperature applications with proton conductivity [28].

A linear relation between the thickness of the YSZ films and the number of deposited layers was observed (Fig. 18). The thickness of YSZ films can be controlled by applying a certain number of spin-coating cycles and/or by varying the starting precursor concentration. The single layer thickness was determined to be in a range of 50–60 nm for each deposition step using ~3% (w/v) YSZ precursor solution.

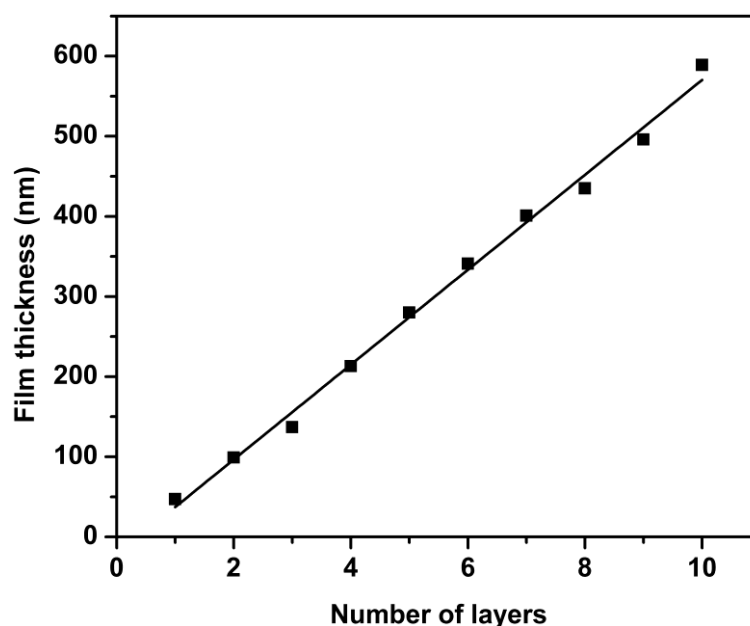


Fig. 18. The dependence of film thickness on the number of layers.

The AFM images of a 10-layered 8YSZ film are shown in Fig. 19. The roughness of YSZ surface was estimated by the calculation of root mean square (RMS) of height values. The RMS roughness of the deposited film was found to be about 1.7 nm.

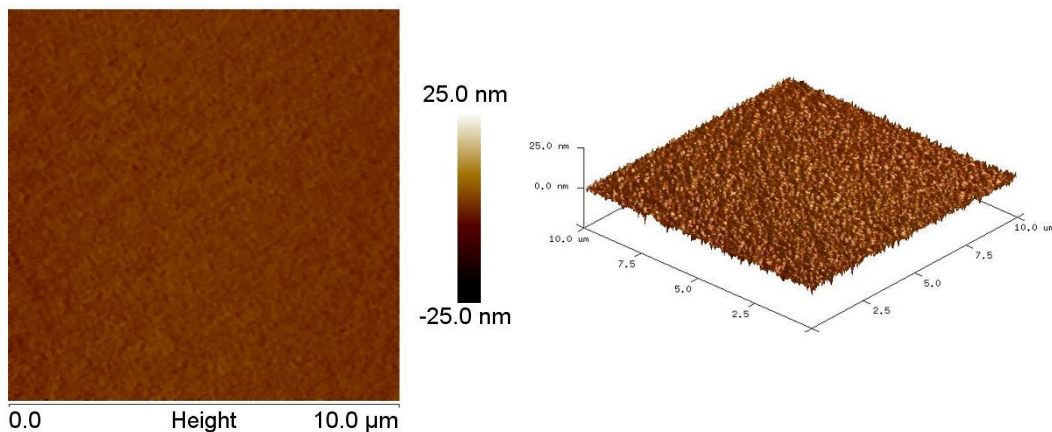


Fig. 19. 2D and 3D AFM images of a 10-layered 8YSZ film.

3.1.3. Development of analytical techniques

For the spectrophotometric determination of Y and Zr in YSZ powders and films the complexation reactions of these metals with arsenazo III were investigated. The solution absorption spectra of arsenazo III and its complexes with zirconium and yttrium are shown in Fig. 20.

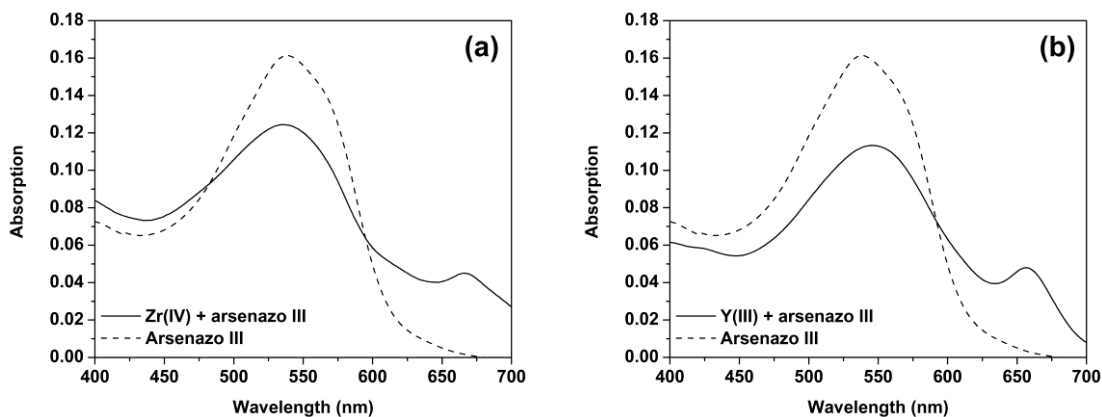


Fig. 20. Absorption spectra of arsenazo III ($c = 0.04\%$) and Zr ($c_{Zr} = 0.3 \mu\text{g/mL}$) with arsenazo III ($c = 0.04\%$) solutions (a); absorption spectra of arsenazo III ($c = 0.04\%$) and Y ($c_Y = 0.4 \mu\text{g/mL}$) with arsenazo III ($c = 0.04\%$) solutions (b).

As seen from Fig. 20a, the formation of complex between Zr and arsenazo III occurred with absorption maximum located around 665 nm. Evidently, the solution of arsenazo III does not absorb at this wavelength. Absorption maximum for the complex of Y and arsenazo III was observed at slightly shorter wavelength (~655 nm; see Fig. 20b).

An attempt was also made to examine the effects of interfering species on the spectrophotometric determination of Zr and Y. In order to determine the selectivity of the method, solutions containing Zr(IV) and Y(III) ions were prepared and analyzed. From these investigations it was determined that Y ions do not affect the absorption behavior of Zr and arsenazo III complex at 665 nm (see Fig. 21a). However, the absorption of Y-arsenazo III complex solution at 655 nm increased significantly in the presence of Zr(IV) ions (Fig. 21b).

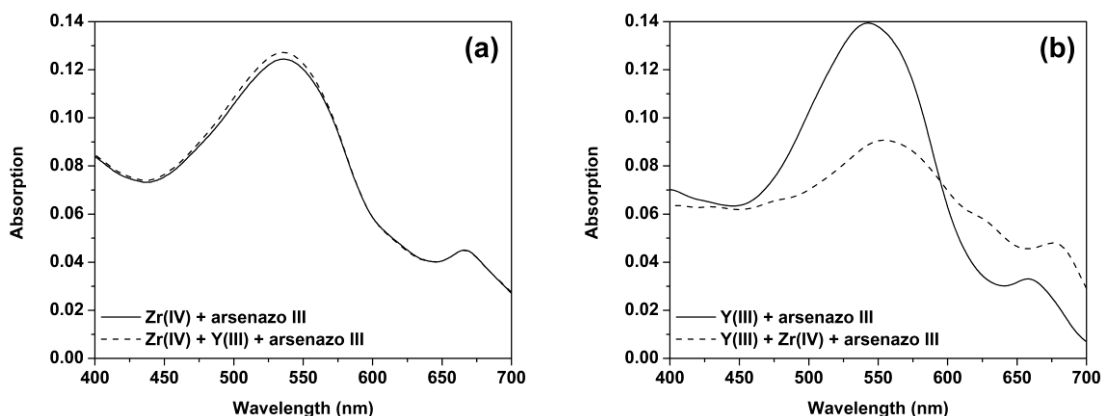


Fig. 21. Absorption spectra of arsenazo III ($c = 0.04\%$) with Zr ($c_{Zr} = 2 \mu\text{g/mL}$) and arsenazo III ($c = 0.04\%$) with Zr ($c_{Zr} = 2 \mu\text{g/mL}$) and Y ($c_Y = 0.3 \mu\text{g/mL}$) solutions (a); absorption spectra of arsenazo III ($c = 0.04\%$) with Y ($c_Y = 0.3 \mu\text{g/mL}$) and arsenazo III ($c = 0.04\%$) with Y ($c_Y = 0.3 \mu\text{g/mL}$) and Zr ($c_{Zr} = 2 \mu\text{g/mL}$) solutions (b).

To eliminate the interfering effect of Zr, a very simple and effective analytical approach was suggested. It was found that Zr does not react with arsenazo III in the presence of excess of EDTA, since Zr is forming very stable complexes with EDTA [140]. On the other hand, yttrium at the same conditions also formed a rather stable complex with EDTA, thus significantly influencing the analytical

signal. Thus, for the successful determination of yttrium the excess of EDTA should be eliminated by using an appropriate masking reagent. We found that nickel removes the excess of EDTA, and at the same time does not form a colored complex with arsenazo III. Fig. 22 shows absorption spectra of a mixture containing arsenazo III, yttrium, nickel and EDTA with and without zirconium. Evidently, the influence of zirconium on the spectrophotometric determination of Y with arsenazo III was eliminated through additional complexation reactions with EDTA and Ni.

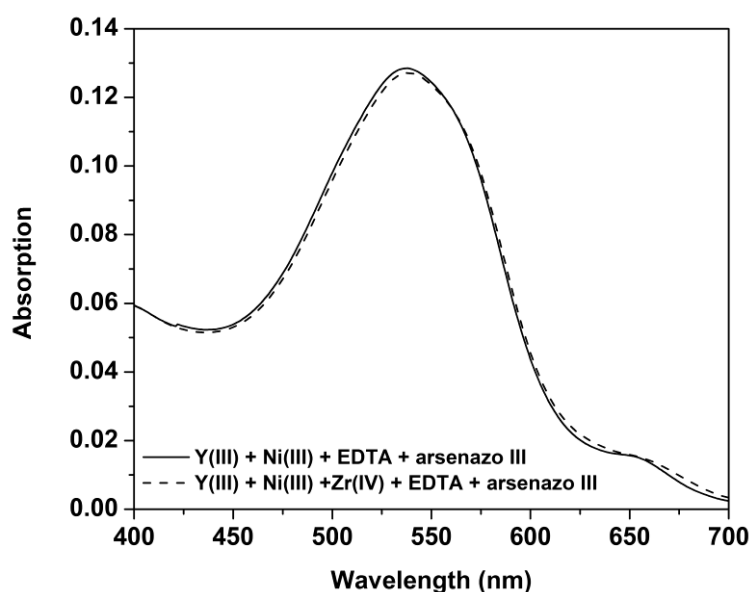


Fig. 22. Absorption spectra of solutions: arsenazo III ($c = 0.04\%$), Y ($c_Y = 0.2 \mu\text{g/mL}$), Ni ($c_{\text{Ni}} = 5 \cdot 10^{-5} \text{ mol/L}$) and EDTA ($c = 4 \cdot 10^{-5} \text{ mol/L}$) and arsenazo III ($c = 0.04\%$), Y ($c_Y = 0.2 \mu\text{g/mL}$), Ni ($c_{\text{Ni}} = 5 \cdot 10^{-5} \text{ mol/L}$), EDTA ($c = 4 \cdot 10^{-5} \text{ mol/L}$) and Zr ($c_{\text{Zr}} = 3 \mu\text{g/mL}$).

The calibration curves obtained under optimal conditions showed a linear correlation in concentration ranges of $0.08\text{--}0.4 \mu\text{g/mL}$ for Zr and $0.1\text{--}0.6 \mu\text{g/mL}$ for Y. Pearson's correlation coefficient r was determined to be 0.9993 and 0.9991 for Zr and Y, respectively.

Determination of Zr and Y was performed in synthesized YSZ powders and thin films. For comparison, commercial YSZ powders (TOSOH) with known chemical composition were also analyzed. Results obtained for Zr and Y

in different samples as a molar ratio of oxides are summarized in Table 4. The sum of ZrO₂ and Y₂O₃ was assumed as 100%. All the samples were parallel analyzed by means of ICP-OES.

Table 4. Results of Zr and Y determination in YSZ powders and films (n = 5).

Sample	Spectrophotometric	ICP-OES
	ZrO ₂ : Y ₂ O ₃	ZrO ₂ : Y ₂ O ₃
5YSZ CP	95.4 : 4.6	95.3 : 4.7
8YSZ CP	92.4 : 7.6	92.5 : 7.5
10YSZ CP	89.5 : 10.5	89.7 : 10.3
5YSZ SGC	95.2 : 4.8	95.1 : 4.9
8YSZ SGC	91.5 : 8.5	91.8 : 8.2
10YSZ SGC	90.5 : 9.5	90.0 : 10.0
5YSZ SG	95.3 : 4.7	95.2 : 4.8
8YSZ SG	92.3 : 7.7	92.0 : 8.0
10YSZ SG	90.3 : 9.7	90.2 : 9.8
5YSZ film	94.9 : 5.1	95.1 : 4.9
8YSZ film	92.4 : 7.6	92.0 : 8.0
10YSZ film	89.7 : 10.3	89.8 : 10.2
8YSZ (TOSOH)	91.7 : 8.3	92.0 : 8.0

It was found that concentration of Y₂O₃ in analyzed YSZ samples ranged between 4.6 and 5.1 mol% for 5YSZ, 7.6 and 8.5 mol% for 8YSZ and 9.5 and 10.5 mol% for 10YSZ. Concentration of ZrO₂ appropriately ranged between 94.9 and 95.4 mol% for 5YSZ, 91.6 and 92.4 mol% for 8YSZ and 89.5 and 90.5 mol% for 10YSZ samples. Comparison of the results obtained by spectrophotometric method, results obtained by ICP-OES and the nominal composition of Y-Zr-O precursor gels or commercial samples suggested a satisfactory agreement. The relative standard deviation (RSD) for Zr (n = 5) was in the range from 0.6 to 4.5%, and for Y it was from 0.6 to 3.6%. The results of Table 4 confirm that suggested spectrophotometric methodology can be successfully applied for the determination of Zr and Y in YSZ samples. The proposed procedure is fast, selective and requires little effort. Moreover, the determined RSD values were quite small, indicating a good accuracy of the developed method.

3.2. Synthesis and characterization of gadolinium doped ceria

3.2.1. Two different synthesis techniques to the bulk ceramics

Thermal analysis

The thermal decomposition behavior of Gd-Ce-O gels, corresponding to the final composition of $\text{Gd}_{0.1}\text{Ce}_{0.9}\text{O}_{1.95}$, was investigated by simultaneous TG-DSC measurements. The TG-DSC curves of the Gd-Ce-O precursor gels synthesized by SGC-EG and SG-EG processes are shown in Fig. 23.

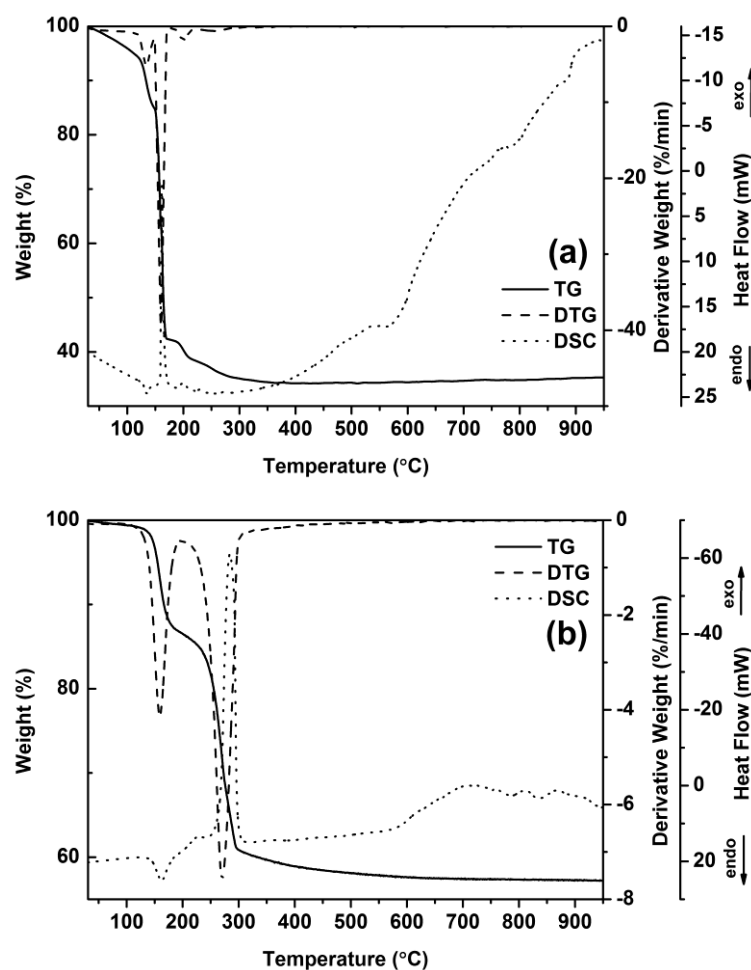


Fig. 23. TG-DSC curves of Gd-Ce-O precursor gels obtained by SGC-EG (a) and SG-EG (b) synthesis routes.

For the Gd-Ce-O precursor gel obtained by SGC-EG route (see Fig. 23a), the first weight loss of about 5% in the TG curve was observed from room temperature to about 130 °C, and is due to the loss of residual water in the gel. The sharp exothermic peak in the DSC curve with its maximum at 160 °C

accompanied by a drastic weight loss in the TG curve indicates that auto-combustion reaction occurs during the degradation of the gel. Furthermore, this exothermic peak was also caused by the oxidation of Ce compounds and formation of CeO₂. The weight loss observed in the temperature range from 170 to 350 °C is attributed to the decomposition of residual organic parts of the gel. It should be noticed, that a non-significant weight gain (about 1%) is observed above 350 °C, which can be attributed to the change of valence state of cerium (Ce(III)→Ce(IV)) according to the possible reaction:



Similar phenomenon was previously noticed by Mahata *et. al.* [141]. The thermal behavior of the Gd-Ce-O precursor gel synthesized by SG-EG process is illustrated in Fig. 23b. It is clearly seen that thermal decomposition of glycolate-acetate gel occurs in two major steps. The first weight loss of about 13% corresponding to the endothermic peak at 160 °C in the DSC curve could be attributed to the removal of water and free ethylene glycol [142]. With further increase of temperature the second weight loss of about 25% occurs at the temperature range from 210 to 310 °C. This weight loss accompanied by a strong exothermic signal with its maximum at 280 °C is assigned to the decomposition of acetates and glycolates, that is in a good agreement with a previously published results [143, 144]. The residual organics slowly decompose with increasing temperature up to 600 °C. Afterwards, the weight of residual GDC precursor remains constant, what indicates that the decomposition and combustion of all organic components in the precursor have been completed below 600 °C. Fig. 24 shows the TG-DSC data of Gd-Ce-O precursor gels obtained by SGC-GL and SG-GL processing routes. Again, the initial weight loss in TG curve of Gd-Ce-O precursor gel obtained by SGC-GL route is attributed to the removal of residual water. Following sharp and strong exothermic peak in the DSC curve with maximum at 170 °C associated with abrupt weight loss in TG curve corresponds to the combustion process.

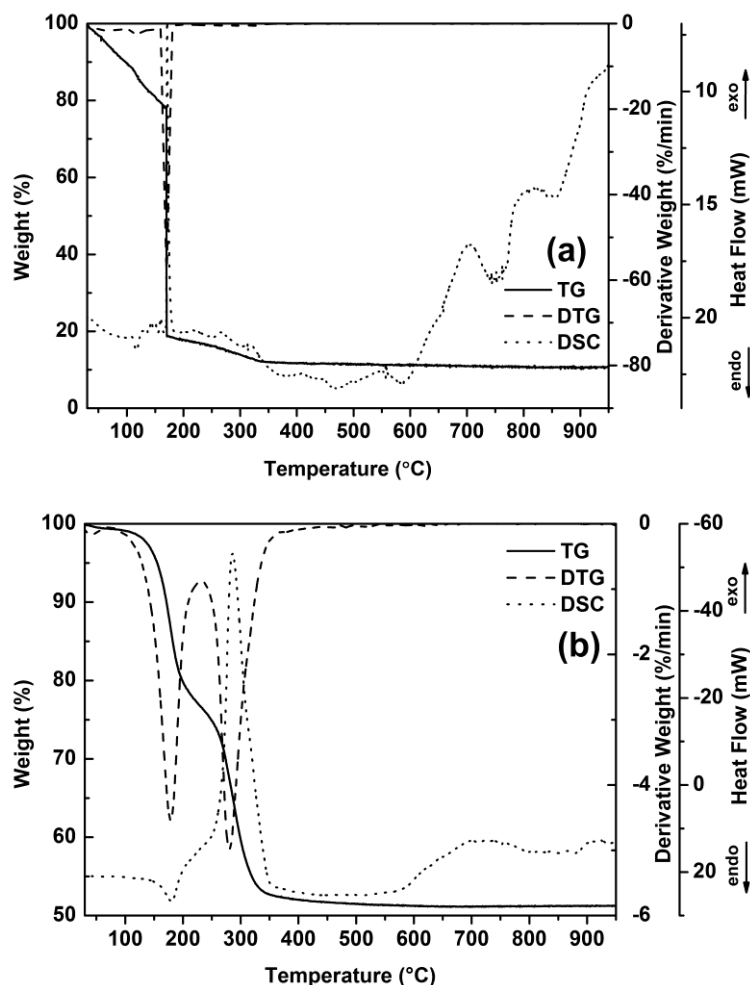


Fig. 24. TG-DSC curves of Gd-Ce-O precursor gels obtained by SGC-GL (a) and SG-GL (b) synthesis routes.

The final weight loss in the temperature range from 170 to 350 °C is ascribed to the burn-out of residual organics. No weight loss was observed beyond 350 °C, which indicates complete decomposition of the gel giving a product free of residual reactants and carbonaceous matter. The thermal degradation of Gd-Ce-O gel synthesized by SG-GL process is depicted in Fig. 24b. Analogically as in the case of sol-gel synthesis using EG (see Fig. 23), the decomposition process in the GDC acetate-glycerate system consists of two main weight loss domains. The first domain (~23%) corresponds to the endothermic peak at ~180 °C in the DSC curve and it is ascribed to the removal of moisture and free glycerol. The second weight loss of about 25% accompanied by the strong exothermic peak with its maximum at ~290 °C might

be attributed to the degradation of acetates and glycerates. Negligible weight loss about 1.5% is observed in the temperature range from 350 to 550 °C, at higher temperature the weight of residual GDC precursor remains constant. The TG-DSC curves of Gd-Ce-O precursor gels derived from SGC-TA and SG-TA syntheses are shown in Fig. 25.

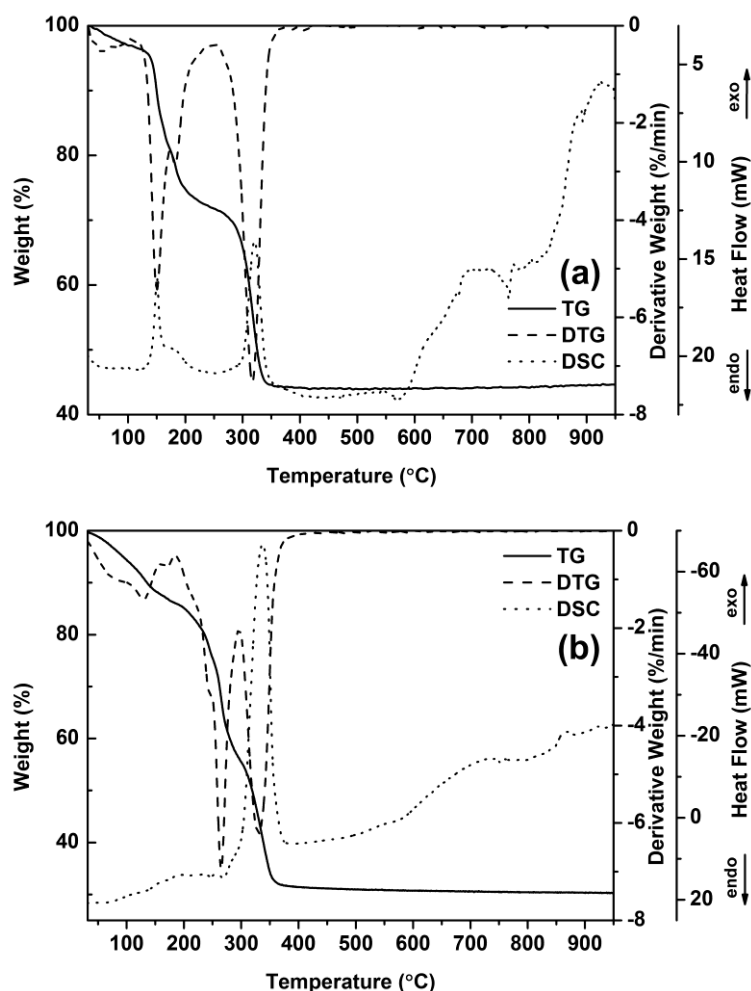


Fig. 25. TG-DSC curves of Gd-Ce-O precursor gels obtained by SGC-TA (a) and SG-TA (b) synthesis routes.

The thermal degradation of the gel obtained by SGC-TA route passes through three stages. During the initial stage from room temperature up to 120 °C residual water is removed. The second stage of exothermal decomposition is observed at ~150 °C and might be ascribed to the decomposition of nitrates and a part of tartrates. The residual tartrates decompose during the exothermic reaction at ~320 °C and this is in a good agreement with previously published

results [145]. No more weight losses are observed above 350 °C indicating that all organic residues are completely decomposed at this point. The TG curve of the Gd-Ce-O precursor gel synthesized by SG-TA process reveals that the weight loss in the GDC acetate-tartrate system occurs also in three steps. The first weight loss of about 14% is ascribed to the removal of adsorbed and hydrated water. The second weight loss (~30%) between 190 and 290 °C peaked at around 260 °C might be attributed to the decomposition of ammonium tartrate and ammonium acetate network. The final weight loss (~25%) accompanied by the strong exothermic peak with maximum at 340 °C could be assigned to the pyrolysis of coordination compounds and organic part of the gels. The constant weight of residual GDC precursor is observed at about 400 °C temperature, which is slightly higher comparing to SGC synthesis (see Fig. 25a).

Powder X-ray diffraction analysis

The phase crystallinity and purity of all samples were characterized by means of XRD analysis. The powder XRD patterns of GDC samples obtained by SGC-EG and SG-EG processes at different temperatures are given in Fig. 26.

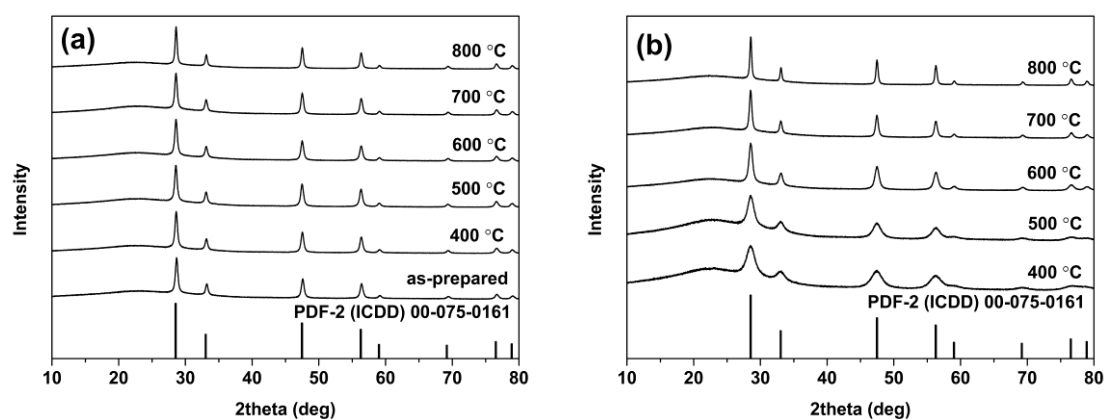


Fig. 26. XRD patterns of GDC prepared by SGC-EG (a) and SG-EG (b) synthesis routes at different temperatures.

It is obvious from Fig. 26a, that crystallization of GDC takes place already during the combustion process. All the diffraction peaks match very well the standard XRD data of $Gd_{0.1}Ce_{0.9}O_{1.95}$ (ICDD 00-075-0161). Fig. 26b shows the

XRD patterns of GDC powders prepared by SG-EG synthesis route. The crystalline phase has formed after annealing sample at 400 °C. Evidently, the degree of crystallinity increases with increasing annealing temperature. No X-ray reflections arising from by-products such as Gd_2O_3 or Ce_2O_3 are observed in both SGC-EG and SG-EG cases. The XRD patterns of GDC samples obtained by SGC-GL and SG-GL processes are shown in Fig. 27.

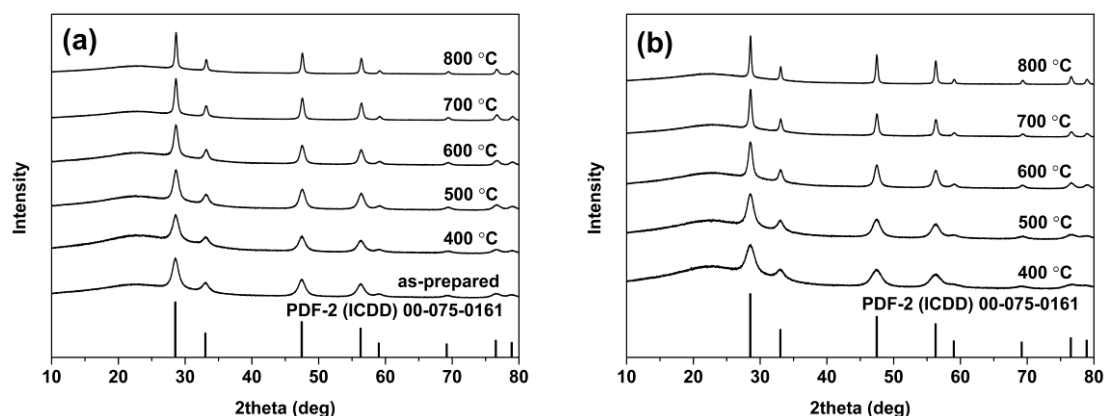


Fig. 27. XRD patterns of GDC prepared by SGC-GL (a) and SG-GL (b) synthesis routes and annealed at different temperatures.

Again, it is clearly seen that crystalline GDC phase is already formed after combustion process. The broad diffraction peaks indicate the nanocrystalline nature of synthesized powders. However, the peak broadening decreases with increasing annealing temperature. The XRD patterns of GDC powders prepared by SG-GL synthesis route are quite similar as for SGC-EG route (see Fig. 27). The broadening of reflection peaks decreases and the degree of crystallinity increases with higher temperature. Both synthesis routes resulted in single-phase cubic GDC with fluorite-type structure. The XRD patterns of GDC samples obtained by SGC-TA and SG-TA processes as a function of annealing temperature are depicted in Fig. 28a and b, respectively. Contrary to the SGC process with EG and GL (see Fig. 26a and Fig. 27a), the crystallization does not take place during the combustion with tartaric acid process. However, the desired crystalline phase is formed after thermal treatment at 400 °C for both SGC and SG routes. Raising the sintering temperature up to 800 °C resulted in

a much narrower peaks due to the particle growth. The absence of characteristic reflections corresponding to Gd_2O_3 phase suggests about intimate mixing of Ce(III) and Gd(III) cations in the precursor solution.

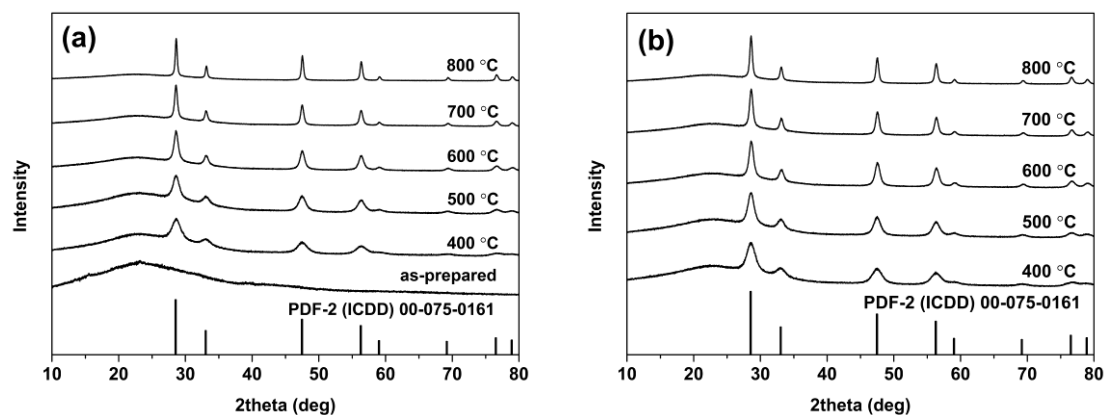


Fig. 28. XRD patterns of GDC prepared by SGC-TA (a) and SG-TA (b) synthesis routes and annealed at different temperatures.

As was mentioned in the experimental part, the size of crystallites was calculated from Scherrer equation. The estimated crystallite sizes of GDC powders calcined at different temperatures are presented in Table 5.

Table 5. Crystallite size and surface area of GDC powders.

Sample	Crystallite size (nm) at different calcination temperatures					S_{BET} after calcination at 800 °C, m^2/g
	400 °C	500 °C	600 °C	700 °C	800 °C	
SGC-EG	20.3	20.5	20.7	21.2	26.5	9.9
SG-EG	5.2	6.6	13.4	20.5	29.4	16.0
SGC-GL	7.2	7.9	10.7	17.0	24.3	19.0
SG-GL	5.2	6.1	11.9	19.9	29.6	12.9
SGC-TA	5.0	6.2	11.5	17.9	27.9	12.9
SG-TA	5.2	6.4	8.3	14.8	19.9	15.8

In general, a gradual growth in crystallite size with increasing heat treatment temperature is observed in all samples, except for SGC-EG derived powders, whose size is nearly constant in the temperature range from 400 to 700 °C.

The calculated crystallite sizes of the final powders annealed at 800 °C vary from 19.9 to 29.6 nm with the largest crystallites for SG-GL and the smallest for SG-TA route. It was found that there is no evident correlation between crystallite size and synthesis route adopted for the preparation of GDC powders with selected complexing agents/fuels.

BET analysis

The specific surface area values obtained for the GDC powders heated at 800 °C are summarized in Table 5. It can be seen that GDC powders synthesized via SGC-GL route showed the highest values (19.0 m²/g), while the lowest values (9.9 m²/g) were obtained for GDC prepared by SGC-EG synthesis route.

FTIR analysis

The FTIR spectra of the GDC specimens prepared by SGC-EG and SG EG methods as a function of sintering temperature are presented in Fig. 29.

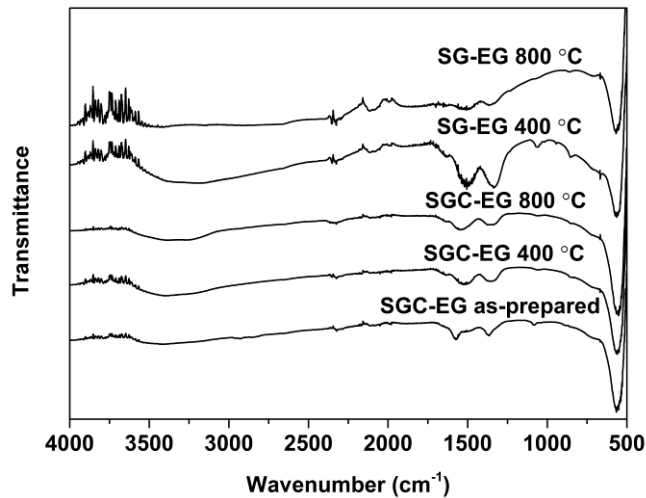


Fig. 29. FTIR spectra of GDC samples synthesized by SGC-EG and SG-EG routes as a function of temperature.

The FTIR spectra of as-prepared and annealed GDC samples synthesized by SGC-EG technique are quite similar with respect to the position and intensity of the main absorption bands. The most intense absorption band at 565 cm⁻¹ is assigned to the metal-oxygen (Ce-O and/or Gd-O) stretching vibrations. Bands in the 1550–1280 cm⁻¹ region are characteristic of the ionic carbonate (CO₃²⁻)

and could be assigned to the stretching mode, ν_3 , and to the bending modes, ν_4 or ν_3 , of the C-O bond [146, 147]. The identity of weak absorption band near 1069 cm^{-1} is not clear. The broad band in the $3800\text{--}3000\text{ cm}^{-1}$ region is attributed to O-H stretching vibrations of adsorbed water molecules. The FTIR spectrum of the GDC sample synthesized by SG method and calcined at $400\text{ }^\circ\text{C}$ contains several absorption bands with maxima close to 1500 cm^{-1} , 1335 cm^{-1} , 1060 cm^{-1} and 840 cm^{-1} which can also be attributed to the vibrations of carbonate group. However, these absorption bands almost disappear after thermal treatment at $800\text{ }^\circ\text{C}$. The FTIR spectra of the GDC specimens prepared by SGC-GL and SG-GL routes are depicted in Fig. 30.

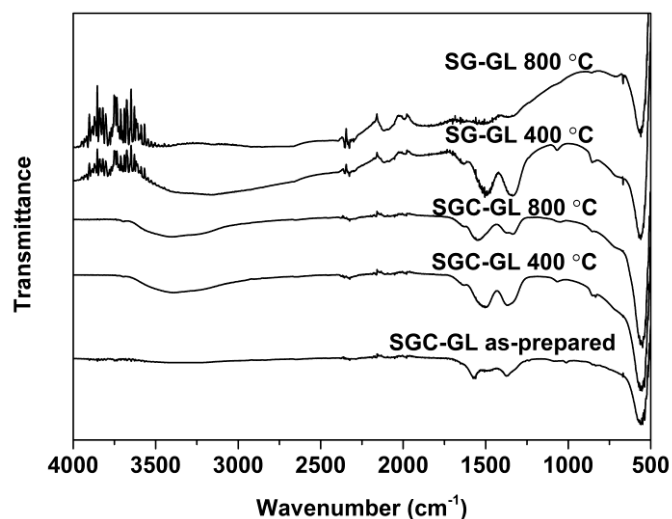


Fig. 30. FTIR spectra of GDC samples synthesized by SGC-GL and SG-GL routes as a function of temperature.

The FTIR spectra of SGC-GL derived powders are nearly identical to those obtained with the use of EG. The absence of characteristic absorption bands of aliphatic ($2800\text{--}3000\text{ cm}^{-1}$) and hydroxyl ($3000\text{--}3800\text{ cm}^{-1}$) groups is an evidence of complete burnout of glycerol after combustion process. The character of FTIR spectra of SGC-GL samples at elevated temperature remains practically unchanged. The absorption bands observed in the spectra of SG derived powders at about 850 , 1060 , 1330 and 1500 cm^{-1} disappear after calcination at $800\text{ }^\circ\text{C}$. Fig. 31 shows the FTIR spectra of the GDC powders prepared by SGC-TA and SG-TA methods.

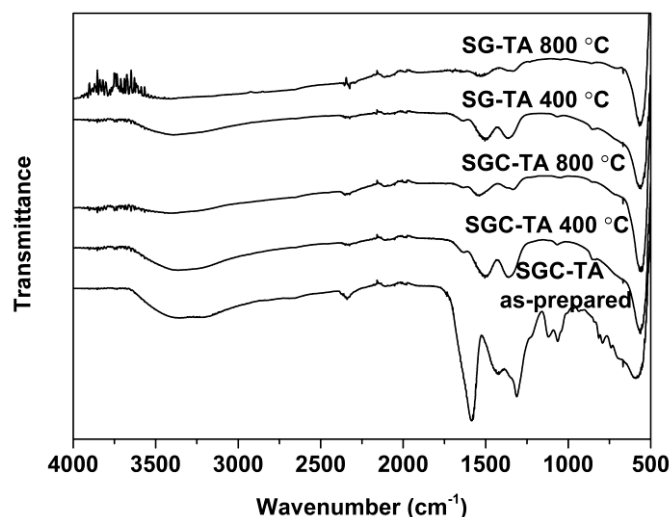


Fig. 31. FTIR spectra of GDC samples synthesized by SGC-TA and SG-TA routes as a function of temperature.

Due to the absence of intensive combustion and incomplete decomposition of organics using TA as a fuel, the FTIR spectrum of partially decomposed GDC gel (SGC-TA as-prepared) shows many absorption bands in 500–1750 cm^{-1} region, which are attributed to -COO-, -CO-OH, C-O, N-O vibrations [148]. With increasing the calcination temperature these bands almost disappear and only two weak signals are observed at ~ 1350 and ~ 1570 cm^{-1} like in previous cases (see Figs. 29 and 30). In the case of SG synthesis route situation is the same as for SG-EG and SG-GL. Considering the results of TG analysis (Fig. 23–25), it is clearly seen that for all six synthetic approaches the mass is constant at 800 °C. Therefore, it can be suggested that absorption bands in the region 1270–1600 cm^{-1} of FTIR spectra of final products calcined at 800 °C originate from the species adsorbed from ambient atmosphere.

Optical properties

Whereas synthesized products were of obviously different colors, diffuse reflectance spectroscopy was employed to obtain information about the optical properties. Fig. 32 illustrates the reflection spectra of powdered GDC samples synthesized at 800 °C. It is obvious that the nature of the reflection spectra strongly depends on the preparation technique. It can be seen that in the range

of wavelength from 800 to 600 nm, the reflectance of the samples synthesized by SGC route is stable and varies at about 95% followed by slight decreasing in the 600–450 region and drastic decrease in the shorter wavelengths region. Obviously different behavior is inherent to the reflection spectra of SG derived samples. All three spectra reveal constant reflectance in the 800–680 nm region with following significant decrease. The maximum difference in absorbance between SGC and SG derived samples is observed in the blue region.

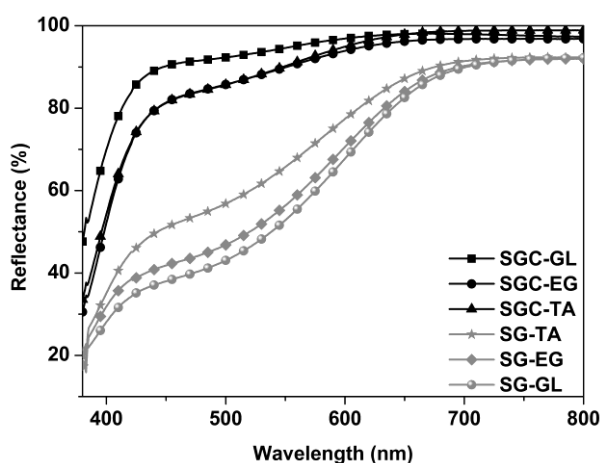


Fig. 32. Diffuse reflection spectra of GDC powders synthesized at 800 °C.

XPS analysis

XPS spectra of synthesized GDC samples were recorded in order to obtain the information on the oxidation state of cerium. The most commonly used Ce 3d electron core level XPS spectra for SGC-GL and SG-GL derived powders synthesized at 800 °C are shown as representative in Fig. 33.

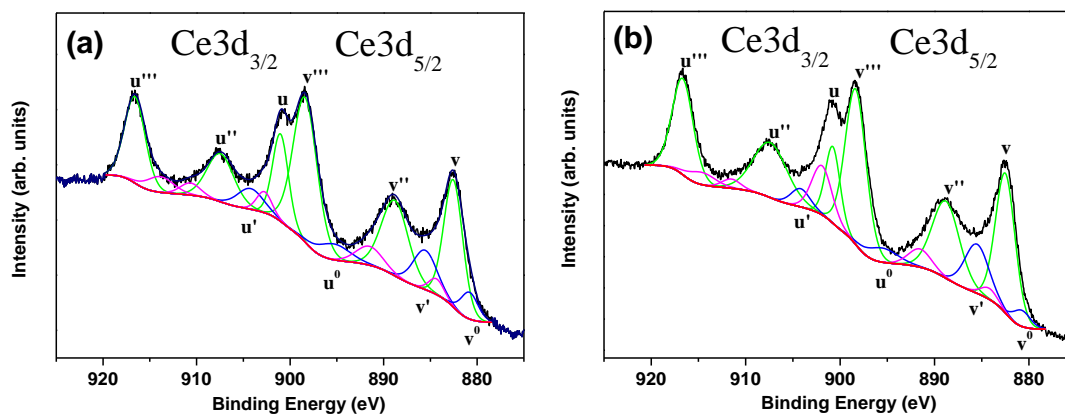


Fig. 33. Ce 3d XPS spectra of GDC powders prepared by SGC-GL (a) and SG-GL (b) routes.

Ce 3d XPS spectra for fully oxidized CeO₂ can be described by six peaks: v, v'' and v''' peaks refer to 3d_{5/2} and u, u'' and u''' peaks to 3d_{3/2} spin-orbit components [149]. This multiplet of peaks results from a final state “shake down” which places a different occupation in the O 2p and Ce 4f valence orbitals. The lowest binding energy states labelled u, v, u'' and v'' result from a mixture of Ce 3d⁹ O 2p⁵ Ce 4f² and Ce 3d⁹ O 2p⁴ Ce 4f¹ final states and the highest binding energy peaks labelled u''' and v''' result from a Ce 3d⁹ O 2p⁶ Ce 4f⁰ final state [150]. The peaks labelled u''' and v''' are unique to CeO₂, arising exclusively from Ce(IV) and were absent from the Ce 3d spectra of pure Ce(III) species. The spectrum for Ce(III) oxide contains only four peaks (u⁰, u', v⁰ and v') because it lacks the Ce 4f⁰ final state component. According to the literature [151, 152] the u''' peak can be used to describe quantitatively the chemical state of cerium. In the case of pure CeO₂, the u''' peak should constitute around 14% of total integral intensity of Ce 3d spectrum. For both XPS spectra (Fig. 33a, b) the u''' peak area was about 14% indicating the absolute majority of Ce(IV) oxidation state. Thus, three sharp doublets, labelled as v-u (at 882.5 and 901.0 eV, respectively), v''-u'' (888.8 and 907.4 eV) and v'''-u''' (898.3 and 916.5 eV), are attributed to Ce(IV), whereas two weak and hardly distinguishable doublets, v⁰-u⁰ (880.8 and 899.6 eV) and v'-u' (885.5 and 904.0 eV), could be due to the traces of Ce(III). The XPS measurements did not reveal significant differences in the surface chemistry for the GDC samples prepared by different approaches and annealed at 800 °C.

SEM analysis

The morphology of synthesized GDC powder samples was examined by SEM. The SEM micrographs of GDC powders prepared by SGC-EG route are shown in Fig. 34 (a, b, c). It can be seen that GDC powders consist of particles varying in size from approximately 1 to 5 μm. A closer look allows to see that these particles consist of significantly smaller sphere-like grains with the size around 20–40 nm (see Fig. 34c). The SEM images of GDC powders prepared by SG-EG route reveal slightly different morphological features, where different

size agglomerates covered by smaller particles are formed. These large particles are constituted of smaller grains with the similar size of about 20–40 nm as previous ones. On the whole, nanocrystalline nature of powders with the similar size and form of crystallites is observed for both SGC and SG techniques.

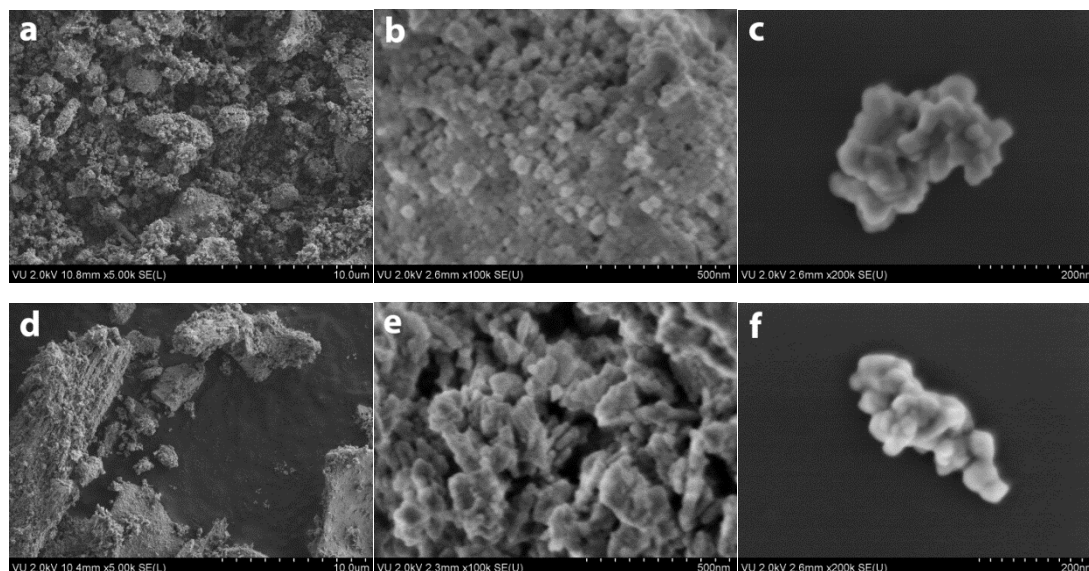


Fig. 34. SEM micrographs of GDC powders synthesized by SGC-EG (a, b, c) and SG-EG (d, e, f) routes and obtained at different magnification.

The SEM micrographs of GDC specimens synthesized by SGC-GL and SG-GL methods are shown in Fig. 35.

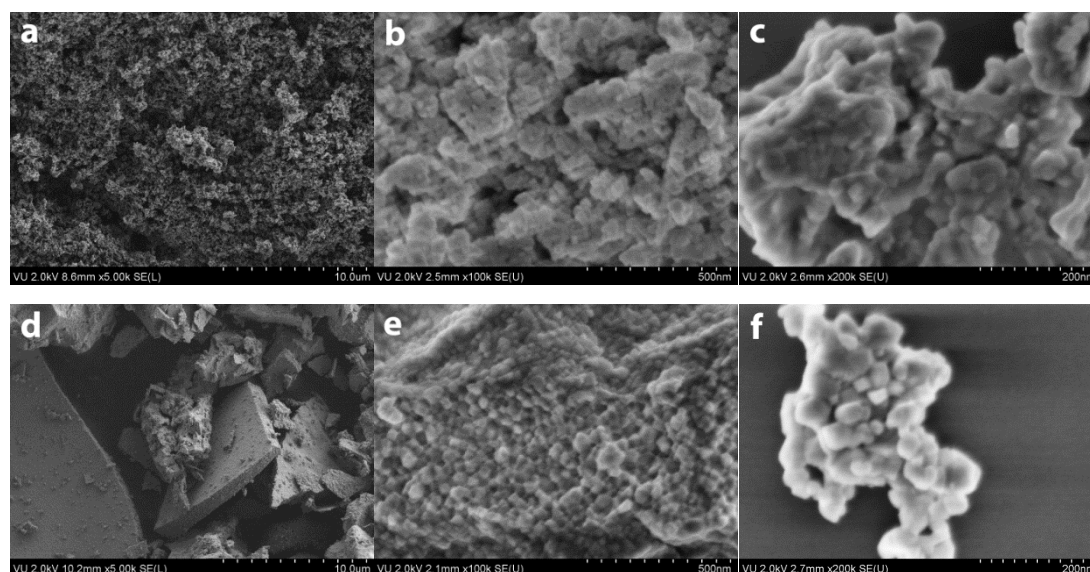


Fig. 35. SEM micrographs of GDC powders synthesized by SGC-GL (a, b, c) and SG-GL (d, e, f) and obtained at different magnification.

It can be seen from the SEM micrographs of GDC specimen synthesized by SGC-GL method (Fig. 35a, b, c) that uniform dendritic particles are formed. However, a closer look (Fig. 35c) revealed that these particles consist of smaller (~20–50 nm) differently shaped crystallites necked to each other. At the same time, GDC powders prepared by SG-GL method exhibit different morphological features (Fig. 35d, e, f). After calcination at 800 °C the various in size plate-like monoliths covered by smaller particles were obtained. The size of polyhedral form crystallites is slightly smaller comparing to SGC-GL method and lies in the range of approximately 20–40 nm. Fig. 36 represents SEM microstructural images of SGC-TA and SG-TA derived powders. The SEM micrographs of prepared powders using SGC-TA route (Fig. 36a, b, c) demonstrate the formation of agglomerates covered by smaller particles with spherical crystallites of approximately 20–40 nm. In the case of SG-TA synthesis the specimens having a porous structure and plate-like particles have formed (Fig. 36d, e, f). Coexistence of the two types of large (1–2 μm) and small (~50 nm) pores is evident. The size and shape of crystallites are similar to previously described. In summary, it could be noted that the size of the grains is similar for all synthesis approaches and belong to nanometer scale.

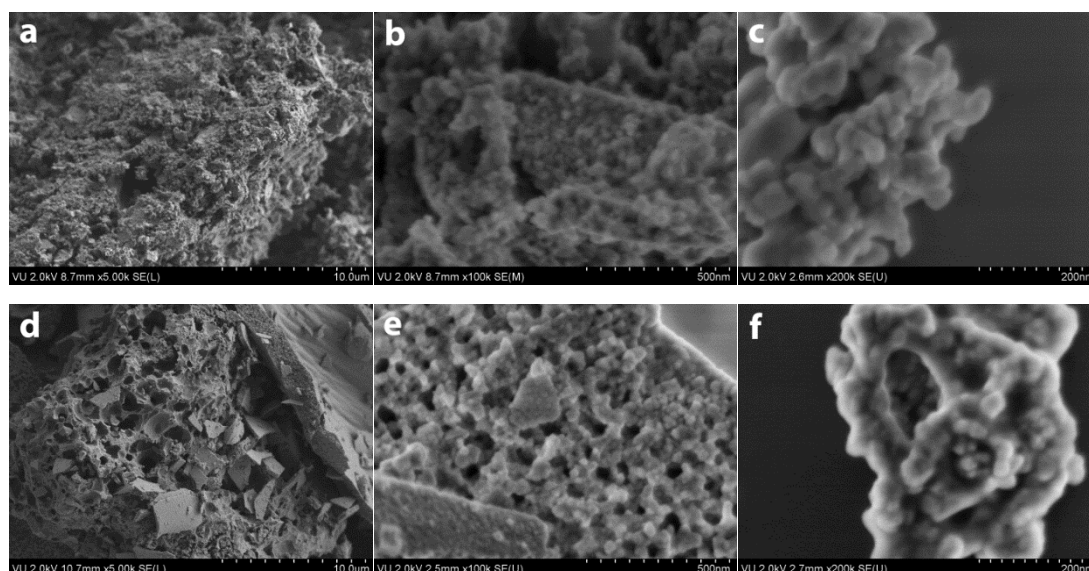


Fig. 36. SEM micrographs of GDC powders synthesized by SGC-TA (a, b, c) and SG-TA (d, e, f) routes and obtained at different magnification.

It is well known, that the densification, electrical properties and thermal expansion of GDC ceramics are very dependent physical properties [153]. Therefore, the morphological features of ceramic bodies sintered at 1300 °C for 2 h were also characterized by SEM analysis. Fig. 37 represents the SEM images of surface and cross-section of GDC pellets pressed from powders synthesized by SGC-EG and SG-EG routes. It can be seen that the pellet pressed from the powders prepared by SGC-EG method is composed of uniform and quite small grains (0.1–0.2 μm) without any interspaces and cracks (Fig. 37a), whereas the pellet prepared from SG-EG derived GDC powders are composed of relatively larger grains (0.2 to 0.5 μm) with a number of similar in size interspaces (Fig. 37c). However, the cross-sectional view (Fig. 37b, d) reveals the porous nature of the inner part of both pellets as a result of insufficient sinterability of samples. For SG-EG sample these empty spaces are especially large. The SEM images of GDC pellets prepared by SGC-GL and SG-GL routes are represented in Fig. 38.

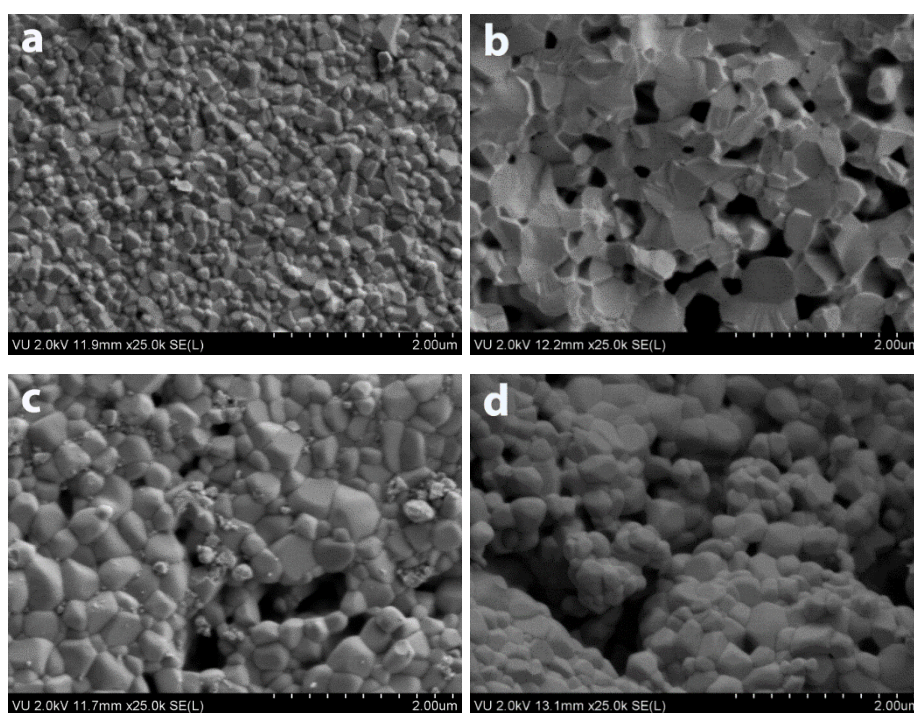


Fig. 37. Surface (a, c) and cross-section (b, d) of GDC pellets prepared from SGC-EG (a, b) and SG-EG (c, d) derived powders.

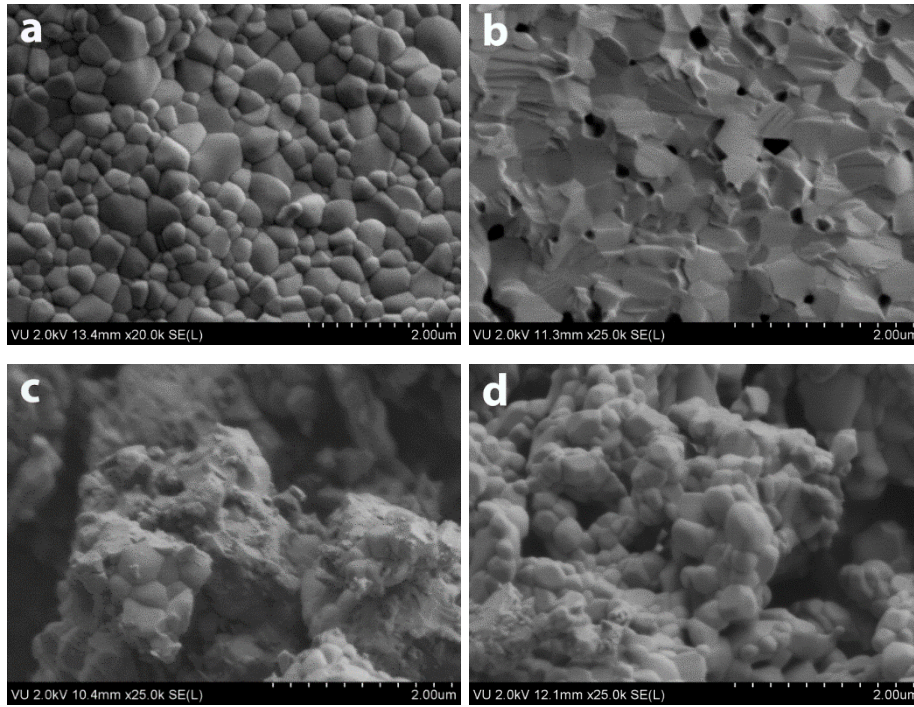


Fig. 38. Surface (a, c) and cross-section (b, d) of GDC pellets prepared from SGC-GL (a, b) and SG-GL (c, d) derived powders.

The surface of the pellet pressed from the powders prepared by SGC-GL is constituted of the grains with the size ranging from approximately 0.2 to 0.6 μm , no interspaces and cracks are observed (Fig. 38a). The image of the cross-section of SGC-GL sample (Fig. 38b) reveals that dense ceramics with low porosity was obtained. Absolutely different morphological features are observed for SG-GL sample (Fig. 38c, d). Poor sinterability under applied conditions and consequently poor quality of ceramics is obvious. Fig. 39 shows the SEM micrographs of GDC pellets pressed from SGC-TA and SG-TA derived powders. The surface of the pellet prepared by SGC-TA synthesis route consist of 0.1–0.6 μm grains without visible defects (Fig. 39a), whereas the surface of the pellet synthesized by SG-TA (Fig. 39c) consist of smaller, but more uniform grains (0.1–0.4 μm) with noticeable porosity. The cross-section of both samples (Fig.39b, d) exhibit porous nature, however, it should be noticed that SGC derived specimens showed evidently better sinterability.

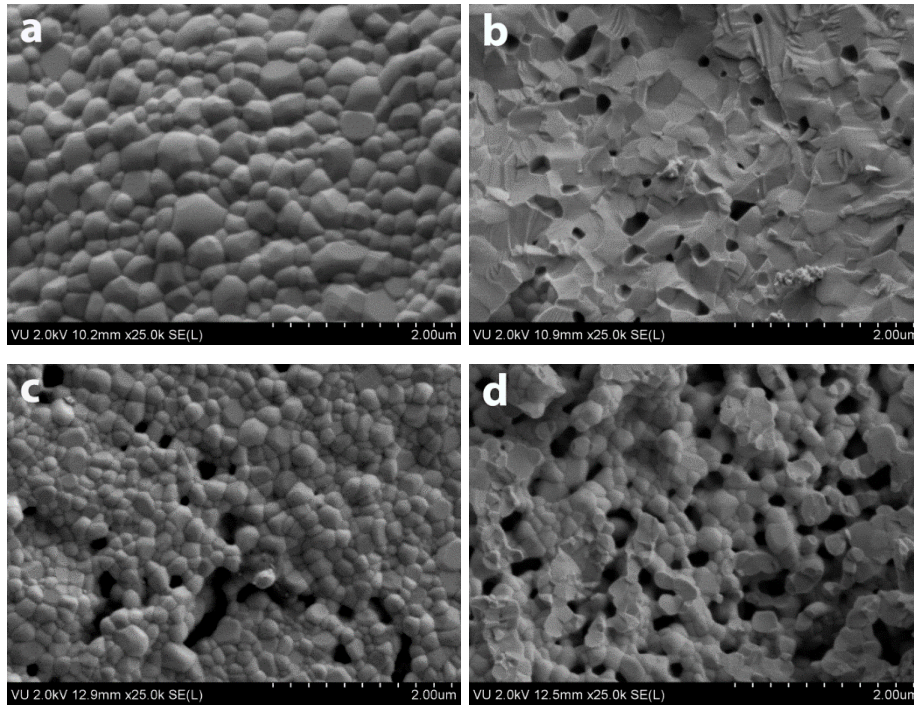


Fig. 39. Surface (a, c) and cross-section (b, d) of GDC pellets prepared from SGC-TA (a, b) and SG-TA (c, d) derived powders.

Electrical properties

A typical resistivity ($\tilde{\rho} = \rho' - i\rho''$) spectrum in complex plain of 10GDC measured by 4-electrode method is presented in Fig. 40a.

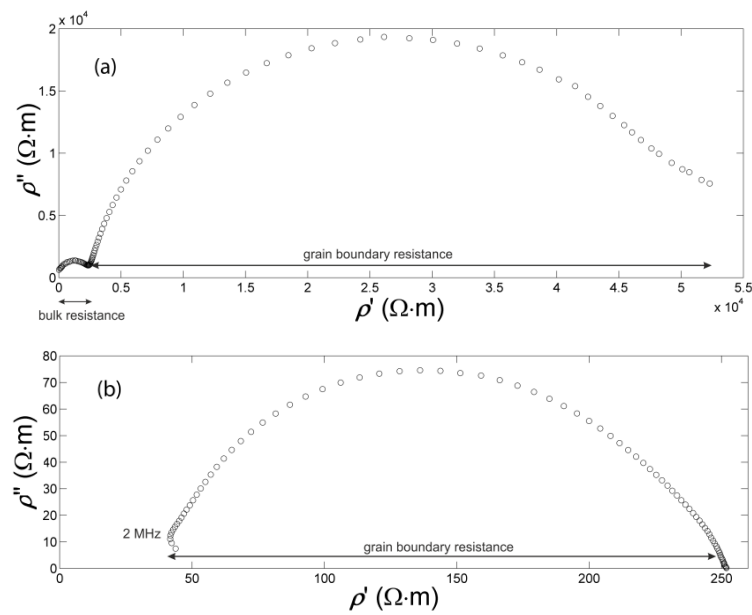


Fig. 40. Complex resistivity plots of SGC-GL sample, obtained by 4-electrode method (a) at 460 K and (b) 600 K.

Two semicircles can be observed. The one at higher frequencies on the left hand side is related to oxygen ion migration in the ceramics grains. Its diameter is equal to the resistivity of the ceramics bulk. The semicircle at lower frequencies is related to oxygen ion transport in grain boundaries and the resistivity of grain boundaries can be found from the diameter of the semicircle. At higher temperatures the bulk contribution disappears from the spectrum (Fig. 40b), so to find the bulk conductivity at temperatures up to 800 K the high frequency measurements are useful. An example of the resistivity complex plain plot measured at 800 K at high frequencies is presented in Fig. 41.

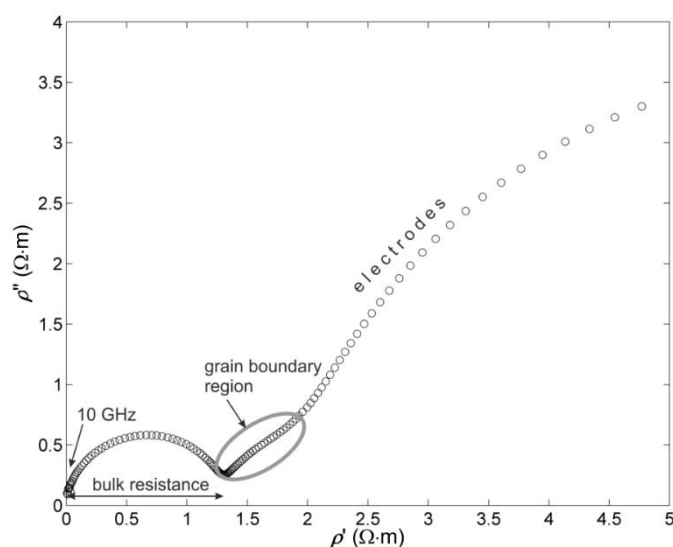


Fig. 41. Complex resistivity plot of SG-EG sample, obtained at 800 K by 2-electrode method.

However, at frequencies higher than 2 MHz only two-electrode method can be applied. By using this method there can be observed several contributions to the impedance spectrum, which are related to the processes at the interface of GDC and Pt electrode. A comparison of two measurements by 2- and 4-electrode method is shown in Fig. 42.

After analysis of all results the bulk and grain boundary resistivity values have been obtained. The bulk and grain boundary conductivities were calculated ($\sigma = 1/\rho$) and they are shown in Arrhenius representation in Fig. 43. As expected, all the conductivities obey Arrhenius law. It can be seen that SGC-GL

derived sample exhibits the highest bulk and grain boundary conductivity values at higher temperatures. The corresponding activation energies are presented in Table 6.

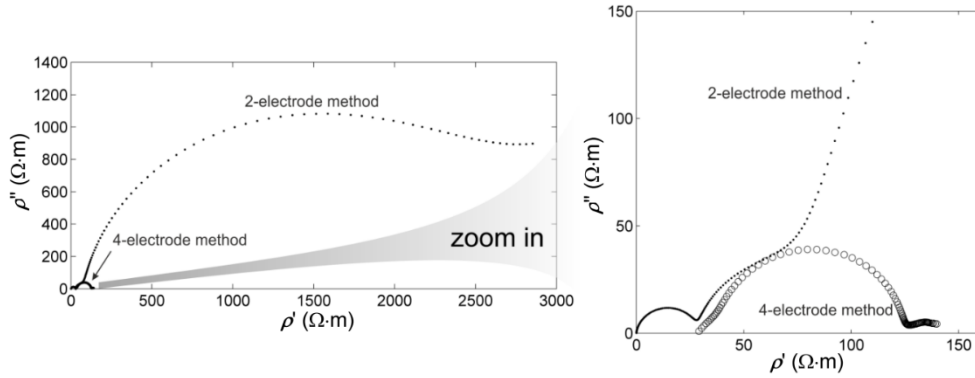


Fig. 42. Comparison of two impedance measurement methods for SG-TA sample (600 K).

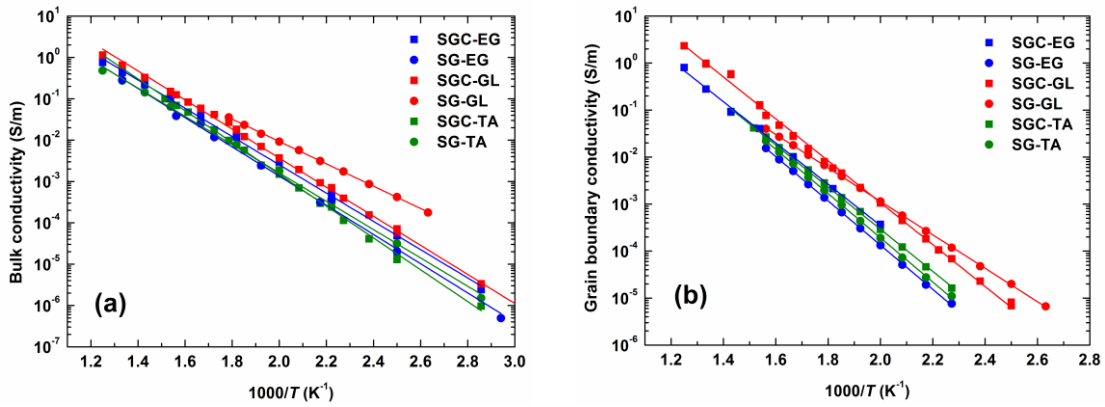


Fig. 43. Arrhenius plot of ceramics bulk (a) and grain boundary (b) conductivities.

Table 6. Conductivity activation energies of 10GDC ceramics.

10GDC sample	Bulk conductivity activation energy, eV	Grain boundary conductivity activation energy, eV
SGC-EG	0.68	0.88
SG-EG	0.71	0.94
SGC-GL	0.70	0.89
SG-GL	0.54	0.71
SGC-TA	0.77	0.90
SG-TA	0.68	0.94

At 5 GHz electrical frequency no dielectric dispersion of the real part of permittivity was observed at any temperature for all samples. So, dielectric permittivity of the obtained ceramics can be found at high frequencies and it is shown in Fig. 44.

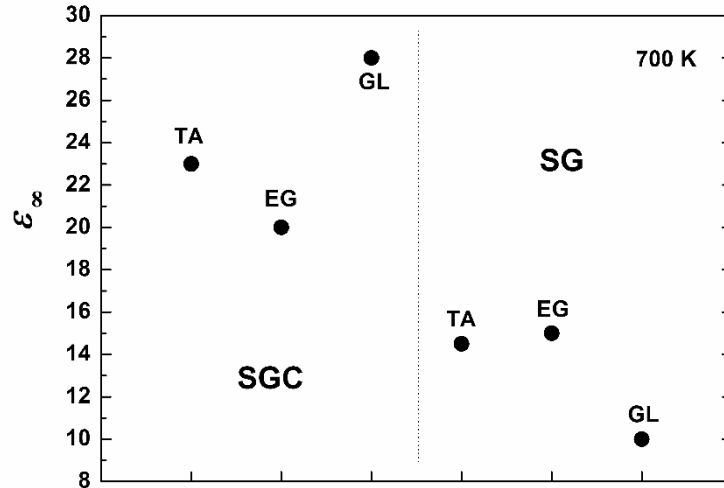


Fig. 44. High frequency limit of dielectric permittivity of 10GDC ceramics measured at 700 K.

Dielectric permittivity is related to the density of material, so it is a good way to evaluate porosity. In our case we have faced some difficulties to find ceramics density in the usual ways. The Archimedes method could not give the correct density values, because some ceramics showed open cracks or porosity. The density determination from sample's mass and dimensions also gives large errors because of not perfect geometry. As can be seen from Fig. 44, dielectric permittivity is higher for SGC derived ceramics and SGC-GL sample has best ϵ_{∞} value. One can see, that among all the investigated ceramics SGC-GL sample shows the highest bulk and grain boundary conductivity values at higher temperatures, the highest dielectric permittivity as well as the highest density according to SEM analysis, so this SGC-GL seems to be the most promising synthesis way for 10GDC [154, 155].

3.2.2. Deposition of thin films

Thermal analysis

The thermal decomposition behavior of dried GDC precursor solution corresponding to the final composition of $\text{Gd}_{0.1}\text{Ce}_{0.9}\text{O}_{1.95}$, was investigated by simultaneous TG-DSC measurements in order to display decomposition steps, which are used as a basis for choosing hot plate treatment of as deposited films (see Fig. 45).

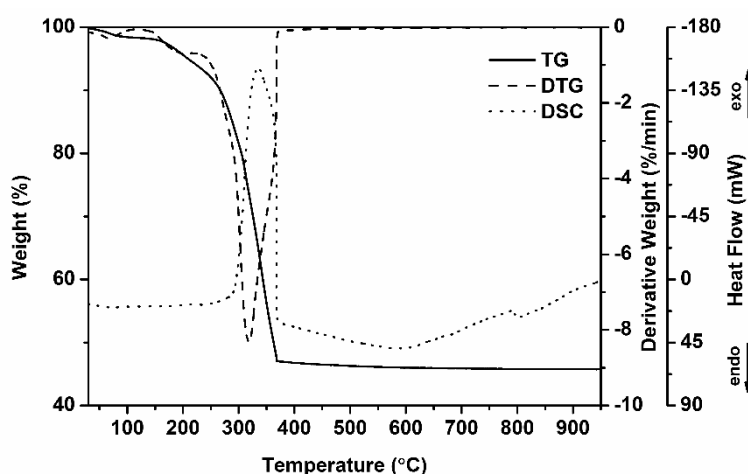


Fig. 45. TG-DSC curves of Gd–Ce–O precursor.

It is clearly seen from DTG curve that thermal decomposition occurs by one major step in temperature range 230–370 °C with the highest degradation rate at 320 °C. This drastic weight loss is accompanied by a broad exothermic signal peaked at 335 °C, which is attributed both to the decomposition of organics and formation of ceria fluorite type crystal structure. The constant weight of residual GDC precursor is observed above 370 °C, indicating that all organic residues are decomposed at this point. For that reason, 400 °C temperature was chosen for the heat treatment on a hot-plate after each deposition cycle. Intermediate heating and such a low decomposition temperature allows to eliminate an evolution of gases from the film during the final annealing and avoid a formation of defects, thus leading to the formation of good quality thin film.

X-ray diffraction analysis

The phase crystallinity and purity of all synthesized films were characterized by means of XRD analysis. Fig. 46. represents XRD patterns of 10GDC coatings processed at different annealing temperatures on Si and Si/YSZ substrates.

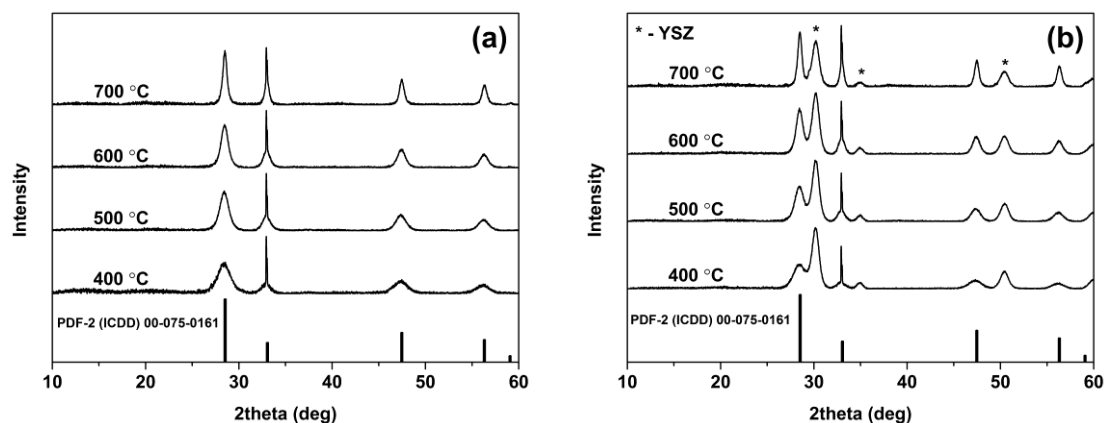


Fig. 46. XRD pattern of 10-layered 10GDC films on Si (a) and Si/YSZ (b) substrates annealed at different temperatures for 2 h.

It is evident that crystalline GDC phase is already formed after heat treatment at 400 °C. All the diffraction peaks match very well the standard XRD data of $Gd_{0.1}Ce_{0.9}O_{1.95}$ (ICDD 00-075-0161). No additional peak was observed. The reflection at ~33 degrees is overlapping with a sharp peak from Si substrate. The broad diffraction peaks indicate the nanocrystalline nature of films. The broadening of reflection peaks decreases and the degree of crystallinity increases with higher annealing temperature. The same behavior was observed for CeO_2 , 15GDC and 20GDC films. XRD patterns of ceria films with different chemical composition annealed at 700 °C are shown in Fig 47. It is seen that peak broadening increases with increasing of Gd content. The broadest and the sharpest peaks are attributed to 20GDC and pure CeO_2 , respectively.

The average crystallite size was calculated from Scherrer equation (see Eq. 13) at the peak position of the main reflection (111). The estimated crystallite sizes of ceria films annealed at different temperatures are summarized in Table 7.

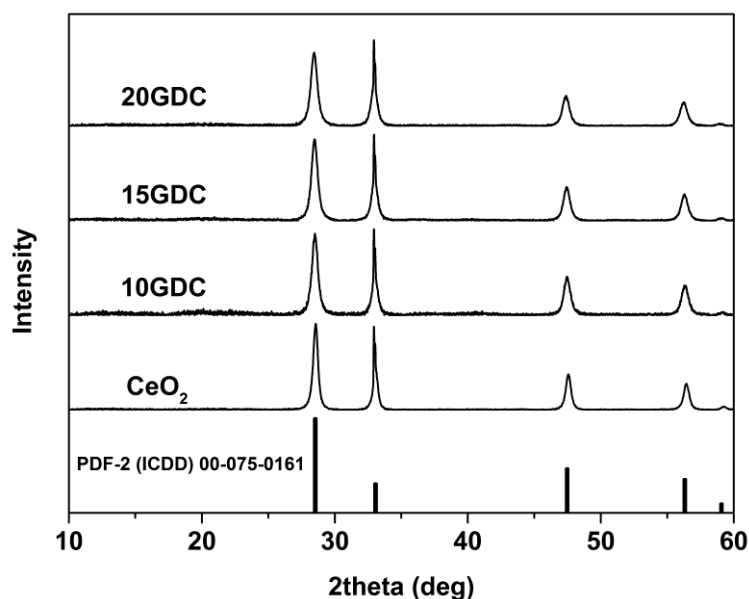


Fig. 47. XRD pattern of 10-layered ceria films on Si substrate annealed at 700 °C temperature for 2 h.

Table 7. Crystallite size of ceria films.

Sample	Crystallite size (nm) at different annealing temperatures			
	400 °C	500 °C	600 °C	700 °C
CeO ₂	6.1	7.9	10.1	21.1
10GDC	5.7	7.2	8.8	15.8
15GDC	5.2	6.9	8.6	15.1
20GDC	5.0	6.6	8.5	14.2

As it was expected, the crystallite size gradually increases with temperature increase. For all annealing temperatures the largest crystallites were calculated for un-doped ceria and the smallest for 20GDC.

Raman spectroscopy

Raman spectroscopy measurements were performed in order to study annealing temperature and doping-induced effects in all synthesized samples. Raman spectra of ceria films on Si substrates annealed at various temperatures are represented in Fig. 48. The peak positions were determined by fitting the data to a Lorentzian line shape.

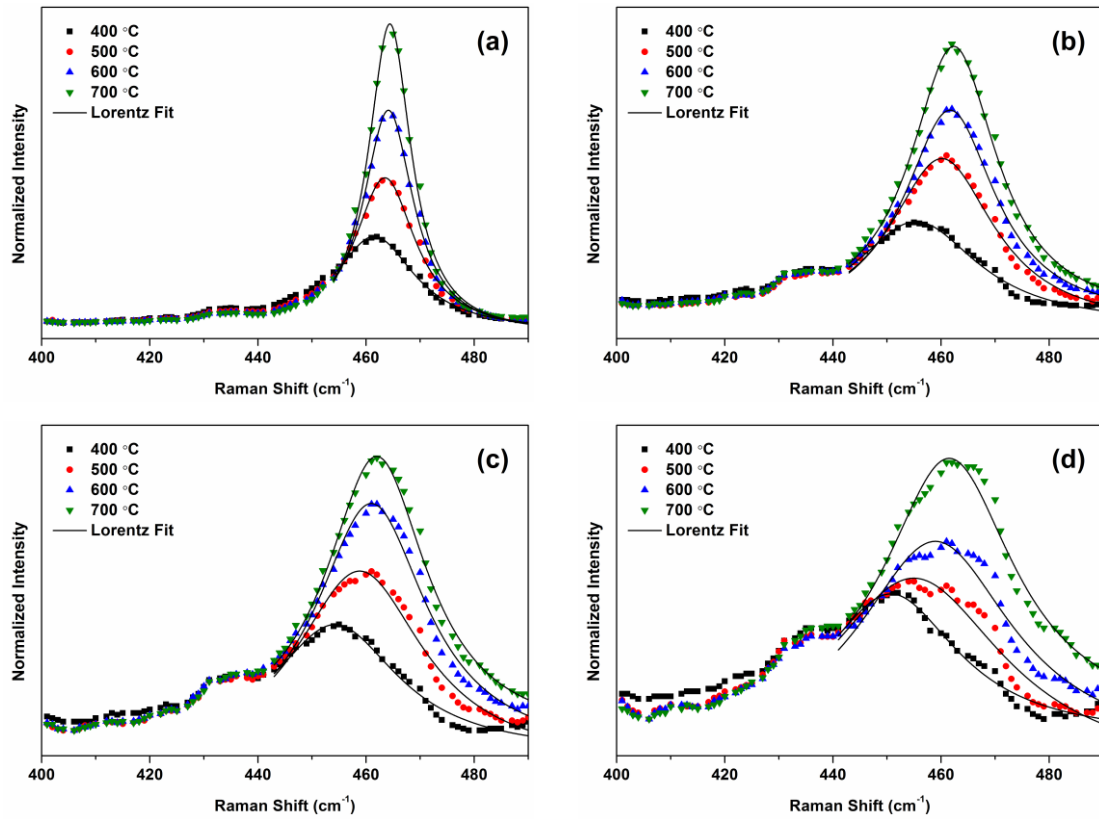


Fig. 48. Raman spectra of 10-layered CeO₂ (a), 10GDC (b), 15GDC (c), and 20GDC (d) films on Si substrate annealed at different temperatures for 2 h.

The results show that the major band is located at approximately 460 cm⁻¹. This peak is associated with a symmetric breathing mode of the oxygen atoms around Ce atom and corresponds to the F_{2g} symmetry, which confirms the formation of cubic CeO₂ phase [156, 157]. Two evident trends related to annealing temperature and chemical composition can be observed in Raman spectra. The influence of annealing temperature and consequently of a grain size on Raman line broadening, intensity and Raman shift can be noticed. Raman line broadening is observed as the grain size gets smaller. This behavior is attributed to combined effects of phonon confinement due to nanosize effect and lattice strain associated with defect species [158, 159]. Independently on the chemical composition of ceria films the Raman peak was shifted towards higher energies with increasing of annealing temperature. Similar behavior of Raman spectra of ceria was reported by other authors [160, 161]. The second trend is related to the

chemical composition of films. Symmetrical stretching mode of the Ce–O₈ vibrational unit is very sensitive to any disorder in the oxygen sublattice [162], consequently it is sensitive to the substitution of Ce(IV) by Gd(III) and creation of oxygen vacancies. It can be seen that as the Gd concentration in ceria increases, the Raman spectrum changes considerably with increase in width and decrease in intensity. Moreover, the Raman peak was shifted towards lower energy with increasing of Gd content. The change in Raman line size and shape is attributed to the lattice expansion induced by the substitution of Ce(IV) by Gd(III) and presence of oxygen vacancies [158, 163]. The grain size also makes contribution, since it depends on the composition of samples (see Table 7). The same effect of chemical composition of doped ceria on Raman spectra was described by other authors [163-165]. The dependence of Raman shift on annealing temperature is illustrated in Fig 49.

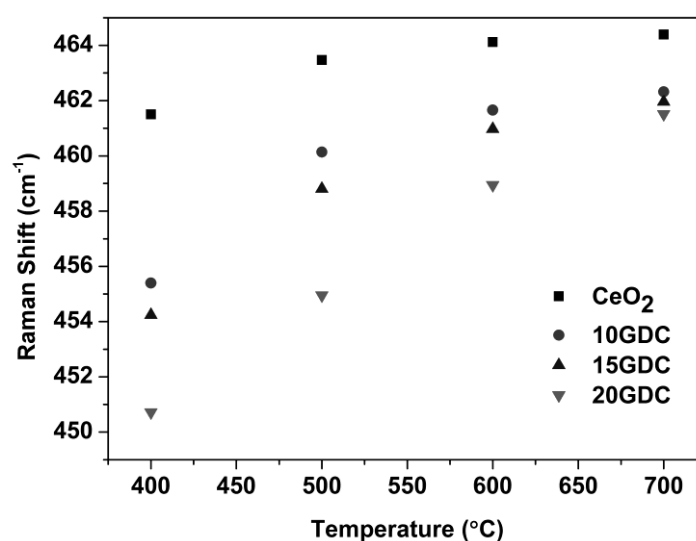


Fig. 49. Raman shift versus annealing temperature.

XPS analysis

XPS studies were performed in order to examine the oxidation state of cerium in films annealed at 400–700 °C temperatures. Ce 3d XPS spectra of 10GDC film annealed at 700 °C are illustrated in Fig. 50 as representative. Fig 50a represents the surface of the film, spectrum was recorded after introducing the sample into the XPS analysis chamber. Fig 50b represents the film in ~10 nm depth, spectrum was recorded after a short Ar⁺ sputtering.

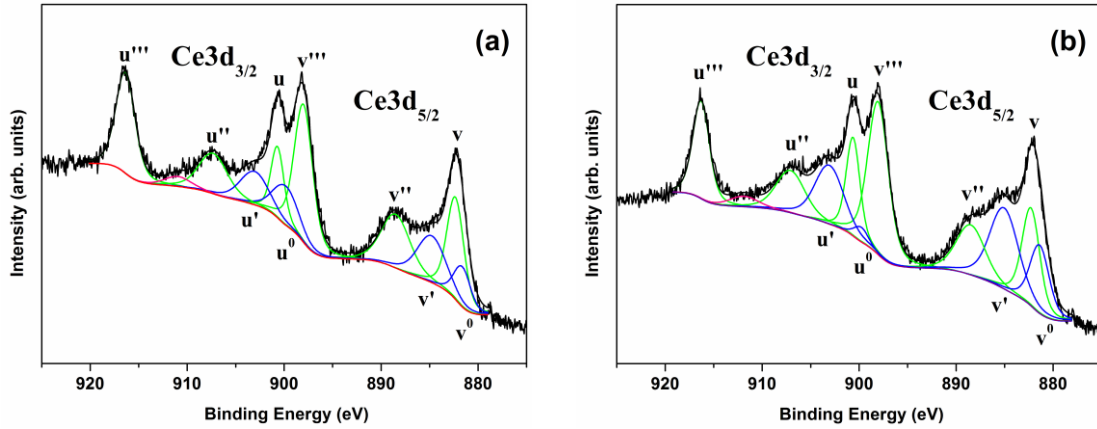


Fig. 50. Ce 3d XPS spectra of 10GDC film annealed at 700 °C temperature measured on the surface (a) and ~10 nm depth (b).

Analogously as in the case of bulk ceramics (see Fig. 33) there are two sets of spin-orbit multiplets: u and v corresponding to Ce 3d_{3/2} and Ce 3d_{5/2}, respectively. The intense peaks labeled u''' and v''' corresponding exclusively to Ce(IV) state are clearly seen in both spectra. However, it can be seen that apart from the Ce 3d doublets corresponding to Ce(IV) states (v, v'', v''', u, u'', u''') the XPS spectra also show a presence of additional peaks (v⁰, v', u⁰, u') which correspond to Ce(III) states indicating partial reduction of cerium. Contribution of the peaks corresponding to Ce(III) state into the total integral intensity of the spectrum increases after bombardment with Ar⁺ ions. Intensity increase at binding energies ~885.3 and ~903.3 eV, corresponding to v' and u' peaks, accordingly, is evident. Quantitative analysis of the Ce 3d photoemission spectra yields that the fractional percentage of cerium atoms in Ce(IV) state is approximately 90% and 65% before and after sputtering, respectively. Unfortunately, these results do not allow to make conclusions on a depth profiling of Ce(IV)/Ce(III) pair. Such considerable reduction of ceria is due to preferential removal of oxygen caused by Ar⁺ sputtering and such behavior is in a good agreement with previously published results [166-168]. The XPS measurements did not reveal any significant difference in oxidation state of Ce for the samples prepared at different temperatures.

SEM analysis

Plane view and cross-section of 10GDC films fabricated on Si substrate at 400 and 700 °C are shown in Fig. 51.

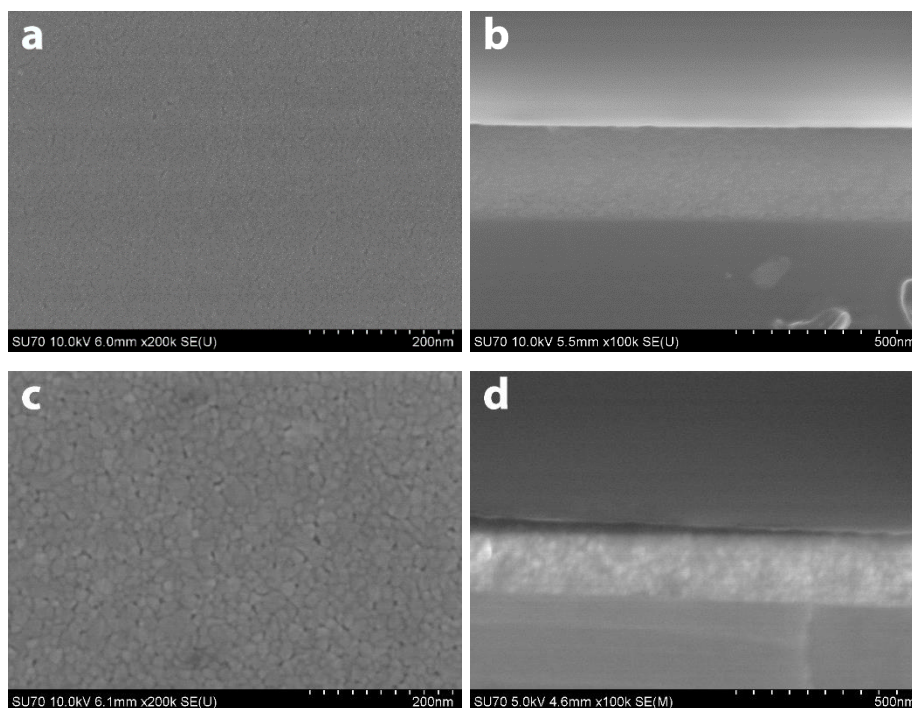


Fig. 51. Plane view (a, c) and cross-sectional (b, d) SEM images of 10-layered 10GDC film on Si substrate annealed at 400 °C (a, b) and 700 °C (c, d).

Surface of the film annealed at 400 °C consist of fine nanosized grains with some pores of insignificant size and without any substantial defects. Cross-section also does not reveal any apparent pores. Surface of the film annealed at 700 °C consist of obviously larger grains with broader distribution. Grain size varies from approximately 10 to 30 nm with an average at about 15 nm, which is in a good agreement with results obtained by XRD analysis. Cross-sectional view reveals completely dense morphology and does not show any sign of porosity. For both temperatures film surfaces were uniformly smooth and did not present any distinguishable defects. One of the reason of absence of defects is that organic part of precursor solution was decomposed during the heat treatment on a hot-plate. This step allows to avoid decomposition of organics within a film during the final annealing. Plane view of CeO₂, 10GDC, 15GDC and 20GDC films on Si substrate are depicted in Fig. 52 for comparison.

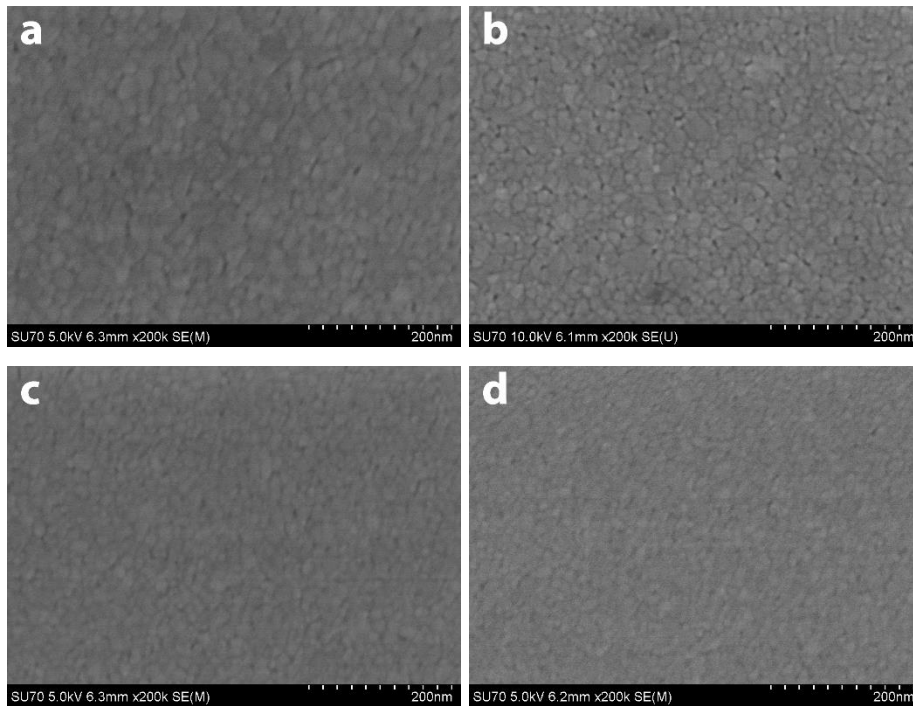


Fig. 52. Plane view SEM images of CeO₂ (a), 10GDC (b), 15GDC (c), and 20GDC (d) films on Si substrate annealed at 700 °C for 2 h.

Influence of Gd content in ceria lattice can be observed. Pure ceria exhibit larger grain size than that of doped films at the same annealing temperature. Grain size gradually decreases with increase of Gd concentration. Independently on chemical compositions films were uniform, smooth, dense and free of cracks. It should be noted that 20GDC film possess the most uniform grain size distribution. Fig. 53 shows SEM images of the surface and the cross-section of 10GDC film deposited on Si/YSZ substrate and annealed at 700 °C.

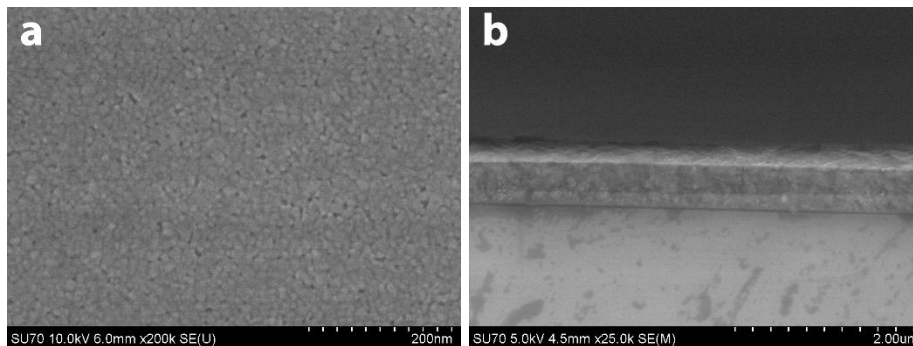


Fig. 53. Plane view (a) and cross-sectional (b) SEM images of 10GDC film on Si/YSZ substrate annealed at 700 °C.

The film exhibits the same morphological features as films deposited on Si substrates. Good adhesion between GDC and YSZ layers was observed. Thickness of the films was measured by cross-sectional SEM images. Dependence of the film thickness on the number of layers is showed in Fig. 54. A linear relation between the thickness and number of deposited layers was observed. The single-layer thickness was determined to be approximately 20 nm.

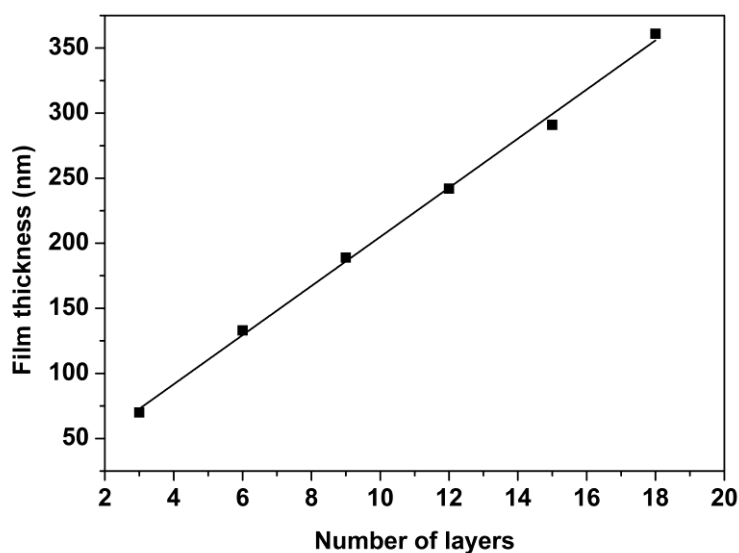


Fig. 54. Dependence of film thickness on the number of layers.

AFM analysis

AFM images of 10-layered CeO₂, 10GDC, 15GDC and 20GDC films on Si substrates after annealing at 700 °C are illustrated in Fig. 55. The images show fairly smooth surface and confirm that it is composed of nanoscale grains with gradually decreasing grain size with increase of Gd content. The roughness of surface was estimated by the calculation of RMS. The RMS roughness of deposited films was found to be 1.2, 0.9, 0.8 and 0.5 nm for CeO₂, 10GDC, 15GDC and 20GDC films, respectively.

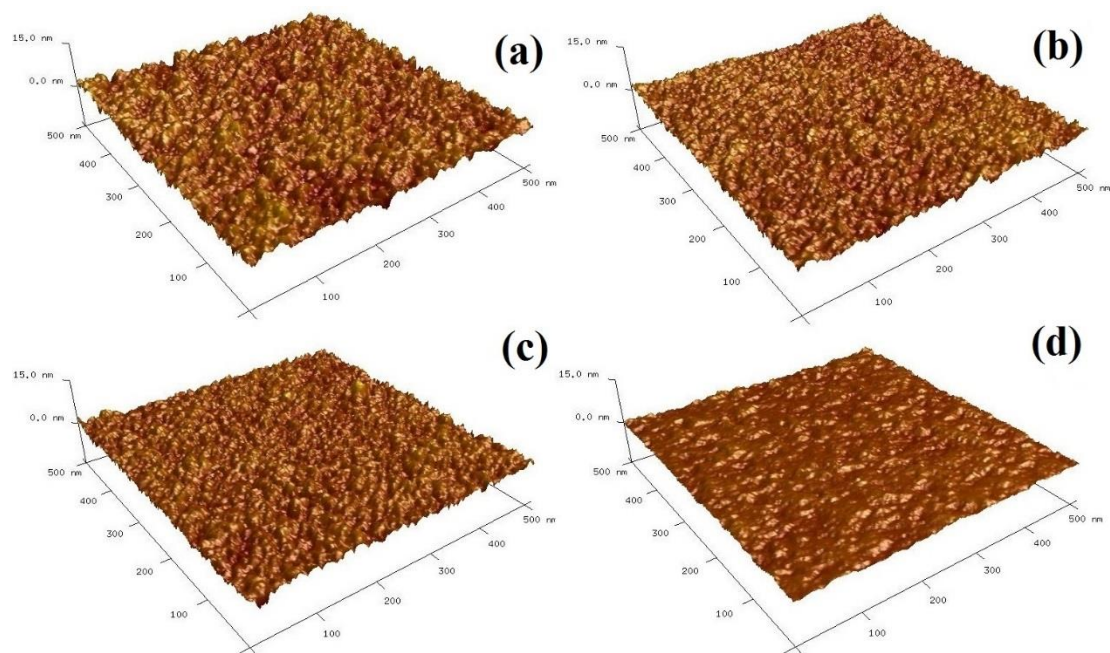


Fig. 55. 3D AFM images of CeO₂ (a), 10GDC (b), 15GDC (c), and 20GDC (d) films on Si substrate annealed at 700 °C for 2 h.

Optical properties

To reveal the correlation between the band gap energies and the grain size and morphology of the samples, diffuse reflectance spectroscopy was utilized. Reflection spectra of 10GDC films recorded in 250–800 nm spectral range are plotted in Fig. 56. All spectra exhibit the same behavior and consist of 3 absorption bands. First broad absorption band is observed in the spectral range ~500–800 nm with a maximum varying from 625 to 688 nm depending on the sample. Absorption band in this region visibly shifts to the shorter wavelength with increasing annealing temperature. The second narrower absorption band is located in blue-violet region. This band as well as previous demonstrates blue shift with increasing annealing temperature. Absorption maximum gradually shifts from 445 to 405 nm. The third absorption band is observed in ultraviolet region. A blue-shifting absorption threshold edge can be observed with annealing temperature increase. Generally, the absorption of cerium oxide in the UV region originates from the charge-transfer transition between the O 2p and Ce 4f states in O²⁻ and Ce⁴⁺. This absorption is much stronger than 4f¹–5d¹ transition from the Ce³⁺ species in the mixed valence ceria system [122].

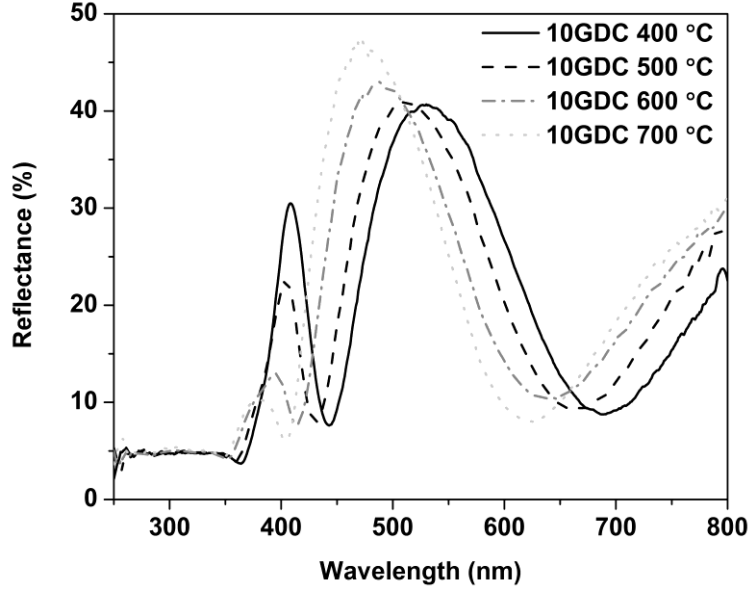


Fig. 56. Reflection spectra of 10-layered 10GDC films on Si substrate annealed at different temperatures.

According to the data of reflection spectra the optical band gap (E_g) of synthesized ceria films can be calculated by the following equation:

$$h\nu\alpha = C(h\nu - E_g)^n \quad (\text{Eq. 15})$$

Here $h\nu$ is the photon energy, α is the absorption coefficient, C is the proportional constant. The value of the exponent n denotes the nature of the sample transition: for direct allowed transition $n = \frac{1}{2}$ and for indirect allowed transition $n = 2$. The acquired reflectance spectra are converted to Kubelka-Munk function, the vertical axis is converted to quantity $F(R_\infty)$, which is proportional to the absorption coefficient. Thereby, α in the Tauc equation is substituted with $F(R_\infty)$ [169]. Thus, in the actual experiment, the relational expression becomes:

$$h\nu F(R_\infty)^{1/n} = C(h\nu - E_g) \quad (\text{Eq. 16})$$

Tauc plots for 10GDC films on Si substrates for direct and indirect allowed transitions are represented in Fig. 57. Band gap values were calculated using a linear fit for the straight interval in the region of largest exponential growth, the intercept with the energy axis corresponds to the optical band gap.

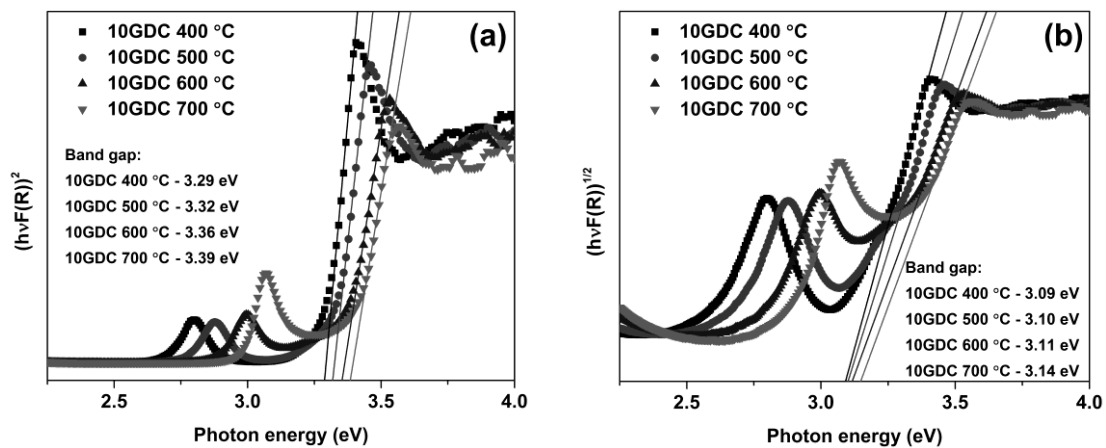


Fig. 57. Plots of $(hvF(R_{\infty}))^2$ (a) and $(hvF(R_{\infty}))^{1/2}$ (b) versus photon energy for 10-layered 10GDC films annealed at different temperatures.

It was found that behavior of the band gap energies for both direct and indirect allowed transitions is correlated with the microstructure of the films. In contradiction to the quantum confinement model predictions, the band gap values were found to increase as grain size increases. The same effect in pure and Gd doped ceria films with a grain size less than 50 nm was previously reported by Suzuki *et al.* [170]. Direct (indirect) band gap values were determined as 3.29 (3.09), 3.32 (3.10), 3.36 (3.11) and 3.39 (3.14) eV for 10GDC films annealed at 400, 500, 600 and 700 °C, respectively. These values are in a good agreement with previously published results [171-174]. Optical properties of nanocrystalline films showed systematic changes, which suggest that their optical behavior can be controlled by microstructure. There was no difference observed in the band gap values for doping level of 10–20 mol%, however, pure ceria films showed 0.05 eV lower band gap value. Similar trend in ceria thin films was observed by Ruiz-Trejo [175].

3.2.3. Development of analytical techniques

Spectrophotometric determination of Ce is based on the absorption of radiation by yellow Ce(IV) solution. Fig. 58 shows absorption spectra of Ce(IV) and Gd(III) solutions in the spectral range from 300 to 500 nm. It can be seen

that maximum absorption of Ce(IV) solution is observed at ~315 nm, however Gd(III) solution also absorbs in this region. Due to this reason 340 nm wavelength, where Gd(III) solution does not interfere, was chosen for further measurements.

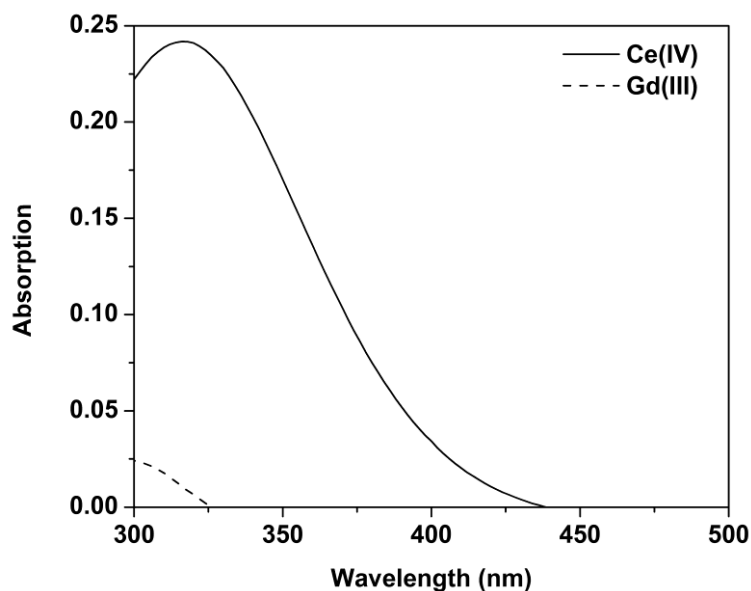


Fig. 58. Absorption spectra of Ce(IV) (10 $\mu\text{g/mL}$) and Gd(III) (10 $\mu\text{g/mL}$) solutions.

No effect on the stability of absorption due to the reduction of yellow Ce(IV) to colorless Ce(III) was observed at least for 2 h. The adherence to Beer's law was studied by measuring the absorbance values of solutions of varying cerium concentrations. The calibration graph was found to be linear in the concentration range from 1 to 30 $\mu\text{g/mL}$. Pearson's correlation coefficient r was determined to be 0.9989. The precision of the determination of Ce(IV) was established from the results of five determinations on standard solutions containing known amount of Ce(IV). The RSD values in the range 0.8–3.9% for different concentrations of Ce(IV) indicates that the method is quite precise.

Determination of Gd(III) is based on the formation of colored complex with arsenazo III. Fig. 59 shows absorption spectra of Gd(III)-arsenazo III complex, Ce(III)-arsenazo III complex and pure arsenazo III solutions in the spectral range from 400 to 700 nm.

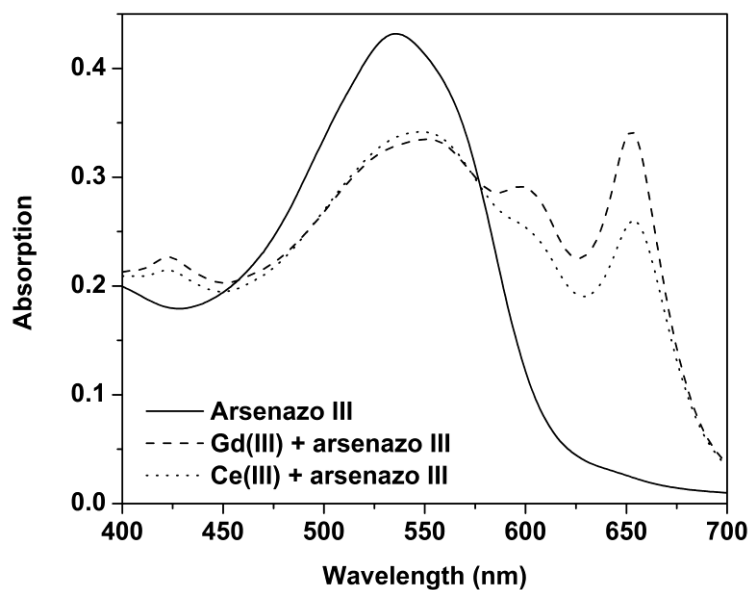


Fig. 59. Absorption spectra of arsenazo III (0.002%), Gd(III)-arsenazo III ($c_{\text{Gd}} = 1.0 \mu\text{g/mL}$) and Ce(III)-arsenazo III ($c_{\text{Ce}} = 1.0 \mu\text{g/mL}$) solutions.

The formation of Gd(III)-arsenazo III complex is evident by an appearance of absorption band with its maximum at $\sim 653 \text{ nm}$. Absorption of pure arsenazo III solution at this wavelength is negligible. This wavelength was selected for the further absorption measurements. However, Ce(III) ions also form complex with arsenazo III with an absorption in the same spectral region. To establish the optimum conditions for the determination of Gd, the effect of several experimental variables were studied and they are reported below.

Effect of pH on the formation of Gd(III)-arsenazo III complex was examined. Absorption of Gd(III) and arsenazo III mixtures was measured against water at various pH values ranging from 1.5 to 5.5 (Fig. 60.). It is clear that initially absorption values increase with increasing pH from 1.5 to 2.5. At higher pH values absorption is nearly constant, however absorption of pure arsenazo III increases. Hence, all absorption measurements on Gd(III)-arsenazo III complex were carried out at $\text{pH} \sim 3$. Optimal amount of arsenazo III was also investigated. For this purpose number of solutions (total vol. 50 mL) with constant concentration of Gd(III) and different amount of arsenazo III standard solution were prepared. Dependence of absorption on the volume of standard arsenazo III solution is given in Fig. 61.

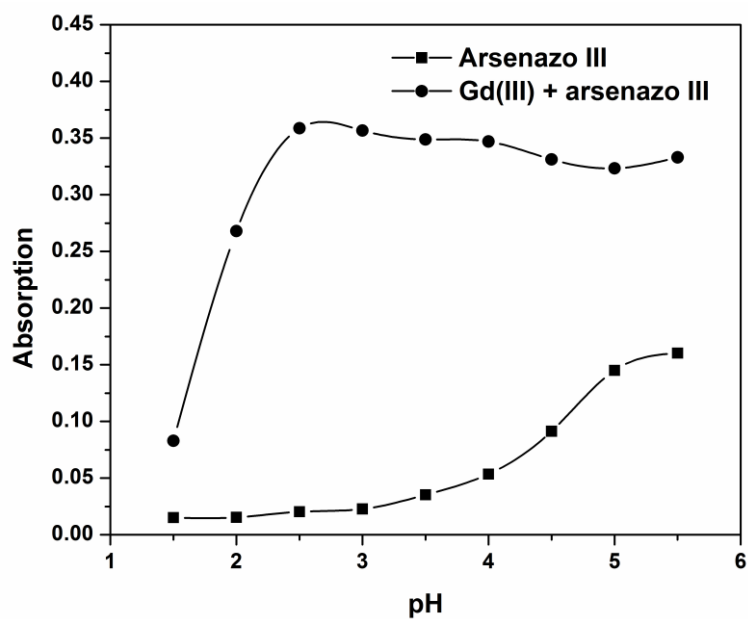


Fig. 60. Dependence of Gd(III)-arsenazo III complex absorption on pH, $\lambda = 653$ nm.

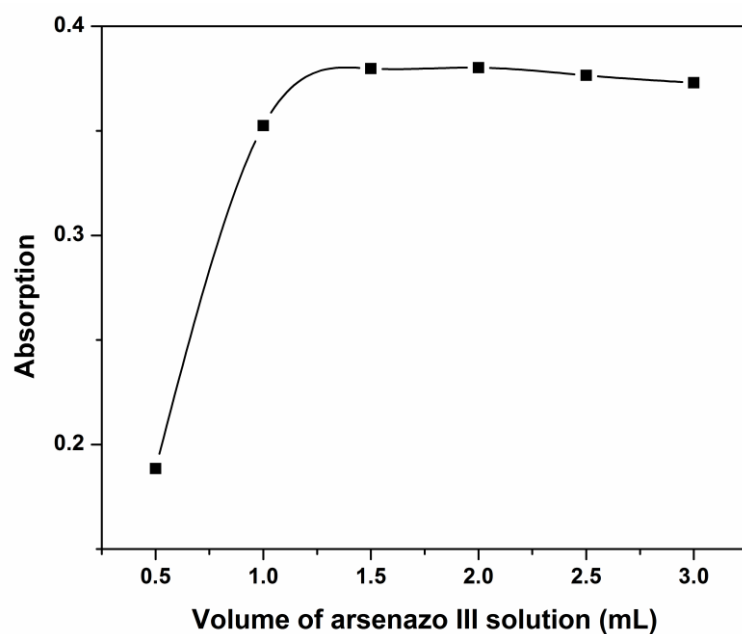


Fig. 61. Dependence of absorption of Gd(III)-arsenazo III complex on a volume of arsenazo III standard solution, $\lambda = 653$ nm.

It can be seen that absorption increases with increasing of arsenazo III volume from 0.5 to 1.5 mL. With higher amount of arsenazo III absorption is nearly constant. Hence, volume of 2 mL of standard arsenazo III solution was chosen

as optimal. Under the optimal conditions the absorption of a system was constant for a period of at least 2 h.

In order to obtain the calibration graph for Gd, a number of solutions containing certain amount of Gd(III) ions were prepared following the above described procedure and measured against corresponding reagent blank prepared in the same manner. Under optimal conditions the system obeys Beer's law in the concentration range from 0.1 to 1.5 $\mu\text{g/mL}$. Pearson's correlation coefficient r was determined to be 0.9996. The reproducibility of the measurements was studied by analyzing standard solutions containing known amount of Gd(III) ions. The RSD values in the range 0.2–0.7% for different concentrations of Gd(III) indicates that the method is very precise. The RSD values for Ce(III) and arsenazo III complex was 0.2–0.9%.

The proposed method was utilized for the determination of Ce and Gd content in synthesized GDC powders and thin films. Samples with nominal stoichiometry of $\text{Gd}_{0.1}\text{Ce}_{0.9}\text{O}_{1.95}$ (10GDC) and $\text{Gd}_{0.2}\text{Ce}_{0.8}\text{O}_{1.9}$ (20GDC) were analyzed. The results obtained for Ce and Gd in different samples are summarized in Table 8 as a molar ratio. The sum of Ce and Gd was assumed as 100%. All the samples were parallel analyzed by means of ICP-OES.

It was found that Gd content in analyzed samples ranged between 9.2 and 11 mol% for 10GDC and between 19 and 20.7 mol% for 20GDC. Determined Ce content varied in the ranges 89.0–90.8 mol% and 79.6–81 mol% for 10GDC and 20GDC, respectively. The data are in a good agreement with nominal stoichiometry of compounds and results obtained by ICP-OES. The RSD was found to be in the ranges 1.5–4.1% and 2.0–5.6% for Ce and Gd, respectively. The obtained results confirm that suggested spectrophotometric methodology can be successfully applied for the determination of Ce and Gd in GDC powders and films. Moreover, obtained results confirm homogeneity of synthesized samples and good agreement between desired and resulting composition of samples.

Table 8. Results of Ce and Gd determination in GDC samples (n = 5).

Sample	Spectrophotometric	ICP-OES
	Ce : Gd	Ce : Gd
10GDC SGC-EG	90.7 : 9.3	90.1 : 9.9
20GDC SGC-EG	79.8 : 20.2	80.2 : 19.8
10GDC SG-EG	89.1 : 10.9	89.9 : 10.1
20GDC SG-EG	80.3 : 20.7	79.8 : 20.2
10GDC SGC-GL	90.8 : 9.2	90.0 : 10.0
20GDC SGC-GL	81.0 : 19.0	80.1 : 19.9
10GDC SG-GL	89.0 : 11.0	89.8 : 10.2
20GDC SG-GL	79.8 : 20.2	80.0 : 20.0
10GDC SGC-TA	90.0 : 10.0	90.1 : 9.9
20GDC SGC-TA	80.5 : 19.5	80.2 : 19.8
10GDC SG-TA	90.6 : 9.4	90.0 : 10.0
20GDC SG-TA	80.1 : 19.9	80.2 : 19.8
10GDC film	89.4 : 10.6	89.5 : 10.5
15GDC film	85.2 : 14.8	85.2 : 14.8
20GDC film	79.6 : 20.4	79.8 : 20.2

4. CONCLUSIONS

1. The effect of the synthesis method on the main characteristics of YSZ ceramics has been widely studied in this work. YSZ ceramics containing 5, 8 and 10 mol% Y_2O_3 have been prepared employing three different chemical methods: co-precipitation, sol-gel and sol-gel combustion. The suitability of these methods was re-inspected.
2. It was determined that YSZ powders obtained by co-precipitation technique require higher annealing temperature (1500 °C) in order to obtain cubic phase structure, whereas 800 °C was sufficient temperature in the case of sol-gel and sol-gel combustion methods. It was demonstrated, that among three synthesis methods, YSZ ceramics prepared by sol-gel combustion method showed the highest ionic conductivity.
3. The sol-gel method have been successfully applied for the fabrication of uniform and smooth (RMS roughness 1.7 nm) YSZ thin films. A linear relation between the thickness of YSZ films and the number of deposited layers was observed. The single layer thickness was determined to be in the range of 50–60 nm.
4. A novel spectrophotometric analytical approach for the determination of Zr and Y in YSZ powders and films has been proposed. Quantitative determination was based on the complexation reactions of these metals with arsenazo III. The calibration graphs for Zr and Y were linear in the range of 0.08–0.4 $\mu\text{g/mL}$ and 0.1–0.6 $\mu\text{g/mL}$, respectively. The proposed procedure was successfully applied for the determination of chemical composition of synthesized and commercial YSZ samples. The RSD values for Zr and Y were in the range from 0.6 to 4.5% and from 0.6 to 3.6%, respectively.
5. In this study, nanostructural GDC powders (crystallite size ~20–40 nm) were successfully synthesized by sol-gel combustion and sol-gel processings using ethylene glycol, glycerol and tartaric acid as

complexing agents/fuels. The sinterability of pelletized powders at selected conditions was determined to be strongly dependent on the microstructure, which was influenced by the processing route.

6. Ce(IV) was determined to be the dominant oxidation state of Ce in all synthesized GDC samples. Moreover, the XPS measurements did not reveal significant differences in the surface chemistry for the GDC samples prepared by different approaches. The SGC-GL was found to be the most promising technique among the investigated synthesis approaches in terms of the highest ionic conductivity values, the highest dielectric permittivity as well as ceramic density.
7. Un-doped and Gd-doped ceria thin films have been synthesized by chemical solution deposition using spin-coating technique. Fabricated films were uniform, smooth, dense and free of cracks. RMS roughness was determined to be in the range 0.5–1.2 nm. A linear relation between the thickness of the GDC films and the number of deposited layers was also observed. The single layer thickness was determined to be about 20 nm. Moreover, it was determined that Gd reduces the grain size of films and slightly increases optical band gap.
8. A novel spectrophotometric analytical approach for the determination of Ce and Gd in GDC powders and films has been proposed. Determination of Ce was based on the absorbance of radiation by yellow Ce(IV) solution. Determination of Gd was based on complexation reactions of Gd(III) ions with arsenazo III. The calibration graphs for Ce and Gd were linear in the range of 1 to 30 $\mu\text{g/mL}$ and 0.1 to 1.5 $\mu\text{g/mL}$, respectively. The proposed procedure was successfully applied for the determination of Ce and Gd in synthesized GDC samples. The RSD values were found to be in the ranges 1.5–4.1 and 2.0–5.6% for Ce and Gd, respectively.

LIST OF PUBLICATIONS

Articles in Journals

1. A. Zarkov, A. Zalga, S. Tautkus, A. Kareiva, Novel analytical approach for the determination of zirconium and yttrium in YSZ powders, *Latvian Journal of Chemistry*, 51 (2012) 428-435
2. A. Zarkov, A. Stanulis, J. Sakaliuniene, S. Butkute, B. Abakeviciene, T. Salkus, S. Tautkus, A.F. Orliukas, S. Tamulevicius, A. Kareiva, On the synthesis of yttria-stabilized zirconia: a comparative study, *Journal of Sol-Gel Science and Technology*, 76 (2015) 309-319.
3. A. Zarkov, A. Stanulis, T. Salkus, A. Kezionis, V. Jasulaitiene, R. Ramanauskas, S. Tautkus, A. Kareiva, Synthesis of nanocrystalline gadolinium doped ceria via sol-gel combustion and sol-gel synthesis routes, *Ceramics International*, 42 (2016) 3972-3988.

Manuscripts in Journals

1. A. Zarkov, A. Stanulis, L. Mikoliunaite, A. Katelnikovas, V. Jasulaitiene, R. Ramanauskas, S. Tautkus, A. Kareiva, Chemical solution deposition of pure and Gd-doped ceria thin films: structural, morphological and optical properties, *Ceramics International* (submitted).

Published Contributions to Academic Conferences

1. A. Zalga, B. Abakeviciene, A. Zarkov, A. Beganskiene, A. Kareiva, S. Tamulevicius. Study on the properties of yttria-stabilized zirconia thin films prepared by sol-gel method. The 16th International Sol-Gel Conference, Hangzhou, China, August 28th-September 2nd, 2011, p. 168.
2. A. Zarkov, A. Zalga, S. Tautkus, A. Kareiva. Novel analytical approach for the determination of zirconium and yttrium in YSZ powders. 17th international scientific conference EcoBalt 2012, Riga, Latvia, 18-19 October 2012, p. 87.
3. A. Zarkov, S. Ceylan, S. Butkute. Synthesis and characterization of 10GDC/CeO₂ and 10GDC/Y₂O₃ compounds. International conference of young chemists Nanochemistry and Nanomaterials, Palanga, Lithuania, 7-9 December 2012, p. 54.

4. S. Tautkus, A. Zarkov, A. Beganskiene, V. Vickackaite, B. Abakeviciene, S. Tamulevicius. Synthesis and characterization of YSZ and GDC thin films using a novel sol-gel processing route. 3rd international conference Multifunctional, Hybrid and Nanomaterials, Sorrento, Italy, 3-7 March 2013, p. [B.1.2.1].
5. A. Kareiva, A. Zarkov, S. Butkute, A. Beganskiene, S. Tautkus, B. Abakeviciene, S. Tamulevicius. Sol-gel synthesis of composite materials for solid oxide fuel cell applications. 17th International Sol-Gel Conference, Madrid, Spain, 25-30 August 2013, p. 364.
6. A. Zarkov, S. Butkute, S. Ceylan, U. Morkan, S. Tautkus, A. Kareiva. Synthesis and characterization of Gd-doped and Gd/Y-codoped ceria. FEMS EUROMAT 2013: European Congress and Exhibition on Advanced Materials and Processes, Seville, Spain, 8-13 September 2013.
7. A. Zarkov, A. Zalga, S. Tautkus, A. Kareiva. UV-Vis spectroscopical investigations of the YSZ thin films on corundum, silicon and silica substrates. The 18th international scientific conference EcoBalt 2013, Vilnius, Lithuania, 25-27 October 2013, p. 102.
8. B. Abakeviciene, J. Sakaliuniene, A. Zarkov, A. Stanulis, S. Butkute, J. Pilipavicius, A. Beganskiene, A. Kareiva, T. Salkus, A. Kezionis, A. F. Orliukas, S. Tamulevicius. Deposition of synthesized YSZ and GDC thin films by electron beam evaporation technique. 13th European vacuum conference and 9th Iberian vacuum meeting and 7th European topical conference on hard coatings, Aveiro, Portugal, 8-12 September 2014. p. 194
9. A. Zarkov, A. Stanulis, A. Beganskiene, S. Tautkus, A. Kareiva. Synthesis of gadolinium doped ceria via sol-gel and sol-gel combustion synthesis routes. Chemistry and Chemical Technology 2015, Vilnius, Lithuania, 23 January 2015, p. 166-169
10. A. Zarkov, A. Stanulis, T. Salkus, S. Tautkus, A. Kareiva. Sol-gel combustion synthesis and characterization of nanocrystalline gadolinium

doped ceria. *Functional Materials and Nanotechnologies 2015*, Vilnius, Lithuania, 5-8 October 2015, p. 89

11. A. Zarkov, A. Stanulis, L. Mikoliunaite, A. Katelnikovas, S. Tautkus, A. Kareiva. *Chemical Solution Deposition of Ceria-Based Thin Films. Advanced Materials and Technologies*, Palanga, Lithuania, 27-31 August 2016, p.152

Published articles not included in the thesis

1. A. Zalga, B. Abakeviciene, A. Zarkov, A. Beganskiene, A. Kareiva, S. Tamulevicius, On the properties of yttria-stabilized zirconia thin films prepared by sol-gel method, *Materials Science-Medziagotyra*, 17 (2011) 191-196.
2. A. Zalga, A. Kareiva, A. Zarkov, S. Tautkus, B. Abakeviciene, UV-Vis spectroscopical investigations of the YSZ thin films on corundum, silicon and silica substrates, *Chemija*, 25 (2014) 29-33.
3. J. Trinkunaite-Felsen, H. Birkedal, A. Zarkov, S. Tautkus, Z. Stankeviciute, A. Kareiva, Environmentally benign fabrication of calcium hydroxyapatite using seashells collected in Baltic Sea countries: A comparative study, *Phosphorus, Sulfur, and Silicon and the Related Elements*, 191 (2016) 919-925.
4. S. Tautkus, A. Beganskienė, A. Žarkov, A. Merkevičius, A. Kareiva. Archeologinių dirbinių tyrimas atominės absorbcinės spektroskopijos (AAS), rentgeno spindulių difrakcinės analizės (XRD), infraraudonosios spektroskopijos (IR), termogravimetrinės analizės (TG) ir skenuojamosios elektroninės mikroskopijos (SEM) metodais. *Metodai Lietuvos archeologijoje*. VU leidykla, Vilnius 2013, pp. 137-181.

ACKNOWLEDGEMENTS

I would like to express my sincere gratitude to my supervisors Prof. Stasys Tautkus and Prof. Aivaras Kareiva for their guidance, numerous discussions and support during my studies.

I wish to thank all my colleagues from Faculty of Chemistry of Vilnius University, especially I would like to thank personnel of Department of Analytical and Environmental Chemistry and members of Sol-Gel Chemistry Group for their help and support.

Special thanks to my colleagues Dr. Tomas Šalkus and Dr. Algimantas Kežionis from Faculty of Physics of Vilnius University for performing impedance spectroscopy measurements.

I would also like to thank Dr. Vitalija Jasulaitienė from Center for Physical Sciences and Technology for performing XPS measurements and help in interpretation of obtained results.

Finally, I thank my family members for their love and support.

REFERENCES

- [1] Z. Gao, L.V. Mogni, E.C. Miller, J.G. Railsback, S.A. Barnett, *Energ. Environ. Sci.*, 9 (2016) 1602-1644.
- [2] K. Funke, *Sci. Technol. Adv. Mater.*, 14 (2013) 043502.
- [3] International Energy Outlook 2013, Web. 25 Aug 2016, <http://www.eia.gov/todayinenergy/detail.cfm?id=12251#>.
- [4] T. Liu, X. Zhang, L. Yuan, J. Yu, *Solid State Ionics*, 283 (2015) 91-102.
- [5] J. Lim, G. Manfredi, S. Gavrilov, K. Rosseel, A. Aerts, J. Van den Bosch, *Sens. Actuator B-Chem.*, 204 (2014) 388-392.
- [6] B. Bernard, L. Bianchi, A. Malié, A. Joulia, B. Rémy, *J. Eur. Ceram. Soc.*, 36 (2016) 1081-1089.
- [7] S.P. Passos, B. Linke, H. Larjava, D. French, *Clin. Oral Impl. Res.*, 27 (2016) 47-54.
- [8] M. Capdevila-Cortada, G. Vilé, D. Teschner, J. Pérez-Ramírez, N. López, *Appl. Catal. B*, 197 (2016) 299-312.
- [9] P. Janoš, J. Ederer, V. Pilařová, J. Henych, J. Tolasz, D. Milde, T. Opletal, *Wear*, 362–363 (2016) 114-120.
- [10] S. Zhang, J. Li, X. Guo, L. Liu, H. Wei, Y. Zhang, *Appl. Surf. Sci.*, 382 (2016) 316-322.
- [11] M. Balestrieri, S. Colis, M. Gallart, G. Schmerber, P. Bazylewski, G.S. Chang, M. Ziegler, P. Gilliot, A. Slaoui, A. Dinia, *Phys. Chem. Chem. Phys.*, 18 (2016) 2527-2534.
- [12] A. Evans, A. Bieberle-Hütter, J.L.M. Rupp, L.J. Gauckler, *J. Power Sources*, 194 (2009) 119-129.
- [13] S. Hull, *Rep. Prog. Phys.*, 67 (2004) 1233-1314.
- [14] H.-H. Möbius, History, in: S.C. Singhal, K. Kendal (Eds.) *High temperature and solid oxide fuel cells*, Elsevier 2003, pp. 23-51.
- [15] M. O'Keefe, Phase transitions and translational freedom in solid electrolytes, in: G. Mahan, W. Roth (Eds.) *Superionic conductors*, Springer 1976, pp. 101-114.
- [16] C. Tubandt, *Z. Anorg. Allg. Chem.*, 115 (1921) 105-126.

- [17] R.J.D. Tilley, Defects in solids, in: R.A. Scott (Ed.) Encyclopedia of inorganic and bioinorganic chemistry, Wiley 2011.
- [18] W.B. Fowler, R. Phillips, A.E. Carlsson, Point and extended defects in crystals, in: G.L. Trigg (Ed.) Encyclopedia of applied physics, Wiley 2003.
- [19] S.J. Skinner, J.A. Kilner, Mater. Today, 6 (2003) 30-37.
- [20] W. Münch, K.D. Kreuer, G. Seifert, J. Maier, Solid State Ionics, 136–137 (2000) 183-189.
- [21] S.P.S. Badwal, Solid State Ionics, 52 (1992) 23-32.
- [22] University of Cambridge, Teaching and learning packages, Web. 25 Aug 2016, http://www.doitpoms.ac.uk/tlplib/fuel-cells/sofc_electrolyte.php.
- [23] Y. Arachi, H. Sakai, O. Yamamoto, Y. Takeda, N. Imanishai, Solid State Ionics, 121 (1999) 133-139.
- [24] T. Ishihara, N.M. Sammes, O. Yamamoto, Electrolytes, High temperature solid oxide fuel cells, Elsevier 2003, pp. 83-117.
- [25] M. Mogensen, D. Lybye, N. Bonanos, P.V. Hendriksen, F.W. Poulsen, Solid State Ionics, 174 (2004) 279-286.
- [26] S.C. Singhal, Solid oxide fuel cells: Past, present and future, in: T.S.J. Irvine, P. Connor (Eds.) Solid oxide fuels cells: Facts and figures: Past present and future perspectives for SOFC technologies, Springer 2013, pp. 1-23.
- [27] M. Lo Faro, A.S. Aricò, Ceramic membranes for intermediate temperature solid oxide fuel cells (SOFCs): state of the art and perspectives, in: A. Basile (Ed.) Membranes for clean and renewable power applications, Woodhead Publishing 2014, pp. 237-265.
- [28] B. Scherrer, M.V.F. Schlupp, D. Stender, J. Martynczuk, J.G. Grolig, H. Ma, P. Kocher, T. Lippert, M. Prestat, L.J. Gauckler, Adv. Funct. Mater., 23 (2013) 1957-1964.
- [29] C. Sun, H. Li, L. Chen, Energ. Environ. Sci., 5 (2012) 8475-8505.
- [30] M. Mogensen, N.M. Sammes, G.A. Tompsett, Solid State Ionics, 129 (2000) 63-94.
- [31] N.Q. Minh, T. Takahashi, Electrolyte, Science and technology of ceramic fuel cells, Elsevier 1995, pp. 69-116.

- [32] B.C.H. Steele, *Solid State Ionics*, 129 (2000) 95-110.
- [33] A. Azzolini, J. Downs, V.M. Sglavo, *J. Eur. Ceram. Soc.*, 35 (2015) 2119-2127.
- [34] W. Zając, L. Suescun, K. Świerczek, J. Molenda, *J. Power Sources*, 194 (2009) 2-9.
- [35] J.-h. Myung, T.H. Shin, X. Huang, C. Savaniu, J. Irvine, *Int. J. Appl. Ceram. Tec.*, 13 (2016) 269-273.
- [36] S.R. Bishop, H.L. Tuller, Y. Kuru, B. Yildiz, *J. Eur. Ceram. Soc.*, 31 (2011) 2351-2356.
- [37] K. Huang, J.B. Goodenough, *Materials for solid oxide fuel cells (SOFCs), Solid oxide fuel cell technology*, Woodhead Publishing 2009, pp. 220-268.
- [38] K. Huang, J.B. Goodenough, *Oxide-ion electrolytes in solid oxide fuel cells (SOFCs), Solid oxide fuel cell technology*, Woodhead Publishing 2009, pp. 67-84.
- [39] M. Shirpour, G. Gregori, R. Merkle, J. Maier, *Phys. Chem. Chem. Phys.*, 13 (2011) 937-940.
- [40] L. Guo, H.B. Guo, S.K. Gong, H.B. Xu, *Ceram. Int.*, 39 (2013) 9009-9015.
- [41] J.S. Zhang, Y.F. Wu, L.H. Luo, G.Y. Shen, H. Su, *Electrical conductivity and characterization of CeO₂ doped 8YSZ electrolyte with 2%wt CuO doping*, in: W. Pan, J.H. Gong (Eds.) *High-performance ceramics VII*, Trans Tech Publications 2012, pp. 1564-1568.
- [42] E. Rebollo, C. Mortalo, S. Escolastico, S. Boldrini, S. Barison, J.M. Serra, M. Fabrizio, *Energ. Environ. Sci.*, 8 (2015) 3675-3686.
- [43] A.P. Jamale, C.H. Bhosale, L.D. Jadhav, *J. Alloys Compd.*, 623 (2015) 136-139.
- [44] A.R. West, *Solid state chemistry and its applications*, Wiley 1989.
- [45] Z. Shao, W. Zhou, Z. Zhu, *Prog. Mater. Sci.*, 57 (2012) 804-874.
- [46] C. Viazzi, A. Deboni, J. Zoppas Ferreira, J.-P. Bonino, F. Ansart, *Solid State Sci.*, 8 (2006) 1023-1028.
- [47] Z. Wang, G.M. Kale, M. Ghadiri, *J. Am. Ceram. Soc.*, 95 (2012) 2863-2868.

- [48] F.-t. Li, J. Ran, M. Jaroniec, S.Z. Qiao, *Nanoscale*, 7 (2015) 17590-17610.
- [49] H. Mohebbi, T. Ebadzadeh, F.A. Hesari, *J. Power Sources*, 178 (2008) 64-68.
- [50] A. Akbari-Fakhrabadi, V. Meruane, M. Jamshidijam, M.A. Gracia-Pinilla, R.V. Mangalaraja, *Mater. Sci. Eng., A*, 649 (2016) 168-173.
- [51] A.K. Pandey, K. Biswas, *Ceram. Int.*, 42 (2016) 2306-2316.
- [52] L. Guo, M. Li, F. Ye, *Ceram. Int.*, 42 (2016) 7360-7365.
- [53] Y. Hui, S. Zhao, J. Xu, B. Zou, Y. Wang, X. Cai, L. Zhu, X. Cao, *Ceram. Int.*, 42 (2016) 341-350.
- [54] D. Zhang, S.G. Huang, Y.M. Guo, C.C. Wang, *Mater. Lett.*, 166 (2016) 192-195.
- [55] S.-Y. Park, J.H. Ahn, C.-W. Jeong, C.W. Na, R.-H. Song, J.-H. Lee, *Int. J. Hydrogen Energy*, 39 (2014) 12894-12903.
- [56] M. Yoshimura, K. Byrappa, *J. Mater. Sci.*, 43 (2007) 2085-2103.
- [57] K. Sato, K. Horiguchi, T. Nishikawa, S. Yagishita, K. Kuruma, T. Murakami, H. Abe, *Inorg. Chem.*, 54 (2015) 7976-7984.
- [58] K. Sato, M. Arai, J.-C. Valmalette, H. Abe, *Langmuir*, 30 (2014) 12049-12056.
- [59] A. Thorel, Tape casting ceramics for high temperature fuel cell applications, in: W. Wunderlich (Ed.) *Ceramic Materials*, Sciyo 2010.
- [60] D. McKinney, W. Sigmund, *Colloidal processing fundamentals*, in: S. Somiya (Ed.) *Handbook of advanced ceramics* (2nd ed.), Elsevier 2013, pp. 911-926.
- [61] C.B. Carter, M.G. Norton, *Coatings and thick films*, *Ceramic materials: science and engineering*, Springer 2007, pp. 481-493.
- [62] X. Cheng, C. Wang, B. Wang, R. Sun, Y. Guan, Y. Sun, X. Liang, P. Sun, G. Lu, *Sens. Actuator B-Chem.*, 221 (2015) 1321-1329.
- [63] B. Charlas, C. Grings Schmidt, H. Lund Frandsen, K. Bøhm Andersen, D. Boccaccini, K. Kammer Hansen, A. Roosen, A. Kaiser, *Ceram. Int.*, 42 (2016) 4546-4555.

- [64] J. Xiong, C. Jiao, M. Han, W. Yi, J. Ma, C. Yan, *RSC Adv.*, 5 (2015) 87477-87483.
- [65] C. Seok, J. Moon, M. Park, J. Hong, H. Kim, J.-W. Son, J.-H. Lee, B.-K. Kim, H.-W. Lee, K.J. Yoon, *J. Eur. Ceram. Soc.*, 36 (2016) 1417-1425.
- [66] C. Nicollet, A. Flura, V. Vibhu, A. Rougier, J.M. Bassat, J.C. Grenier, *J. Power Sources*, 294 (2015) 473-482.
- [67] A. Wang, J. Pu, D. Yan, N.-Q. Duan, Y. Tan, L. Jia, B. Chi, J. Li, *J. Power Sources*, 303 (2016) 137-141.
- [68] S. Sønderby, B.H. Christensen, K.P. Almqvist, L.P. Nielsen, P. Eklund, *Surf. Coat. Technol.*, 281 (2015) 150-156.
- [69] W.H. Tanveer, S. Ji, W. Yu, G.Y. Cho, Y.H. Lee, S.W. Cha, *J. Nanosci. Nanotechnol.*, 15 (2015) 8926-8930.
- [70] J. Jiang, W. Shen, J.L. Hertz, *Thin Solid Films*, 522 (2012) 66-70.
- [71] D.P. Norton, *Pulsed laser deposition of complex materials: Progress toward applications*, Pulsed laser deposition of thin films, Wiley 2006, pp. 1-31.
- [72] E.M. Hopper, E. Perret, B.J. Ingram, H. You, K.-C. Chang, P.M. Baldo, P.H. Fuoss, J.A. Eastman, *J. Phys. Chem. C*, 119 (2015) 19915-19921.
- [73] K. Develos-Bagarinao, H. Kishimoto, K. Yamaji, T. Horita, H. Yokokawa, *Nanotechnology*, 26 (2015) 9.
- [74] K.-R. Lee, K. Ahn, Y.-C. Chung, J.-H. Lee, H.-I. Yoo, *Solid State Ionics*, 229 (2012) 45-53.
- [75] L.A. Chow, Equipment and manufacturability issues in CVD processes, in: K. Seshan (Ed.) *Handbook of thin film deposition* (3rd ed.), Elsevier 2012, pp. 127-178.
- [76] M.V.F. Schlupp, A. Kurlov, J. Hwang, Z. Yang, M. Dobeli, J. Martynczuk, M. Prestat, J.W. Son, L.J. Gauckler, *Fuel Cells*, 13 (2013) 658-665.
- [77] D. Beckel, A. Bieberle-Hütter, A. Harvey, A. Infortuna, U.P. Muecke, M. Prestat, J.L.M. Rupp, L.J. Gauckler, *J. Power Sources*, 173 (2007) 325-345.
- [78] J. Im, I. Park, D. Shin, *Ceram. Int.*, 38 (2012) 2051-2058.
- [79] J. Lee, I. Park, H. Lee, D. Shin, *J. Power Sources*, 212 (2012) 35-42.

- [80] B. Scherrer, J. Martynczuk, H. Galinski, J.G. Grolig, S. Binder, A. Bieberle-Hutter, J.L.M. Rupp, M. Prestat, L.J. Gauckler, *Adv. Funct. Mater.*, 22 (2012) 3509-3518.
- [81] G. Constantin, C. Rossignol, J.P. Barnes, E. Djurado, *Solid State Ionics*, 235 (2013) 36-41.
- [82] C.L. Eggen, P.M. McAfee, Y. Jin, Y.S. Lin, *Thin Solid Films*, 591, Part A (2015) 111-118.
- [83] J. Hierso, P. Boy, K. Valle, J. Vulliet, F. Blein, C. Laberty-Robert, C. Sanchez, *J. Solid State Chem.*, 197 (2013) 113-119.
- [84] A. Dey, A. Singh, D. Das, P.K. Iyer, *Organic semiconductors: A new future of nanodevices and applications*, in: S. Babu Krishna Moorthy (Ed.) *Thin film structures in energy applications*, Springer 2015, pp. 97-128.
- [85] D.P. Birnie, *Spin coating: Art and science*, in: T. Schneller, R. Waser, M. Kosec, D. Payne (Eds.) *Chemical solution deposition of functional oxide thin films*, Springer 2013, pp. 263-274.
- [86] T. Van Gestel, D. Sebold, H.P. Buchkremer, *J. Eur. Ceram. Soc.*, 35 (2015) 1505-1515.
- [87] Y.V. França, F. Leitão, H.M. Shihomatsu, W.S. Scapin, N.M.P. de Moraes, V.L. Salvador, A.M.G. Figueiredo, E.N.S. Muccillo, R. Muccillo, *Chromatographia*, 49 (1999) 91-94.
- [88] S.-J. Hao, C. Wang, T.-L. Liu, J.-L. Wang, Z.-Q. Mao, *Ceram. Int.*, 42 (2016) 9323-9326.
- [89] E.W. Leib, R.M. Pasquarelli, J.J. do Rosario, P.N. Dyachenko, S. Doring, A. Puchert, A.Y. Petrov, M. Eich, G.A. Schneider, R. Janssen, H. Weller, T. Vossmeier, *J. Mater. Chem. C*, 4 (2016) 62-74.
- [90] C.N. Chervin, B.J. Clapsaddle, H.W. Chiu, A.E. Gash, J.H. Satcher, S.M. Kauzlarich, *Chem. Mater.*, 18 (2006) 4865-4874.
- [91] M. Guo, J. Lu, Y. Wu, Y. Wang, M. Luo, *Langmuir*, 27 (2011) 3872-3877.
- [92] A. Akbari-Fakhrabadi, R.E. Avila, H.E. Carrasco, S. Ananthakumar, R.V. Mangalaraja, *J. Alloys Compd.*, 541 (2012) 1-5.
- [93] C.-K. Cho, B.-H. Choi, K.-T. Lee, *J. Alloys Compd.*, 541 (2012) 433-439.

- [94] M.-Y. Lee, M.-K. Song, J.-S. Kim, J.-H. Seo, M.-H. Kim, *J. Am. Ceram. Soc.*, 97 (2014) 1379-1382.
- [95] C. Dubourdieu, S.B. Kang, Y.Q. Li, G. Kulesha, B. Gallois, *Thin Solid Films*, 339 (1999) 165-173.
- [96] S. Heiroth, T. Lippert, A. Wokaun, M. Döbeli, *Appl. Phys. A*, 93 (2008) 639-643.
- [97] Y.S. Hong, S.H. Kim, W.J. Kim, H.H. Yoon, *Curr. Appl. Phys.*, 11 (2011) S163-S168.
- [98] F.M.L. Figueiredo, F.M.B. Marques, *Wiley Interdiscip. Rev. Energy Environ.*, 2 (2013) 52-72.
- [99] S.C. Singhal, K. Kendall, Introduction to SOFCs, in: S.C. Singhal, K. Kendal (Eds.) *High temperature solid oxide fuel cells*, Elsevier 2003, pp. 1-22.
- [100] A. McEvoy, Anodes, in: S.C. Singhal (Ed.) *High temperature solid oxide fuel cells*, Elsevier 2003, pp. 149-171.
- [101] J. Ju, J. Lin, Y. Wang, Y. Zhang, C. Xia, *J. Power Sources*, 302 (2016) 298-307.
- [102] G.D. Han, K.C. Neoh, K. Bae, H.J. Choi, S.W. Park, J.-W. Son, J.H. Shim, *J. Power Sources*, 306 (2016) 503-509.
- [103] M.Z. Khan, M.T. Mehran, R.-H. Song, J.-W. Lee, S.-B. Lee, T.-H. Lim, S.-J. Park, *Ceram. Int.*, 42 (2016) 6978-6984.
- [104] C. Zuo, M. Liu, M. Liu, *Solid oxide fuel cells*, in: M. Aparicio, A. Jitianu, C.L. Klein (Eds.) *Sol-gel processing for conventional and alternative energy*, Springer 2012, pp. 7-36.
- [105] R. Moos, *Int. J. Appl. Ceram. Tec.*, 2 (2005) 401-413.
- [106] R. Ramamoorthy, P.K. Dutta, S.A. Akbar, *J. Mater. Sci.*, 38 (2003) 4271-4282.
- [107] J.R. Stetter, J. Li, *Chem. Rev.*, 108 (2008) 352-366.
- [108] R. Moos, N. Izu, F. Rettig, S. Reiss, W. Shin, I. Matsubara, *Sensors*, 11 (2011) 3439-3465.
- [109] P.K. Sekhar, R. Mukundan, E. Brosha, F. Garzon, *Sens. Actuator B-Chem.*, 183 (2013) 20-24.

- [110] I. Romanytsia, J.-P. Viricelle, P. Vernoux, C. Pijolat, *Sens. Actuator B-Chem.*, 207, Part A (2015) 391-397.
- [111] J.W. Fergus, *Sens. Actuator B-Chem.*, 134 (2008) 1034-1041.
- [112] Y. Fujio, T. Sato, N. Miura, *Solid State Ionics*, 262 (2014) 266-269.
- [113] I.I. Soykal, P.H. Matter, L.B. Thrun, R.Q. Long, S.L. Swartz, U.S. Ozkan, *IEEE Sens. J.*, 16 (2016) 1532-1540.
- [114] P. Nagaraju, Y. Vijayakumar, D.M. Phase, R.J. Choudary, M.V.R. Reddy, *J. Mater. Sci.-Mater. Electron.*, 27 (2016) 651-658.
- [115] C.Y. Chen, K.H. Chang, H.Y. Chiang, S.J. Shih, *Sens. Actuator B-Chem.*, 204 (2014) 31-41.
- [116] A. Díaz-Parralejo, A.L. Ortiz, F. Rodríguez-Rojas, F. Guiberteau, *Thin Solid Films*, 518 (2010) 2779-2782.
- [117] R. Ahmadi-Pidani, R. Shoja-Razavi, R. Mozafarinia, H. Jamali, *Mater. Des.*, 57 (2014) 336-341.
- [118] S. Affatato, A. Ruggiero, M. Merola, *Composites Part B*, 83 (2015) 276-283.
- [119] S. Sikarwar, B.C. Yadav, S. Singh, G.I. Dzhardimalieva, S.I. Pomogailo, N.D. Golubeva, A.D. Pomogailo, *Sens. Actuator B-Chem.*, 232 (2016) 283-291.
- [120] M.N. Tsampas, F.M. Sapountzi, P. Vernoux, *Catal. Sci. Technol.*, 5 (2015) 4884-4900.
- [121] L. Almar, A. Tarancon, T. Andreu, M. Torrell, Y. Hu, G. Dezanneau, A. Morata, *Sens. Actuator B-Chem.*, 216 (2015) 41-48.
- [122] H.-L. Lin, C.-Y. Wu, R.-K. Chiang, *J. Colloid Interface Sci.*, 341 (2010) 12-17.
- [123] S.R. Jain, K.C. Adiga, V.R. Pai Verneker, *Combust. Flame*, 40 (1981) 71-79.
- [124] A. Kezionis, S. Kazlauskas, D. Petrulionis, A.F. Orliukas, *IEEE Trans. Microw. Theory Tech.*, 62 (2014) 2456-2461.
- [125] A. Kezionis, P. Butvilas, T. Salkus, S. Kazlauskas, D. Petrulionis, T. Zukauskas, E. Kazakevicius, A.F. Orliukas, *Rev. Sci. Instrum.*, 84 (2013) 8.

- [126] E. Drożdż-Cieśla, A. Małecki, B. Jajko, *J. Therm. Anal. Calorim.*, 92 (2008) 939-944.
- [127] A.S. Deshpande, Y.B. Kholam, A.J. Patil, S.B. Deshpande, H.S. Potdar, S.K. Date, *Mater. Lett.*, 51 (2001) 161-171.
- [128] A. Glasner, E. Levy, M. Steinberg, *J. Inorg. Nucl. Chem.*, 25 (1963) 1119-1127.
- [129] O. Vasykiv, Y. Sakka, *J. Am. Ceram. Soc.*, 83 (2000) 2196-2202.
- [130] W.W. Wendlandt, T.D. George, G.R. Horton, *J. Inorg. Nucl. Chem.*, 17 (1961) 273-280.
- [131] K. Tõnsuaadu, A. Zalga, A. Beganskiene, A. Kareiva, *J. Therm. Anal. Calorim.*, 110 (2012) 77-83.
- [132] D. Wyrzykowski, E. Hebanowska, G. Nowak-Wiczak, M. Makowski, L. Chmurzyński, *J. Therm. Anal. Calorim.*, 104 (2011) 731-735.
- [133] S. Banerjee, A. Kumar, P. Sujatha Devi, *J. Therm. Anal. Calorim.*, 104 (2011) 859-867.
- [134] H.B. Wang, C.R. Xia, G.Y. Meng, D.K. Peng, *Mater. Lett.*, 44 (2000) 23-28.
- [135] N. Petrova, D. Todorovsky, *Mater. Res. Bull.*, 41 (2006) 576-589.
- [136] S. Komine, F. Munakata, *J. Mater. Sci.*, 40 (2005) 3887-3890.
- [137] S. Kazlauskas, A. Kežionis, T. Šalkus, A.F. Orliukas, *Solid State Ionics*, 262 (2014) 593-596.
- [138] B. Yu, W. Zhang, J. Xu, J. Chen, X. Luo, K. Stephan, *Int. J. Hydrogen Energy*, 37 (2012) 12074-12080.
- [139] M.F. Morks, C.C. Berndt, Y. Durandet, M. Brandt, J. Wang, *Appl. Surf. Sci.*, 256 (2010) 6213-6218.
- [140] S. Kotrlý, L. Sucha, *Handbook of chemical equilibria in analytical chemistry*, Ellis Horwood 1985.
- [141] T. Mahata, G. Das, R.K. Mishra, B.P. Sharma, *J. Alloys Compd.*, 391 (2005) 129-135.
- [142] O. Opuchovic, A. Beganskiene, A. Kareiva, *J. Alloys Compd.*, 647 (2015) 189-197.

- [143] B. Ksapabutr, E. Gulari, S. Wongkasemjit, *Mater. Chem. Phys.*, 99 (2006) 318-324.
- [144] T. Aarii, T. Taguchi, A. Kishi, M. Ogawa, Y. Sawada, *J. Eur. Ceram. Soc.*, 22 (2002) 2283-2289.
- [145] B. Ambrozini, P.R. Dametto, A.B. Siqueira, C.T. Carvalho, M. Ionashiro, *J. Therm. Anal. Calorim.*, 97 (2009) 761-764.
- [146] E. Garskaite, K.-A. Gross, S.-W. Yang, T.C.-K. Yang, J.-C. Yang, A. Kareiva, *CrystEngComm*, 16 (2014) 3950-3959.
- [147] A. Leleckaite, A. Kareiva, H. Bettentrup, T. Justel, H.J. Meyer, *Zeitschrift Fur Anorganische Und Allgemeine Chemie*, 631 (2005) 2987-2993.
- [148] K. Nakamoto, *Theory of normal vibrations, Infrared and Raman spectra of inorganic and coordination compounds*, Wiley 2008, pp. 1-147.
- [149] V. Grover, R. Shukla, R. Kumari, B.P. Mandal, P.K. Kulriya, S.K. Srivastava, S. Ghosh, A.K. Tyagi, D.K. Avasthi, *Phys. Chem. Chem. Phys.*, 16 (2014) 27065-27073.
- [150] D.R. Mullins, S.H. Overbury, D.R. Huntley, *Surf. Sci.*, 409 (1998) 307-319.
- [151] X. Yu, G. Li, *J. Alloys Compd.*, 364 (2004) 193-198.
- [152] J.Z. Shyu, K. Otto, W.L.H. Watkins, G.W. Graham, R.K. Belitz, H.S. Gandhi, *J. Catal.*, 114 (1988) 23-33.
- [153] T. Guo, L. Zhang, X. Song, X. Dong, M.M. Shirolkar, M. Wang, M. Li, H. Wang, *J. Power Sources*, 262 (2014) 239-244.
- [154] M.Z. Khan, R.-H. Song, S.-B. Lee, J.-W. Lee, T.-H. Lim, S.-J. Park, *Int. J. Hydrogen Energy*, 39 (2014) 20799-20805.
- [155] K.M. Paciejewska, Y. Yu, Uuml, S. Hn, A. Weber, M. Kleber, *J. Ceram. Soc. Jpn.*, 123 (2015) 171-177.
- [156] J.R. McBride, K.C. Hass, B.D. Poindexter, W.H. Weber, *J. Appl. Phys.*, 76 (1994) 2435-2441.
- [157] O.S. Khalipova, V. Lair, A. Ringuede, *Electrochim. Acta*, 116 (2014) 183-187.

- [158] J.E. Spanier, R.D. Robinson, F. Zhang, S.-W. Chan, I.P. Herman, *Phys. Rev. B*, 64 (2001) 245407.
- [159] S.B. Anantharaman, R. Bauri, *Ceram. Int.*, 39 (2013) 9421-9428.
- [160] S. Saitzek, J.F. Blach, S. Villain, J.R. Gavarrri, *Phys. Status Solidi A*, 205 (2008) 1534-1539.
- [161] T. Taniguchi, T. Watanabe, N. Sugiyama, A.K. Subramani, H. Wagata, N. Matsushita, M. Yoshimura, *J. Phys. Chem. C*, 113 (2009) 19789-19793.
- [162] I. Kosacki, V. Petrovsky, H.U. Anderson, P. Colomban, *J. Am. Ceram. Soc.*, 85 (2002) 2646-2650.
- [163] S.A. Acharya, V.M. Gaikwad, S.W. D'Souza, S.R. Barman, *Solid State Ionics*, 260 (2014) 21-29.
- [164] A. Banerji, V. Grover, V. Sathe, S.K. Deb, A.K. Tyagi, *Solid State Commun.*, 149 (2009) 1689-1692.
- [165] C. Artini, M. Pani, M.M. Carnasciali, M.T. Buscaglia, J.R. Plaisier, G.A. Costa, *Inorg. Chem.*, 54 (2015) 4126-4137.
- [166] C.T. Nottbohm, C. Hess, *Catal. Commun.*, 22 (2012) 39-42.
- [167] L. Qiu, F. Liu, L. Zhao, Y. Ma, *Appl. Surf. Sci.*, 252 (2006) 4931-4935.
- [168] D. Mesguich, C. Aymonier, J.-M. Bassat, F. Mauvy, E. You, J.J. Watkins, *Chem. Mater.*, 23 (2011) 5323-5330.
- [169] R. López, R. Gómez, *J. Sol-Gel Sci. Technol.*, 61 (2012) 1-7.
- [170] T. Suzuki, I. Kosacki, V. Petrovsky, H.U. Anderson, *J. Appl. Phys.*, 91 (2002) 2308-2314.
- [171] C. Ho, J.C. Yu, T. Kwong, A.C. Mak, S. Lai, *Chem. Mater.*, 17 (2005) 4514-4522.
- [172] F. Pinar Gokdemir, A. Evrim Saatci, O. Ozdemir, B. Keskin, K. Kutlu, *Mater. Sci. Semicond. Process.*, 38 (2015) 300-305.
- [173] T.-S. Oh, Y.S. Tokpanov, Y. Hao, W. Jung, S.M. Haile, *J. Appl. Phys.*, 112 (2012) 103535.
- [174] A. Eltayeb, R.K. Vijayaraghavan, A.P. McCoy, J. Cullen, S. Daniels, E. McGlynn, *Thin Solid Films*, 603 (2016) 363-370.
- [175] E. Ruiz-Trejo, *J. Phys. Chem. Solids*, 74 (2013) 605-610.